#### UNIVERSITY OF CALIFORNIA Santa Barbara

## Millimeter Wave MIMO: Design and Evaluation of Practical System Architectures

A Dissertation submitted in partial satisfaction of the requirements for the degree of

Doctor of Philosophy

in

Electrical and Computer Engineering

by

Eric G. Torkildson

#### Committee in Charge:

Professor Upamanyu Madhow, Chair

Professor Shivkumar Chandrasekaran

Professor Jerry Gibson

Professor Mark Rodwell

December 2010

#### Abstract

#### Millimeter Wave MIMO: Design and Evaluation of Practical System Architectures

#### Eric G. Torkildson

Unlicensed spectrum at 60 GHz and the E-band frequencies spans multiple GHz, enabling wireless links to reach multi-Gb/s speeds. In this work, we propose increasing speeds further by leveraging spatial multiplexing gains at millimeter (mm) wave. To this end, we design and evaluate practical MIMO architectures that address the unique challenges and opportunities associated with mm wave communication. We begin by recognizing that the mm wave channel is predominantly line-of-sight (LOS), and develop arrays that provide robust spatial multiplexing gains in this environment. Noting that the cost and power consumption of ADCs become limiting factors as bandwidths scale to multiple GHz, we then propose a hierarchical approach to MIMO signal processing. Spatial processing, including beamforming and spatial multiplexing, is performed on a slow time scale and followed by separate temporal processing of each of the multiplexed data streams. This design is implemented in a four-channel hardware prototype.

We then investigate mm wave spatial multiplexing for short range indoor applications, first by quantifying fundamental limits in LOS environments, and then by investigating performance in the presence of multipath and LOS blockage. For

linear arrays with constrained form factor, an asymptotic analysis (as the number

of antenna elements gets large) based on properties of prolate spheroidal wave

functions shows that a sparse array producing a spatially uncorrelated channel

matrix effectively provides the maximum number of spatial degrees of freedom in

a LOS environment, but that substantial beamforming gains can be obtained by

using a denser array. This motivates a system architecture that utilizes arrays

of subarrays to provide both directivity and spatial multiplexing gains. The per-

formance of this system is evaluated in a simulated indoor environment using a

ray-tracing model that incorporates multipath effects and potential LOS block-

age. Our numerical results provide insight into the spatial variations of attainable

capacity within a room, and the combinations of beamsteering and spatial multi-

plexing used in different scenarios.

Professor Upamanyu Madhow

Dissertation Committee Chair

iii

## Contents

A	bstra	ct	ii
Li	st of	Figures	vi
Li	st of	Tables	viii
1	$\mathbf{Intr}$	roduction	1
	1.1	LOS Spatial Multiplexing at mm Wave Frequencies	5
	1.2	Hierarchical MIMO Signal Processing: Architecture and Prototype	6
	1.3	Feasibility and Performance Study of Indoor mm Wave MIMO Links	8
	1.4	Related Work	9
<b>2</b>	LOS	S Spatial Multiplexing Over Millimeter-Wave Links	11
	2.1	LOS Spatial Multiplexing	12
		2.1.1 LOS MIMO Channel Model	13
		2.1.2 The Rayleigh Spacing Criterion	15
		2.1.3 Application to mm-Wave Links	17
	2.2	Spatial Correlation at Non-Optimal Link	
	Rang	${ m ges}$	21
		2.2.1 Noise Enhancement at Non-Optimal Link Ranges	24
	2.3	Optimized Nonuniform Arrays	27
		2.3.1 4-element Nonuniform Array Analysis	27
		2.3.2 Optimization Procedure and Results	31
	2.4	Rank Adaptation	34
	2.5	Discussion	39

	type			
	3.1 Two-level mm-Wave MIMO Architecture			
	3.1.1 Pilot-Symbol-Aided Channel Estimation	•	•	
	Background			
	3.1.2 System Architecture			
	3.1.3 Channel Model			
	3.2 Spatial Interference Suppression			
	3.2.1 DFT-Based Channel Estimation:			
	3.2.2 Least Squares Channel Estimation:			
	3.2.3 Closed-Loop Equalization:			
	3.2.4 Simulation Results			
	3.3 Hardware Prototype			
	3.3.1 Transmitter and Receiver Electronics			
	3.3.2 Experimental Results			
	3.4 Discussion			
	4.1 Fundamental Limits of LOS MIMO			
	4.1.1 LOS MIMO Channel Model			
	4.1.1 LOS MIMO Channel Model			
	4.1.1 LOS MIMO Channel Model			
	4.1.1 LOS MIMO Channel Model			
	4.1.1 LOS MIMO Channel Model			
	4.1.1 LOS MIMO Channel Model			
	4.1.1 LOS MIMO Channel Model			
	4.1.1 LOS MIMO Channel Model 4.1.2 Spatial Degrees of Freedom 4.2 LOS mm-Wave MIMO Architecture 4.2.1 Waterfilling Benchmark 4.2.2 Transmit Beamsteering/Receive MMSE 4.3 Indoor Propagation Model 4.4 Results 4.4.1 Performance of Waterfilling Benchmark 4.4.2 Performance of Transmit Beamsteering/Receive MMSE 4.4.3 Performance of Transmit Beamsteering/Receive MMSE			
	4.1.1 LOS MIMO Channel Model 4.1.2 Spatial Degrees of Freedom 4.2 LOS mm-Wave MIMO Architecture 4.2.1 Waterfilling Benchmark 4.2.2 Transmit Beamsteering/Receive MMSE 4.3 Indoor Propagation Model 4.4 Results 4.4.1 Performance of Waterfilling Benchmark 4.4.2 Performance of Transmit Beamsteering/Receive MMSE 4.4.3 Transmitter Alignment			
	4.1.1 LOS MIMO Channel Model 4.1.2 Spatial Degrees of Freedom 4.2 LOS mm-Wave MIMO Architecture 4.2.1 Waterfilling Benchmark 4.2.2 Transmit Beamsteering/Receive MMSE 4.3 Indoor Propagation Model 4.4 Results 4.4.1 Performance of Waterfilling Benchmark 4.4.2 Performance of Transmit Beamsteering/Receive MMSE 4.4.3 Performance of Transmit Beamsteering/Receive MMSE			
5	4.1.1 LOS MIMO Channel Model 4.1.2 Spatial Degrees of Freedom 4.2 LOS mm-Wave MIMO Architecture 4.2.1 Waterfilling Benchmark 4.2.2 Transmit Beamsteering/Receive MMSE 4.3 Indoor Propagation Model 4.4 Results 4.4.1 Performance of Waterfilling Benchmark 4.4.2 Performance of Transmit Beamsteering/Receive MMSE 4.4.3 Transmitter Alignment			

## List of Figures

2.1	Aligned uniform linear arrays	14
2.2	Subarray configurations	19
2.3	Spatial correlation in <b>H</b>	22
2.4	Array response at various link ranges	23
2.5	Noise enhancement as a function of range	25
2.6	Correlation $\rho(1,4)$	28
2.7	Optimization metric $\gamma$ for symmetric 4-element array	30
2.8	Maximum noise enhancement as a function of range for an opti-	
mize	d 4-element array	32
2.9	Maximum noise enhancement as a function of range for an opti-	
mize	d 5-element array	33
2.10	Maximum noise enhancement as a function of range for an opti-	
	d 6-element array	34
2.11	$\mathcal{I}$ as a function of $N_s$ , the number of independent transmitted signals.	37
2.12	Rank adaptation strategy compared to channel capacity	38
		0.0
3.1	Two-level system architecture	46
3.1 3.2		
	Two-level system architecture	46
3.2	Two-level system architecture	46 51
3.2 3.3	Two-level system architecture	46 51 58
3.2 3.3 3.4	Two-level system architecture	46 51 58 59
3.2 3.3 3.4 3.5	Two-level system architecture	46 51 58 59 64
3.2 3.3 3.4 3.5 3.6	Two-level system architecture	46 51 58 59 64 65
3.2 3.3 3.4 3.5 3.6 3.7	Two-level system architecture	46 51 58 59 64 65 66
3.2 3.3 3.4 3.5 3.6 3.7 3.8	Two-level system architecture	46 51 58 59 64 65 66 68
3.2 3.3 3.4 3.5 3.6 3.7 3.8 3.9	Two-level system architecture.  Open-loop spatial equalizer structure.  Closed-loop frequency domain spatial equalizer structure.  Discrete Fourier transform of received signal.  SIR using DFT-based spatial equalizer.  SIR using LSE-based spatial equalizer.  SIR using closed-loop spatial equalizer.  Transmitter prototype block diagram.  Receiver prototype block diagram.	466 511 586 59 644 656 686 686

4.1	Squared singular values of discrete ULA channel matrix	81
4.2	Eigenvalues of continuous array channel	85
4.3	Array of subarrays architecture	87
4.4	Indoor environment model	93
4.5	Channel capacity with waterfilling benchmark scheme as a function	
of tra	ansmitter coordinates	96
4.6	NLOS channel capacity with waterfilling benchmark scheme	98
4.7	Transmit eigenvector field patterns in LOS blockage scenario	99
4.8	Channel capacity as a function average transmit power per antenna.	100
4.9	LOS channel capacity under TX beamsteering/RX MMSE scheme.	101
4.10	NLOS channel capacity under TX beamsteering/RX MMSE scheme.	103
4.11	Capacity-maximizing beamsteering directions in NLOS scenario	106
4.12	CDF of spectral efficiency using various transmitter alignments	107

## List of Tables

2.1	Sample array configurations	17
2.2	Link budget for SISO link	18
2.3	Normalized element positions for optimized nonuniform arrays	33
3.1	Link budget	72
3.2	SIR and BER Measurements	72

### Chapter 1

#### Introduction

With an abundance of unlicensed and uncrowded spectrum, the 60 GHz and E-band (71-76 GHz, 81-86 GHz) frequencies represent a frontier for modern wireless communications. The large swaths of available bandwidth allow wireless links to achieve unprecedented speeds. On the other hand, multi-Gbps data rates, hardware limitations, and mm wave propagation characteristics present system designers with a new set of challenges. Our goal in this dissertation is to design and evaluate practical architectures that address these challenges while capitalizing on the abundant spectrum. In particular, we investigate the feasibility of designing multi-antenna mm wave systems that employ spatial multiplexing to improve spectral efficiency and increase data rates.

Spatial multiplexing involves transmitting independent data streams in parallel over a multiple-input multiple-output (MIMO) channel. If the signals arrive at the receiver with sufficiently different spatial signatures, the transmitted signals can be separated out. Since it was first proposed by [1] and [2], spatial multiplexing has generated tremendous interest in the literature, and the technology has been successfully integrated with commercial products, such as 802.11n wireless local area network (WLAN) radios. While fundamental MIMO concepts are independent of the operating frequency, much of the existing MIMO literature makes assumptions about the wireless channel and hardware capabilities that may not hold at mm wavelengths. In particular, we identify several key characteristics that differentiate mm wave from lower frequencies (i.e. 1-5 GHz), including the following:

- Directionality: Assuming omnidirectional transmission, path loss scales as λ², resulting in a 22 dB loss at 60 GHz as compared to 5 GHz. Due to the limitations of today's mm wave devices, this loss cannot be offset simply by increasing transmit power. Instead, it necessitates the use of directional transmission. For antennas of a fixed aperture, directivity scales as 1/λ². Factoring in both the transmit and receive antennas, directional 60 GHz links end up with net gain of 1/λ².
- Sparse multipath: Measurement studies have observed relatively high reflection loss at mm wave frequencies, with multipath reflections tending to be more specular than diffuse [3] [4]. These observations, coupled with weak

diffraction characteristics and directional transmission, result in a channel with sparse, highly-attenuated multipath components.

- Large bandwidth: The 60 GHz band offers 7 GHz of unlicensed bandwidth in the United States, while the 70/80 GHz bands offer 10 GHz. While this allows for higher data rates, it also places an excessive burden on analog-to-digital converters (ADCs) and modern DSP-centric communication architectures. High-precision ADCs capable of sampling over several GHz of bandwidth are prohibitive in terms of cost, power consumption, or availability [5]. This requires us to consider system architectures and signal processing techniques that eliminate reliance on high-rate, high-precision ADCs.
- Additional hardware limitations: The difficulty of generating large amounts of transmit power using emerging silicon implementations drives us towards power-efficient communication (i.e., small constellations) over large bands (1-5 GHz). In contrast, the trend in MIMO systems at lower carrier frequencies is to use bandwidth-efficient communication over relatively narrow bands (20-40 MHz).

Throughout this work, our design choices are guided by these properties. We also take the potential applications of mm wave links into account, which include:

Long-range outdoor links: We assume long-range outdoor links operate in the 70/80 GHz bands, which avoid the high level of oxygen absorption that occurs near 60 GHz. Potential applications for outdoor mm wave links include wireless backhaul and high-speed mesh networks [6]. As an example of the speeds attainable by mm wave MIMO, consider a 1 km LOS link operating in the 71-76 GHz band, where a single 5 Gbps data stream can be achieved by a conservative design of QPSK with an excess bandwidth of 100%. By using four antennas each at the transmitter and the receiver, with inter-antenna spacing of about 1 meter, we can achieve four-fold spatial multiplexing. This yields a data rate of 20 Gbps, which can be further doubled by using dual polarization at each antenna, leading to an aggregate rate of 40 Gbps.

Short-range indoor links: Indoor applications of mm wave links include high-definition (HD) multimedia transmission and high-speed data sync. Single-antenna 60 GHz commercial products are currently entering the market, and standardization efforts include the recently published IEEE 802.15.3c-2009 [7] and ECMA-387 [8] standards, as well as emerging industry-backed specifications such as WiGig [9] and WirelessHD [10]. MIMO links would allow higher quality video streaming (i.e. faster framerates, higher color depth) and faster data sync.

The main contributions of this dissertation are summarized in the following sections.

# 1.1 LOS Spatial Multiplexing at mm Wave Frequencies

As mentioned above, the channels we consider have strong line-of-sight (LOS) components and sparse multipath due to antenna directionality and high reflection loss. As a result, we begin by focusing exclusively on the LOS channel component, and investigating its relationship to geometry of the transmit and receive antenna arrays. Spatial multiplexing over a LOS channel is possible assuming appropriate spacing between antenna elements [11]. Given knowledge of the link range and carrier frequency, a uniform linear or rectangular array can be designed that provides a spatially uncorrelated MIMO channel [12], [13]. We review this result before investigating how deviation from the nominal link range impacts system performance.

In scenarios of practical interest, a link may be deployed over an actual link range that differs from the nominal. When this occurs, the use of uniformly spaced arrays can result in a highly correlated, and even rank deficient, channel. In order to reduce the impact of spatial correlation over link ranges of interest, we consider the use of optimized non-uniform arrays, and show that suitably optimized non-uniform spacing of antennas can yield more robust performance than uniform arrays of the same size.

In the event that the channel becomes highly correlated, the receiver may be unable to recover the transmitted signals. We propose a rank adaptation scheme that adjusts the number of transmitted signals based on the extent of channel correlation. The performance of this scheme is evaluated through simulation and, despite the sub-optimal nature of its implementation, is shown to offer reasonable performance in comparison to the channel capacity.

## 1.2 Hierarchical MIMO Signal Processing: Architecture and Prototype

Since high-precision ADCs become a limiting factor as bandwidths scale up to multiple GHz, we require novel architectures and signal processing methods that avoid this bottleneck. For some tasks, such as the demodulation of small-constellation signals, low-precision (1-3 bits) ADCs may suffice. Other receiver processing, including conventional channel estimation methods, high-precision sampling is a prerequisite. To this end, we propose a hierarchical approach that decouples the signal processing tasks of spatial equalization and signal demodulation. The linear spatial equalizer at the receiver adapts its coefficients by monitoring low-frequency pilot tones embedded in the transmitted signals. Equalization is performed at baseband using analog hardware. The recovered signals at the output

of the equalizer can then be sampled at the full rate with low precision and demodulated.

Three methods of choosing the spatial equalizer coefficients are considered. The first two compute an explicit channel estimate, which in turn can be used to estimate the zero-forcing (ZF) or minimum mean squared error (MMSE) equalizer coefficients. The third approach adapts the equalizer weights iteratively based on feedback from the output of the equalizer. The three methods are described in detail and their performance is evaluated through simulation.

We then describe a 60 GHz mm wave MIMO prototype built at UCSB by Dr. Colin Sheldon with assistance from Dr. Munkyo Seo and the author. The prototype provides a proof of concept for LOS spatial multiplexing, and achieves an aggregate data rate of 2.4 Gbps by multiplexing four channels at 600 Mbps. It has demonstrated the feasibility of LOS spatial multiplexing both outdoors [14] over 41 m range, and indoors over 5 m [15]. Spatial equalization was implemented at baseband using analog components and an adaptive controller capable of monitoring the embedded low-frequency pilot tones. The prototype was designed to operate at 60 GHz due to the widespread availability of 60 GHz components and fewer regulations relative to the E-band. Specifically, the FCC requires that links operating in the 71-76 GHz or 81-86 GHz bands are registered and have anten-

nas with a minimum directivity of 43 dBi and a maximum beamwidth of 1.6°. Experimental results are provided and discussed.

## 1.3 Feasibility and Performance Study of Indoor mm Wave MIMO Links

While it has been shown that suitably choosing antenna spacing produces orthogonal eigenmodes for LOS spatial multiplexing, we show here, for the example of linear arrays, that this strategy is effectively optimal in terms of maximizing the number of degrees of freedom for a given array length. Our analysis is based on the limit of a continuous linear array, where the channel spatial eigenmodes are prolate spheroidal waveforms, analogous to the classical analysis of time- and band-limited systems.

We then evaluate the performance of an array of subarrays architecture, where the subarrays provide beamsteering gains, and are spaced to provide spatial multiplexing gains with eigenmodes which are orthogonal for a LOS link at a nominal range. We evaluate its performance in the sparse multipath environment resulting from highly directive transmissions using geometrical optics (i.e., ray tracing) to model the channel, with a view to quantifying variations in performance with the relative location of transmitter and receiver, and with LOS blockage. We compare a waterfilling benchmark against a strategy with independent transmit beamsteering for each subarray, together with linear MMSE spatial interference suppression at the receiver. Our numerical results provide insight into how the spatial eigenmodes and the achievable capacity vary with the propagation environment. We conclude that the spatial multiplexing gain provided by our architecture is robust to LOS blockage and to variations in the locations of the transmitter and receiver within the room, while requiring a reasonably small power per transmit element realizable by low-cost CMOS processes.

#### 1.4 Related Work

Interest in mm wave communications has been prompted, in part, by recent advances in mm wave IC design. 60 GHz and E-band ICs have been demonstrated in CMOS technology [16] [17] [18] [19], and integrated mm-wave phased-array ICs have been demonstrated in CMOS and SiGe technologies [20] [21]. Progress in IC design have been accompanied by system-level advances. The authors of [22] describe a 6-Gbit/s link operating in the 81-86 GHz frequency band achieving a spectral efficiency of 2.4-bit/s/Hz. This system uses frequency-domain multichannel multiplexing to achieve the given spectral efficiency. This is complementary

to the approach described herein, which increases spectral efficiency through the use of spatial multiplexing.

The number of spatial degrees of freedom of a MIMO channel given array aperture constraints was previously evaluated in [23] in the context of a scattering environment. Their derivation uses the plane wave approximation, which holds when antenna spacing is small relative to the wavelength, in which case a LOS channel is limited to a single spatial degree of freedom. Our interest here is in antennas with larger antenna spacing (feasible because the wavelength is so small), where purely LOS channels can indeed offer multiple degrees of freedom. The capacity of LOS MIMO channels was previously studied by several authors [11], [24], [13], [12], with a view to identifying the optimal antenna array geometries that maximize the LOS channel capacity. In this paper, we show that such geometries are indeed near-optimal in terms of degrees of freedom maximization, given a constraint on the node form factor.

### Chapter 2

## LOS Spatial Multiplexing Over Millimeter-Wave Links

Multiple-input, multiple-output processing involves multiplexing multiple independent signals in the spatial dimension, thereby increasing throughput without requiring increased bandwidth or transmit power. In this chapter, we consider applying MIMO processing to mm-wave links operating in the 60 GHz and 75-85 GHz frequency ranges. In particular, noting that the mm-wave channel is typically dominated by a line-of-sight component, we investigate spatial multiplexing over a LOS MIMO channel. While conventional MIMO channel models often assume independent random gains between antennas, representative of a rich multipath environment, the LOS MIMO channel is determined by the geometry and alignment of the antenna arrays at each node. As such, the arrays should be designed with the goal of producing a robust full-rank channel.

We begin this chapter by reviewing the LOS MIMO channel model and deriving the antenna geometry that maximizes capacity over this channel. We then consider these results in the context of mm-wave systems. In Section 2.2, we investigate the effect of spatial correlation on system performance, motivating the study of nonuniform linear arrays in Section 2.3. We find that, in comparison to uniform linear arrays, nonuniform arrays can be made less susceptible to spatial correlation and channel rank deficiency. In Section 2.4, we discuss a rank adaptation strategy designed to maintain high throughput if the channel becomes highly correlated. We conclude with Section 2.5.

#### 2.1 LOS Spatial Multiplexing

Several characteristics of the 60 GHz and 75/85 GHz bands distinguish mm-wave communication from wireless communication at lower frequencies. For instance, mm-wave links may be directional by necessity, due to the fact that, for omnidirectional transmission, path loss scales as  $\lambda^{-2}$ , where  $\lambda$  is the carrier wavelength. This amounts to a 22 dB loss at 60 GHz as compared to 5 GHz, which can be offset through the use of directional antennas and/or antenna arrays. Given a fixed antenna aperture area, directivity scales as  $\lambda^{-2}$ , resulting in a net gain of  $\lambda^{-2}$  when the transmit and receive antennas are both taken into account.

Conventional MIMO links rely on a rich scattering environment to ensure that transmitted signals arrive at the receiver with different enough spatial signatures that they can be separated out through spatial processing. But as a result of using highly directional antennas, in addition to higher reflection loss at mm-wavelengths, multipath is attenuated and the LOS channel component is dominant (assuming it is unobstructed). Multiplexing over LOS channels is possible if antenna arrays are of sufficient size. In this section, we derive the optimal antenna spacing that maximizes capacity over the LOS MIMO channel.

#### 2.1.1 LOS MIMO Channel Model

Consider a point-to-point LOS link with an N-element antenna array at each node. Assuming no temporal intersymbol interference, which is a reasonable approximation given the narrow beams radiated by highly directive antennas, the  $N \times 1$  received signal vector  $\mathbf{r}$  is given by

$$\mathbf{r} = \mathbf{H}\mathbf{s} + \mathbf{n},\tag{2.1}$$

where **s** is the  $N \times 1$  transmitted vector, **n** is an  $N \times 1$  zero mean circularly symmetric complex white Gaussian noise vector with covariance  $R_n = 2\sigma^2 \mathbf{I}_N$  and  $\mathbf{I}_N$  is the  $N \times N$  identity matrix. **H** is an  $N \times N$  channel matrix with entries  $h_{m,n}$  corresponding to the complex channel gain from the nth transmit element

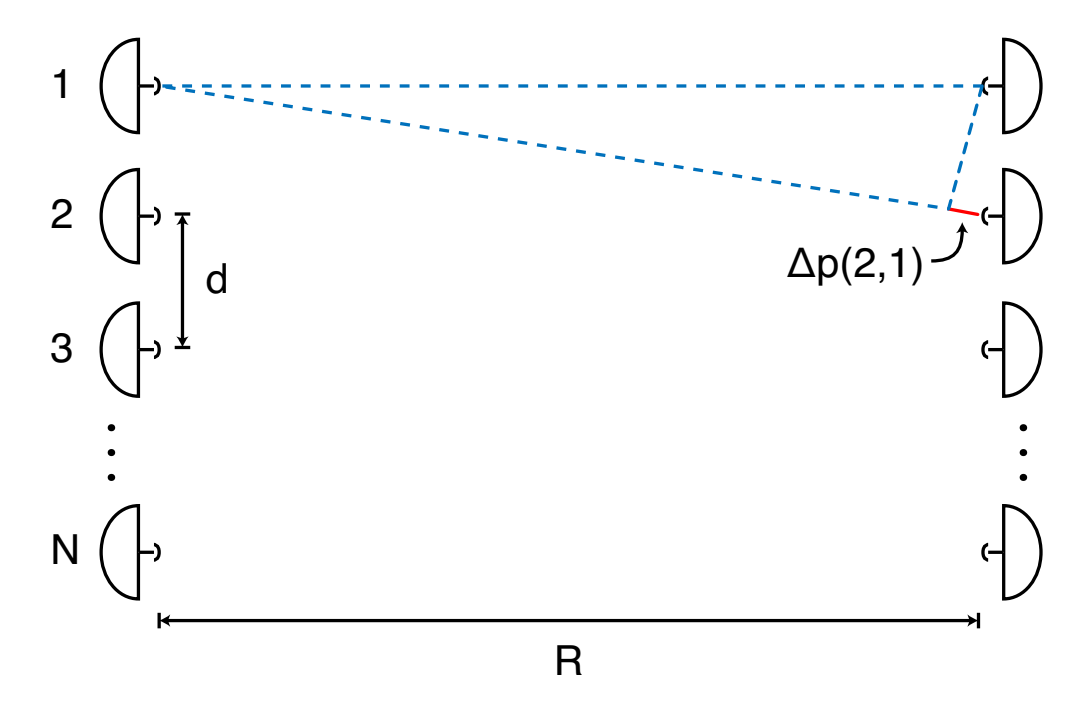


Figure 2.1: Aligned uniform linear arrays.

to the mth receive element. Assuming a strictly LOS channel with no signal path loss (the loss is accounted for in the link budget), the elements of the channel matrix are given by  $\tilde{h}_{m,n} = e^{-j2\pi p(m,n)/\lambda}$ , where p(m,n) is the path length from nth transmit element to the mth receive element and  $\lambda$  is the carrier wavelength. Only the relative phase shifts between elements of  $\mathbf{H}$  are of interest, so for notational convenience we normalize  $\tilde{h}_{m,n}$  by a factor of  $e^{j2\pi R/\lambda}$ , resulting in

$$h_{m,n} = e^{-j2\pi(p(m,n)-R)/\lambda} = e^{-j2\pi\Delta p(m,n)/\lambda}, \qquad (2.2)$$

where  $\Delta p(m, n) = p(m, n) - R$ .

Specializing to linear arrays aligned to the broadside of each other, as shown in Fig. 2.1, let  $\mathbf{x} = [x_1, x_2, \dots, x_N]$  specify the positions of the N array elements relative to the top of the array, i.e.  $x_1 = 0$  and  $x_N = L$ , where L is the total length of the array.  $\Delta p(m, n)$  can now be expressed as

$$\Delta p(m,n) = \sqrt{(x_m - x_n)^2 + R^2} - R \approx \frac{(x_m - x_n)^2}{2R},$$
(2.3)

with the approximation holding for  $|x_m - x_n| \ll R$ . The entries of the channel matrix can be approximated as

$$h_{m,n} \approx e^{-j\pi(x_m - x_n)^2/(R\lambda)}. (2.4)$$

Given  $\lambda$  and R, it is possible to position the array elements such that each column of  $\mathbf{H}$  is orthogonal to every other column. This allows all N signals to be recovered without any suffering performance degradation due to spatial interference. In the next section, we review an array design which meets this criteria.

#### 2.1.2 The Rayleigh Spacing Criterion

Consider the simple example of two N-element uniform linear arrays (ULAs) aligned to the broadside of each other as in Fig. 2.1. Assume the link range is known, and given by  $R_o$ . The spacing between adjacent elements is d, resulting in a position vector of  $\mathbf{x} = [0, d, 2d, \dots, (N-1)d]$ . The path length difference

(relative to  $R_o$ ) is given by

$$\Delta p(m,n) \approx (m-n)^2 \frac{d^2}{2R_o},\tag{2.5}$$

where  $(m-n)d \ll R_o$ . The entries of the channel matrix are given by

$$h(m,n) \approx e^{-j(m-n)^2 \pi d^2/(\lambda R_o)} = e^{-j(m-n)^2 \phi},$$
 (2.6)

where  $\phi = \pi d^2/(\lambda R_o)$  is the phase difference between neighboring elements. The correlation between the receive array responses to the kth transmit element and the mth transmit element, with  $k \neq m$ , is given by

$$\rho(k,m) = \frac{|\mathbf{h}_{k}^{H} \mathbf{h}_{m}|}{\|\mathbf{h}_{k}\| \|\mathbf{h}_{m}\|} 
= \frac{1}{N} \left| \sum_{n=0}^{N-1} e^{-j((k-n-1)^{2} - (m-n-1)^{2})\phi} \right| 
= \frac{1}{N} \left| \frac{\sin(N(k-m)\phi)}{\sin((k-m)\phi)} \right| 
= \rho(k-m), \quad k, m \in \{1, 2, \dots, N\},$$
(2.7)

where  $\mathbf{h}_k$  is the kth column of  $\mathbf{H}$ . From Eq. (2.7), we observe that the correlation is driven to zero when  $N\phi = \pi$ . Substituting this result into Eq. (2.5), we obtain the optimal uniform spacing

$$d_{\rm R} = \sqrt{\frac{R_o \lambda}{N}}. (2.8)$$

More generally, if the transmit and receive arrays have interelement spacings given by  $d_t$  and  $d_r$ , respectively, it can be shown [12] that the optimal spacings satisfy

$$d_t d_r = \frac{R_o \lambda}{N}. (2.9)$$

Table 2.1: Sample array configurations. Lengths given in meters.

$R_o$	N=2	N = 3	N=4
1 km	1.41	2.31	3.00
$100 \mathrm{m}$	0.44	0.73	0.95
5  m	0.11	0.18	0.23

Eq. (2.9) also specifies the optimal element spacing of  $N \times N$  uniform square arrays aligned broadside [13].

We refer to (2.9) as the Rayleigh spacing criterion. In the field of diffraction limited optics, the Rayleigh criterion states an imaging array consisting of N elements spaced distance  $d_r$  apart has an angular resolution of  $\theta_R \approx \lambda/(d_r N)$ . Two distant objects a distance R from the imaging array, and a distance  $d_t \ll R$  from one other, have angular separation  $\theta_T \approx d_T/R$ . In order to resolve the objects, it is required that  $\theta_T \geq \theta_R$ . Equating the two quantities, we arrive at the same condition given in (2.9).

A more general expression for the optimal uniform spacing is provided by Bohagen *et al.* in [25] [12], where authors consider linear and rectangular arrays facing arbitrary directions.

#### 2.1.3 Application to mm-Wave Links

The length of a Rayleigh spaced array scales in proportion to  $\sqrt{\lambda}$ . While this results in impractically large arrays at lower frequencies, arrays are more moderately

Table 2.2: Link budget for SISO link.

Carrier Frequency	75	GHz
Bitrate	5	Gbps
Excess bandwidth	100%	
BER	$10^{-9}$	
TX antenna gain	45	$\mathrm{dBi}$
RX antenna gain	45	$\mathrm{dBi}$
Link range	1	$\mathrm{km}$
Free-space path loss	129	dB
Atmospheric loss	11.94	dB
Rx noise figure	6.5	dB
Link margin	25	dB
Tx Power	21.9	dBm
Rx Power	-23.0	dBm

sized at mm wavelengths. Table 2.1 lists the lengths of sample array configurations for 5 m, 100 m, and 1 km link ranges. It is assumed that the 100 m and 1 km links operate at 75 GHz to avoid peak in oxygen absorption loss found at 60 GHz. The 5 m range, representative of an indoor link, operates at 60 GHz. We observe outdoor links are of suitable size for rooftop or tower deployments, while the indoor arrays could be integrated into consumer electronic devices such as televisions or set-top boxes.

We can also consider square arrays with  $N^2$  elements, in which case Table 2.1 lists the length per side of the array. Rayleigh-spaced square arrays are capable of sending  $N^2$  data streams in parallel.

#### Sample link budget:

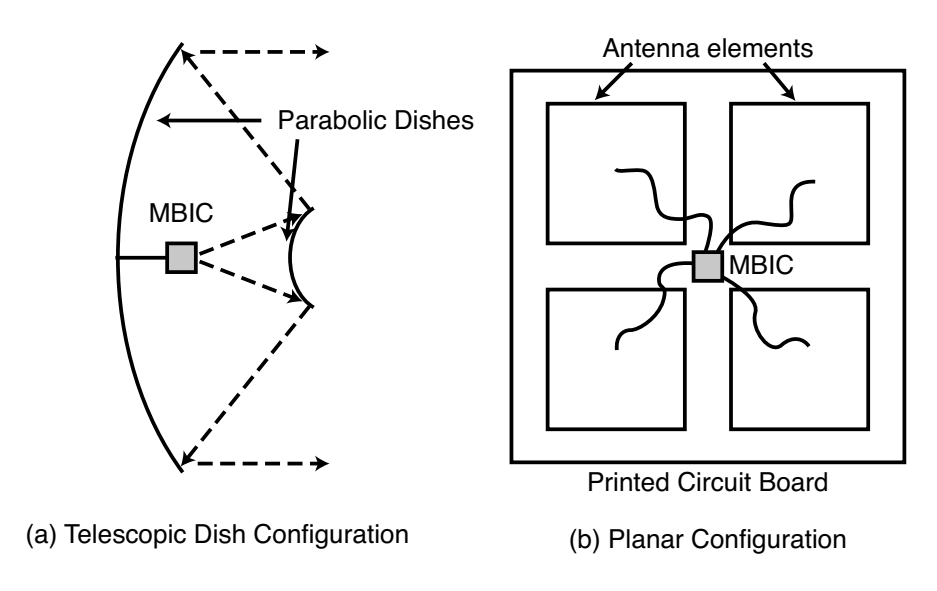


Figure 2.2: Subarray configurations.

Long-range mm-wave links face several implementation challenges, including high path loss, as mentioned previously, and limited power output from mm-wave RF devices. These limitations can be overcome through the use of highly directional antennas or beamforming antenna arrays. Antenna arrays offer beamsteering capability and require less power per element. Half-wavelength arrays can be implemented as monolothic beamsteering integrated circuits (MBICs) at 60 GHz due to the small wavelength, but they have insufficient aperture to provide directivity required for a long-range link. One alternative is to use a MBIC as the feed for a parabolic dish or planar circuit board antenna, as shown in Fig. 2.2, which increases directivity while retaining some beamsteering capability. This is the approach we adopt in the following link budget analysis.

To evaluate the feasibility of long-range mm-wave links, we compute the link budget for a 5 Gbps 75 GHz single-input single-output (SISO) link with a 1 km link range. Each antenna consists of a beamsteering  $4 \times 4$  square array (which we refer to as a subarray, to distinguish it from a larger Rayleigh-spaced array) mounted on a 30 cm diameter dish antenna with a  $2^{\circ}$  beamwidth, providing a directivity of G = 45dB.

The minimum received power is given  $P_{RX} = Q^2 k_b T F B$ , where  $k_B$  is the Boltzmann constant, T is the temperature, F is the received noise figure, B is the bandwidth, and Q = 6 for QPSK with an uncoded bit error rate of  $10^{-9}$ . The bandwidth is 5 GHz assuming QPSK modulation with 100% excess bandwidth. The received power according to Friis' transmission equation is

$$\frac{P_{RX}}{P_{TX}} = \frac{G_T G_R \lambda}{16\pi R^2} e^{-\alpha R} \tag{2.10}$$

where  $\alpha$  is atmospheric attenuation, which dominates over the  $(\lambda/R)^2$  in foul weather conditions. We allow for heavy rain by setting  $\alpha = 11.94$  dB/km [26], [27].

The resulting link budget is summarized in Table 2.2. Including a 25 dB link margin, we find that the link can be maintained using 160 mW transmit power at each subarray, or 10 mW per subarray element. This SISO link forms the building block of a larger MIMO link, which can reduce the required transmit power further through array processing gains. These calculations support the notion that long

range links are feasible using moderate transmit power per element. The "array of subarrays" approach is applied to indoor links in Chapter 4.

#### 2.2 Spatial Correlation at Non-Optimal Link

#### Ranges

When the Rayleigh criterion is met, the channel matrix is scaled unitary and the (noisy) transmitted signal vector  $\mathbf{s}$  can be recovered through spatial equalization without suffering degradation of the signal-to-noise (SNR) ratio. However, when the link operates at a range  $R \neq R_o$ , correlation will be present among columns of  $\mathbf{H}$  and spatial equalization can cause an increase in noise power. This is likely to occur in practice, because the precise link range R may be unknown during the design and manufacture of an array.

Consider a 4-element ULA array. Fig. 2.3 plots the correlation  $\rho(k-m)$  of the receive array responses to transmit elements k and m as the link range is varied from  $R=0.2R_o$  to  $R=R_o$ .  $\rho(1)$  is the correlation between adjacent columns of  $\mathbf{H}$ , i.e. correlation among the receive array responses to neighboring transmit elements. Similarly,  $\rho(2)$  corresponds to transmit elements separated by 2d. Hence, it represents correlation between responses to the first and third transmit elements or the second and fourth transmit elements. Finally,  $\rho(3)$  corresponds to

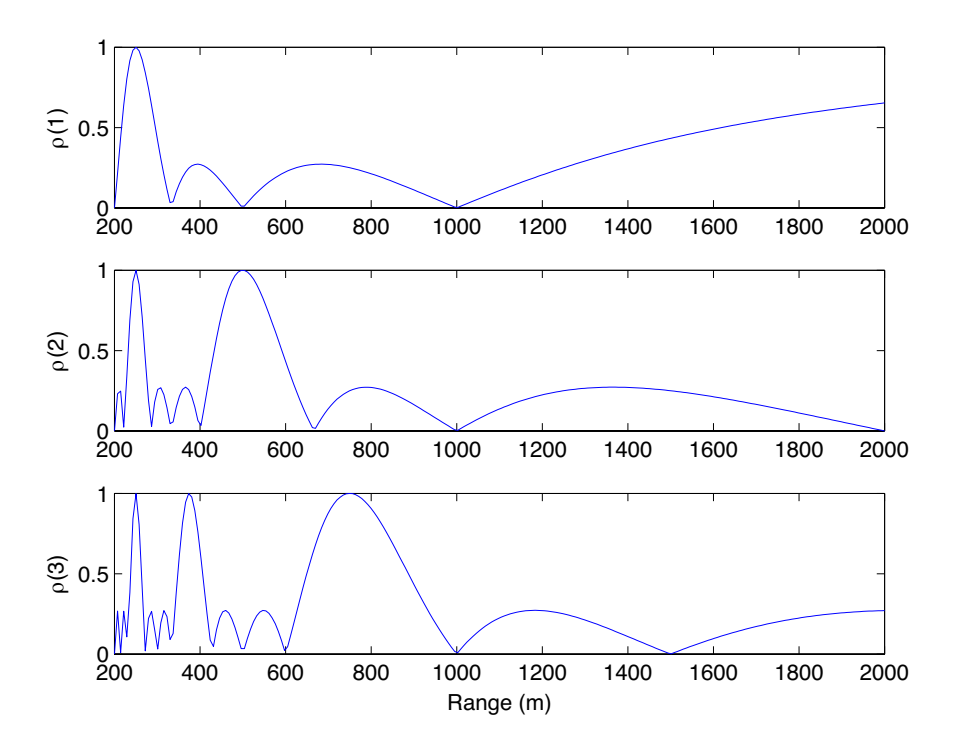


Figure 2.3: Correlation among columns of  $\mathbf{H}$  as a function of link range for a 4-element Rayleigh-spaced array.

transmit elements separated by distance 3d, i.e. the outermost elements transmit array.

At some values of R, the correlation between two or more columns of  $\mathbf{H}$  approaches unity, in which case the channel matrix becomes ill-conditioned. For instance, when  $R = \frac{d^2}{\lambda} = \frac{R_{\rm RC}}{N}$  the phase difference between adjacent receive elements is  $\phi = \pi$  and  $\mathbf{H}$  becomes rank one. In general, from Eq. (2.7) we find that  $\rho(n)$  goes to unity whenever R takes on the values

$$R = \frac{n}{kN}R_o, \qquad k = 1, 2, 3, \dots,$$
 (2.11)

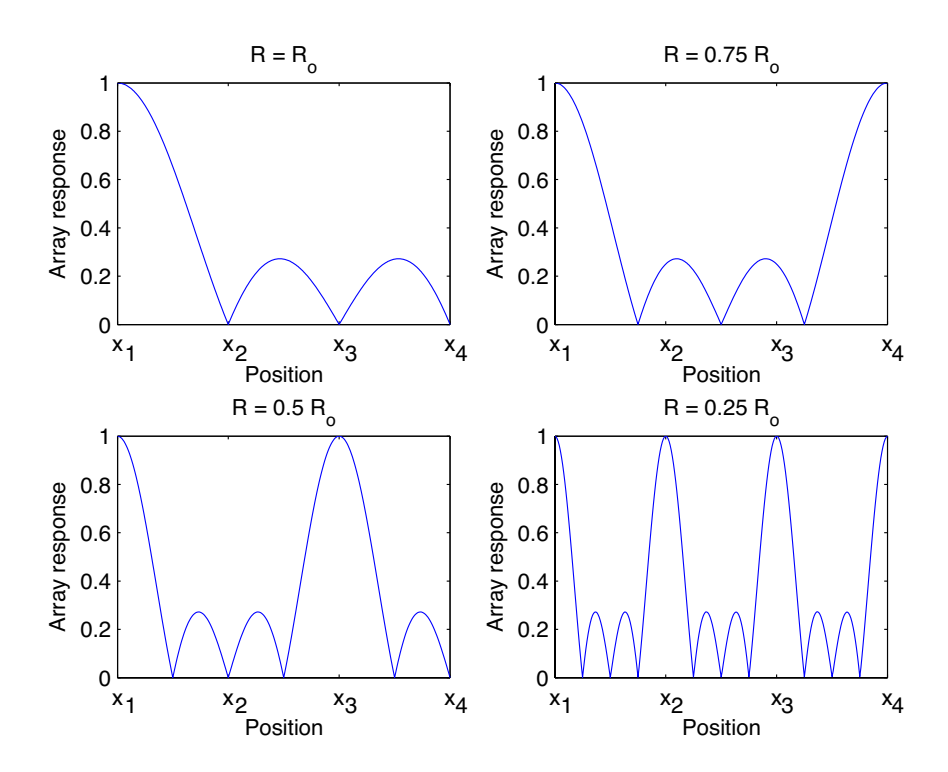


Figure 2.4: Array response at various link ranges.

for n = 1, 2, ..., N-1. This equation specifies the link ranges at which **H** becomes ill-conditioned for both Rayleigh-spaced N-element ULAs and Rayleigh-spaced  $N \times N$ -element square arrays. According to Eq. (2.11), as R deviates from  $R_o$ , correlation among columns of **H** first reaches unity at  $R = \frac{N-1}{N}R_o$ . At this distance, the receive array responses to the outermost transmit elements become perfectly correlated.

Spatial correlation can also be considered in relation to the array response. Assume the receiver is steering (i.e. through electronic phase adjustment) in the direction of the first transmit element. Fig. 2.4 plots the receiver's array response to a point source source moving across the line connecting the transmit elements. When  $R = R_0$  and the Rayleigh criterion is satisfied, the interfering transmitters fall into nulls in the array pattern. At R = 0.75, however, the fourth transmit element falls within a grating lobe of the receive array response, which accounts for the high value of  $\rho(3)$  at this link range. Similarly, the third element falls within a grating lobe at  $R = R_0/2$ , and all elements coincide with grating lobes at  $R = R_0/4$ .

#### 2.2.1 Noise Enhancement at Non-Optimal Link Ranges

To assess the impact of spatial correlation on system performance, we will consider the output of a zero-forcing (ZF) spatial equalizer. The ZF equalizer cancels out spatial interference entirely by filtering the received signal vector by the pseudoinverse of the channel matrix, given by

$$\mathbf{C}_{\mathbf{ZF}} = \mathbf{H}^{\dagger} = \mathbf{H}^{H} (\mathbf{H} \mathbf{H}^{H})^{-1}. \tag{2.12}$$

**H** is typically invertible (although possibly ill-conditioned), in which case the pseudo-inverse and inverse coincide. The output of the zero-forcing equalizer is

$$\mathbf{y} = \mathbf{C}_{\mathrm{ZF}} \left( \mathbf{H} \mathbf{s} + \mathbf{n} \right) = \mathbf{s} + \tilde{\mathbf{n}}, \tag{2.13}$$

where  $\tilde{\mathbf{n}}$  is an  $N \times 1$  complex Gaussian noise vector with covariance  $2\sigma^2 \mathbf{C}_{\mathrm{ZF}}^H \mathbf{C}_{\mathrm{ZF}}$ . The ZF equalizer eliminates spatial interference entirely at the cost of an increase

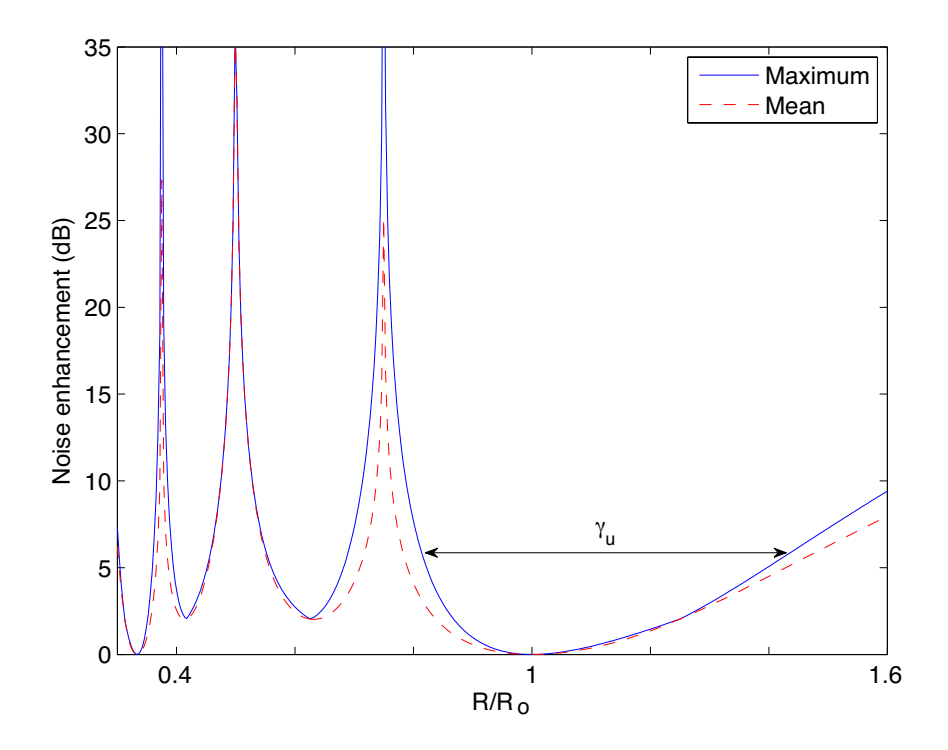


Figure 2.5: Noise enhancement as a function of range.

in noise power, referred to as noise enhancement. For a given array configuration  $\mathbf{x}$ , the noise enhancement incurred by the *i*th transmitted signal is given by

$$\eta_i(\mathbf{x}, R) = \|\mathbf{h}_i\|^2 \|\mathbf{c}_i\|^2 = N \|\mathbf{c}_i\|^2,$$
 (2.14)

where  $\mathbf{c_i}$  is the *i*th column of  $\mathbf{C}_{\mathrm{ZF}}$  and the dependence of  $\mathbf{c}_i$  on  $\mathbf{x}$  and R is implicit. The mean noise enhancement is given by

$$\bar{\eta}(\mathbf{x}, R) = \frac{1}{N} \sum_{i=1}^{N} \eta_i(R) = \sum_{i=1}^{N} \frac{1}{\lambda_i^2},$$
 (2.15)

where  $\lambda_i$  are the singular values of **H** evaluated at R.

Fig. 2.5 plots the mean noise enhancement,  $\bar{\eta}(\mathbf{x}_u, R)$ , and the maximum noise enhancement,  $\max_i \eta_i(\mathbf{x}_u, R)$ , of the 4-element Rayleigh-spaced array. Note that noise enhancement increases as soon as R deviates from  $R_o$ . A link budget analysis suggests that, even under unfavorable weather conditions, the link margin can be set as high as 10 to 20 dB [28]. A portion of the link margin can be allocated to offsetting the effects of noise enhancement. However, the noise enhancement far exceeds the entire link margin at ranges of 375 m, 500 m, and 750 m, i.e. at ranges given by Eq. (2.11) where the correlation among columns of  $\mathbf{H}$  approaches unity.

Although other spatial equalization methods (eigenchannel transmission, BLAST, and MMSE) could be considered, these schemes suffer performance degradation at the same link ranges as the ZF receiver due to spatial correlation in the channel. In particular, MMSE and ZF equalization give similar performance at moderate to high SNRs, with the MMSE receiver tending to the ZF receiver asymptotically as the SNR gets large. Thus we focus on noise enhancement as a simple SNR-independent metric of array performance.

In the the following section, we consider the use of optimized nonuniform arrays that sacrifice optimality at  $R_o$  to provide acceptable performance over a larger set of link ranges. By breaking the uniformity of the array, the noise enhancement spikes closest to  $R_o$  can be avoided.

#### 2.3 Optimized Nonuniform Arrays

Let  $[R_1, R_2]$  denote the interval about  $R_o$  for which the maximum noise enhancement remains below a given threshold  $\eta$ . Defining  $\gamma = R_2 - R_1$ , the goal of our optimization will be to find a nonuniform linear array that maximizes  $\gamma$ . We denote the maximum value by  $\gamma_o$  and define  $\gamma_u$  as the value of our metric when using Rayleigh-spaced uniform arrays. For example, consider the four-element uniform array optimized for some link range  $R_o$ . Setting  $\eta = 6$  dB, we have  $R_1 = .8R_o$  and  $R_2 = 1.4R_o$ , as shown in Fig. 2.5. The link will operate reliably given  $R/R_o \in [0.8, 1.4]$ , corresponding to  $\gamma_u = 0.6$ .

#### 2.3.1 4-element Nonuniform Array Analysis

To gain insight into the optimization problem, we begin with 4-element Rayleigh-spaced arrays at both ends of the link. The array is optimized for link range  $R_o$ . Keeping the outer two elements fixed, we allow the inner two elements to shift inward or outward in position by an equal amount, maintaining symmetry about the center of the array. The element positions are given by  $\mathbf{x} = [0, \alpha d_R, (3 - \alpha)d_R, 3d_R]$ , with  $\alpha = 1$  corresponding to the original Rayleigh-spaced array.

As shown by Fig. 2.5,  $\gamma_u$  is limited by the rightmost spike in noise enhancement, which occurs at  $3R_o/4$ . This spike is the result of high correlation between

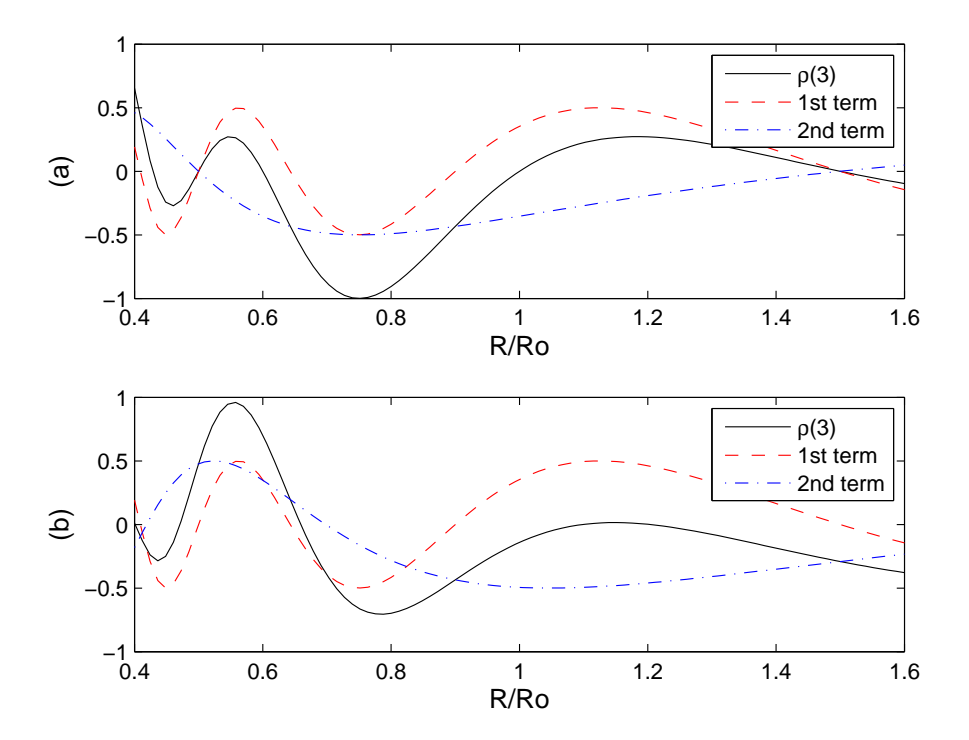


Figure 2.6: Correlation  $\rho(1,4)$  corresponding to signals from the outermost elements of the transmit array. In the top plot,  $\alpha = 1$ . In the bottom plot,  $\alpha = 0.80$ .

the first and fourth columns of  $\mathbf{H}$ , corresponding to the outer transmit elements. Allowing the correlation to take on values in [-1,1],  $\rho(1,4)$  can be expressed as a

sum of cosines as follows

$$\rho(1,4) = \frac{1}{2}\cos\left(\frac{9\pi R_o}{4R}\right) + \frac{1}{2}\cos\left(\frac{3\pi R_o}{4R}(3+2\alpha)\right). \tag{2.16}$$

The individual terms and their sum are displayed in the top plot of Fig. 2.6 for  $\alpha = 1$ . We observe that  $\rho(1,4) = -1$  at  $3R_o/4$ , resulting in a noise enhancement spike as expected.

The first term, plotted as a dashed line, is independent of the choice of  $\alpha$  while the second term is dependent. We can predict that a good choice of  $\alpha$  is one that avoids coinciding positive or negative peaks among the cosine terms in the range interval of interest.

Setting  $\eta=6$  dB, the the metric  $\gamma$  has been computed numerically for  $\alpha\in[0,1.5]$ , with the results shown in Fig. 2.7. We find that the nonuniform array outperforms the Rayleigh-spaced array for any values of  $\alpha$  between 0.45 and 1. The optimal value occurs at  $\alpha=0.802$ . Although not shown, the correlations  $\rho(1,2)$  and  $\rho(3,4)$  grow large for  $\alpha<0.5$ , resulting in a low value of  $\gamma$ . This is as expected, because the receiver has difficulty resolving the inner and outer elements when they are placed close together.

As shown in the Fig. 2.6, the optimal value of  $\alpha$  reduces  $\rho(3)$  at values of R surrounding  $R_o$ . This provides an intuitive notion of what constitutes a good nonuniform array, however, it also highlights the complexity of the problem. First, the distance between adjacent peaks of each cosine term shrinks as R decreases, thus it becomes increasingly difficult to ensure that peaks do not coincide as R decreases. In fact, even in the optimized case, negative peaks coincide at R = 500 m, resulting in a sharp spike in noise enhancement at this range. Second, we have constrained ourselves to a nonuniform array that is symmetric about the center

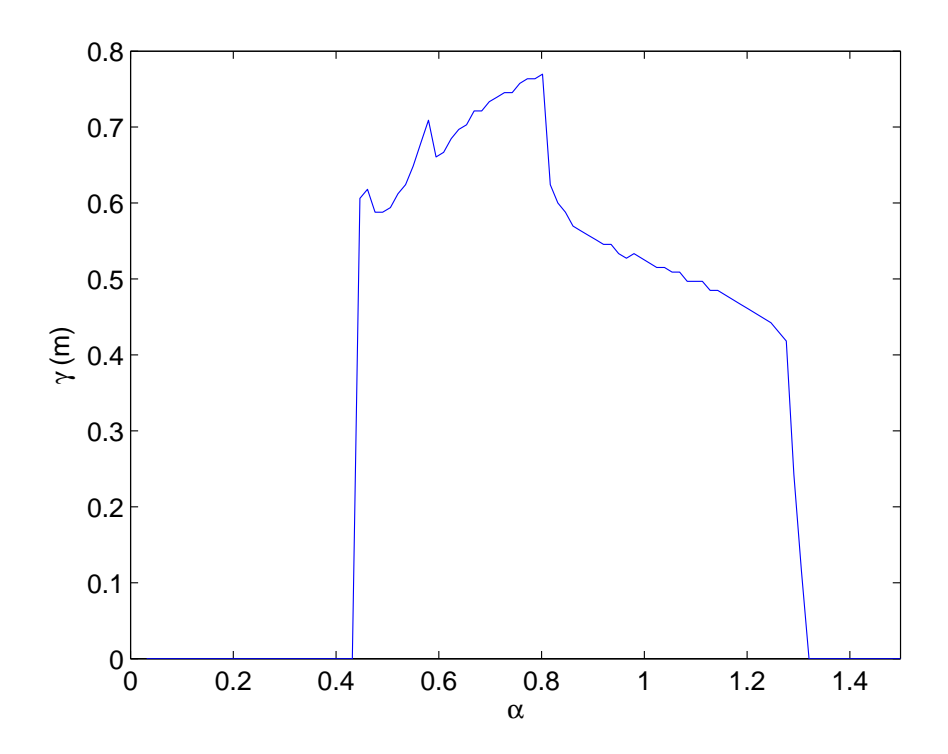


Figure 2.7: Optimization metric  $\gamma$  for symmetric 4-element array.

of the array. Asymmetric arrays may perform significantly better, although they are considerably more difficult to characterize analytically.

Based on these factors, we proceed to perform a numerical optimization of asymmetric nonuniform arrays. Because the number of elements in a mm-wave MIMO array is limited by practical constraints on the array's physical size, exhaustive search for optimal positions remains a computationally feasible option.

## 2.3.2 Optimization Procedure and Results

The optimization procedure is first performed on a 4-element array with an expected link range of  $R_o = 1$  km. Our optimization goal is to maximize  $\gamma = R_2 - R_1$ , where  $[R_1, R_2]$  is the interval about  $R_o$  on which the noise enhancement remains below  $\eta = 6$  dB. The array length is fixed at  $L = 3d_R$ , i.e. the length of a 4-element Rayleigh spaced optimized for a link range of  $R_o$ . The antenna position vector is given by  $\mathbf{x} = [0, x_2, x_3, 3d_R]$  with  $x_2 \in [0, 1.5d_R]$  and  $x_3 \in [1.5d_R, 3d_R]$ . The optimal element positions, determined through exhaustive search, are given by  $\mathbf{x}_o = [0, 0.87d_R, 2.36d_R, 3d_R]$ . In Fig. 2.8, we plot the mean SNR gain (normalized to 0 dB at  $R_o$ ), defined as

$$SNR(R) = \left(\frac{R_o}{R}\right)^2 \bar{\eta}(\mathbf{x}_o, R),$$

where the factor  $(R_o/R)^2$  accounts for path loss. We note that while the maximum link range is slightly decreased, the nonuniform array eliminates large spikes in the noise enhancement completely and could be used over a much wider set of link ranges without concern that the SNR would dip below an acceptable level.

The procedure was repeated for a 5-element array with  $\eta$  increased to 6.97 dB to account for the additional receive array processing gain provided by the extra array element. Fig. 2.9 plots the resulting normalized SNR. Similarly, a 6-element array was optimized with  $\eta = 7.76$  dB, and the normalized SNR is plotted in Fig.

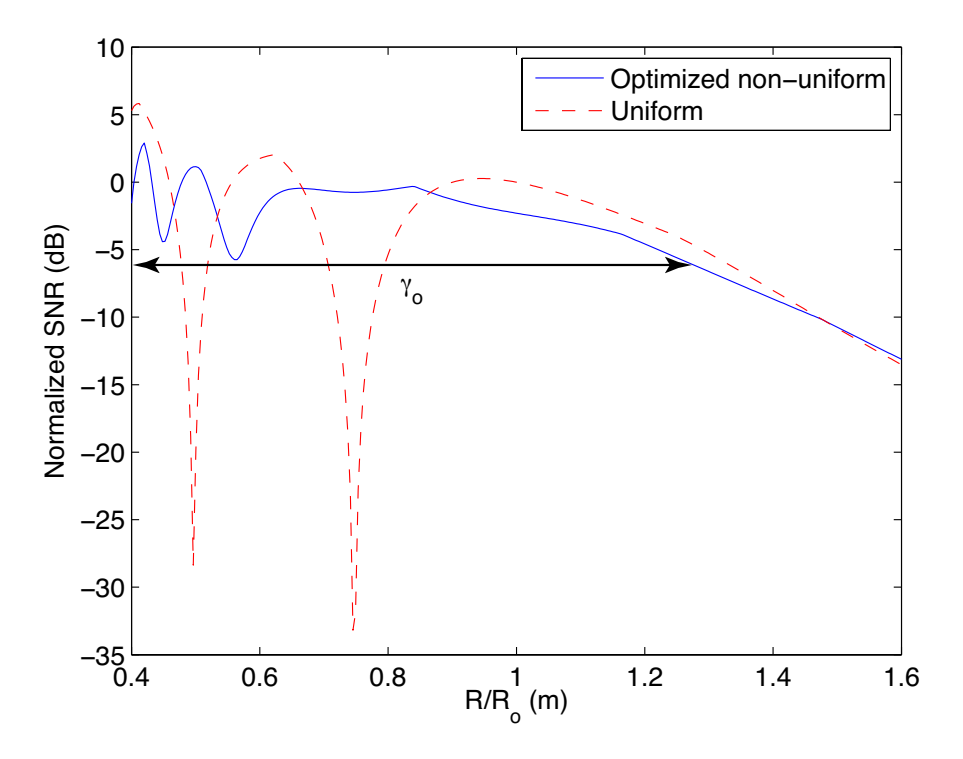


Figure 2.8: Maximum noise enhancement as a function of range for an optimized 4-element array.

2.10. In both cases  $\gamma_o$  provides a significant improvement over  $\gamma_u$ . The optimized antenna positions are for 3, 4, and 5-element arrays normalized to unit length are provided in Table 2.3.

We observe that  $\gamma_u$  decreases by roughly 20% with each additional array element,  $\gamma_o$  remains nearly constant. This trend suggests that the benefit of nonuniform optimization grows with increasing N. We note that during optimization, we assumed the arrays were aligned, and non-uniform arrays may not necessarily perform better than uniform arrays when the arrays are misaligned. As such,

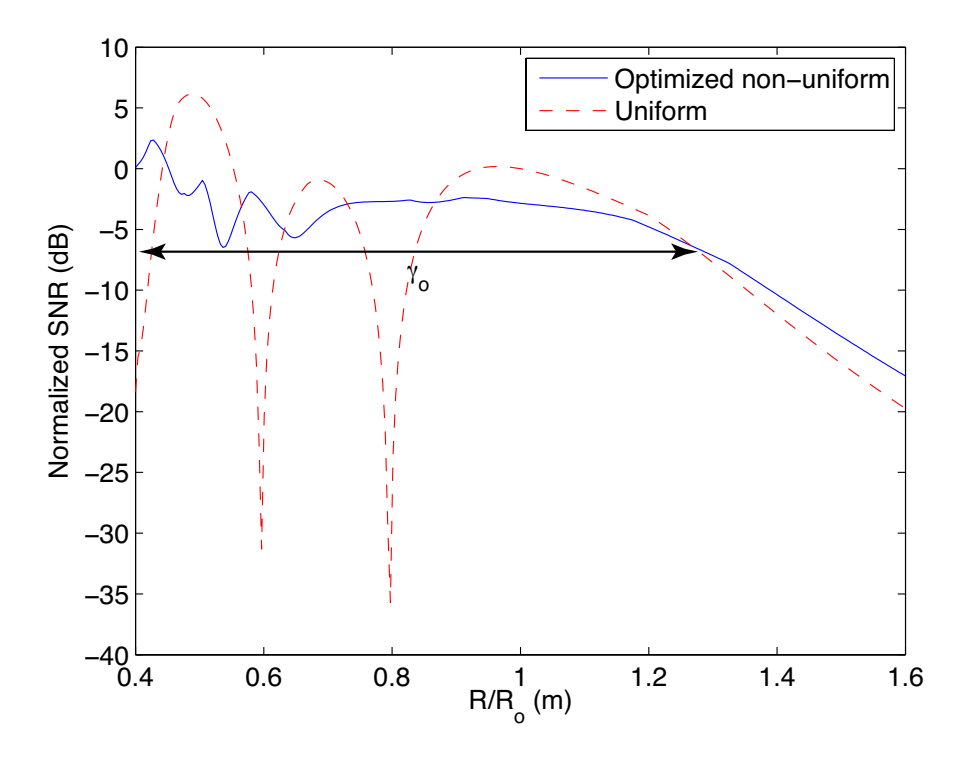


Figure 2.9: Maximum noise enhancement as a function of range for an optimized 5-element array.

Table 2.3: Normalized element positions for optimized nonuniform arrays.

	$x_1$	$x_2$	$x_3$	$x_4$	$x_5$	$x_6$
4 elements	0	0.19	0.81	1		
5 elements	0	0.13	0.54	0.74	1	
6 elements	0	0.10	0.39	0.65	0.83	1

they are well-suited for use with fixed outdoor links that can be aligned during installation.

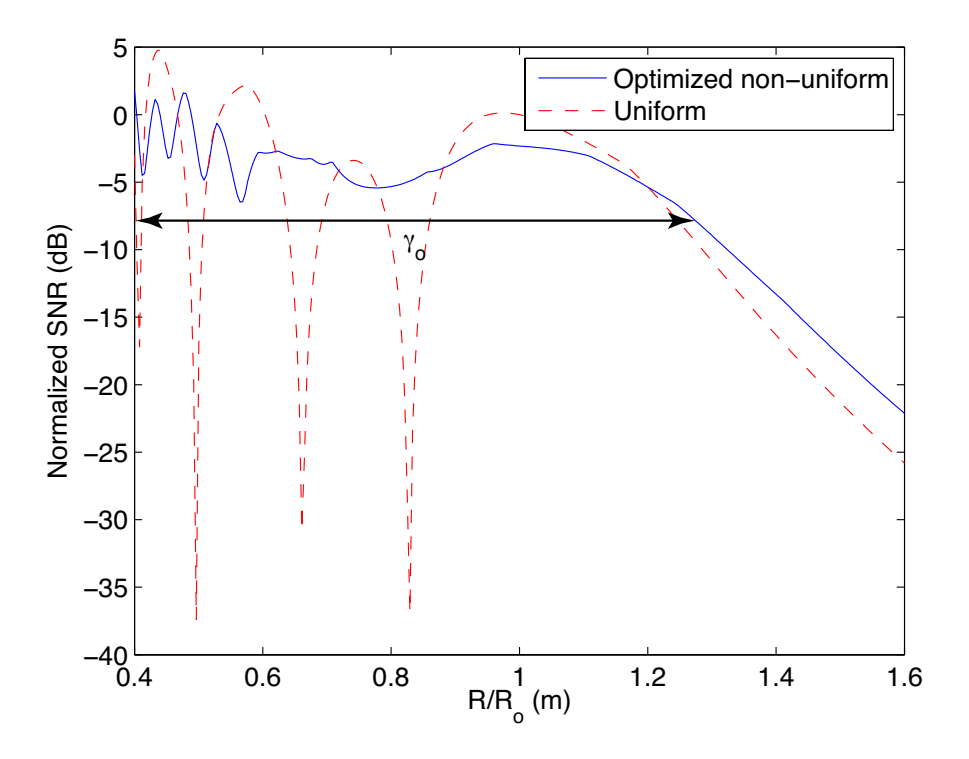


Figure 2.10: Maximum noise enhancement as a function of range for an optimized 6-element array.

## 2.4 Rank Adaptation

In the case that a LOS MIMO channel becomes highly correlated due mismatch between the antenna spacing and the link range, the receiver may be unable to recover the transmitted signal from the interferer(s). In the worst case, the channel matrix becomes rank deficient, and the interfering signals will be irrecoverable. The transmitter can adapt to such a scenario by reducing the number of independent signals it attempts to transmit simultaneously. Specifically, if the receiver responses to two (or more) transmitters are highly correlated, the transmitter

can send a single data stream over these antennas. If there is a strong negative correlation between transmitters, one of the signals should be inverted.

For instance, consider a four element array that satisfies the Rayleigh criterion at some range  $R_o$ . As we saw in Section 2.2, the receiver is unable to distinguish the signals transmitted by the first and fourth antennas at  $R = 0.75R_o$ . In this case, there is a strong positive correlation and the transmitter should send an identical signal from these antennas. At  $R = R_o/2$ , signals 1 and 3 cannot be jointly recovered, nor can signals 2 and 4, and it would be preferable to send two independent signals.

To evaluate the performance of this scheme, we model the  $N \times 1$  received signal vector as

$$y = HQx + n, (2.17)$$

where  $\mathbf{x} \in \mathbb{C}^{N_s \times 1}$  is the transmitted signal vector with entries satisfying  $E(|x_n|^2) = P$ ,  $\mathbf{Q} \in \mathbb{R}^{N \times N_s}$  is a rank adaptation matrix, and  $\mathbf{n} \sim \mathcal{CN}(\mathbf{0}, \mathbf{I}_N)$  is complex additive white Gaussian noise. The entries of Q, selected from  $\{-1, 0, 1\}$ , specify how the  $N_s$  signals are distributed to N transmit antennas. Each row is constrained to have a single non-zero entry to ensure that each antenna transmits a single stream. For instance, if a common signal is sent over the first and fourth antennas

of a four element array, Q is given by

$$Q = \left(\begin{array}{ccc} 1 & 0 & 0 \\ 0 & 1 & 0 \\ 0 & 0 & 1 \\ 1 & 0 & 0 \end{array}\right).$$

We assume the signals are recovered at the receiver using a ZF equalizer with weights  $\mathbf{C} = (\mathbf{H}\mathbf{Q})^{\dagger}$ . The *n*th output of the ZF equalizer is given by

$$y_n = x_n + w_n, \qquad n = 1, 2, \dots, N_s,$$
 (2.18)

where  $w \sim CN(0, \|\mathbf{c}_n\|^2)$  and  $\mathbf{c}_n$  is the *n* row of  $\mathbf{C}$ . The maximum rate at which the system can transmit information reliably is given by

$$\mathcal{I} = \max_{N_s, Q} \sum_{n=1}^{N_s} \log_2(1 + \frac{P}{\|\mathbf{c}_n\|^2}), \tag{2.19}$$

We note that ZF equalization and equal power allocation are suboptimal strategies, but practical design choices for mm-wave systems. We can evaluate how suboptimal the proposed system is by comparing  $\mathcal{I}$  to the channel capacity, the maximum rate of reliable communication over the channel, given by

$$C = \sum_{n=1}^{N} \log_2(1 + P_n \sigma_n^2), \tag{2.20}$$

where  $\frac{1}{N}\sum_{n}P_{n}=P$  is the power allocation under the waterfilling allocation scheme and  $\sigma_{n}^{2}$  is the *n*th eigenvalue of  $\mathbf{H}^{H}\mathbf{H}$  [1].

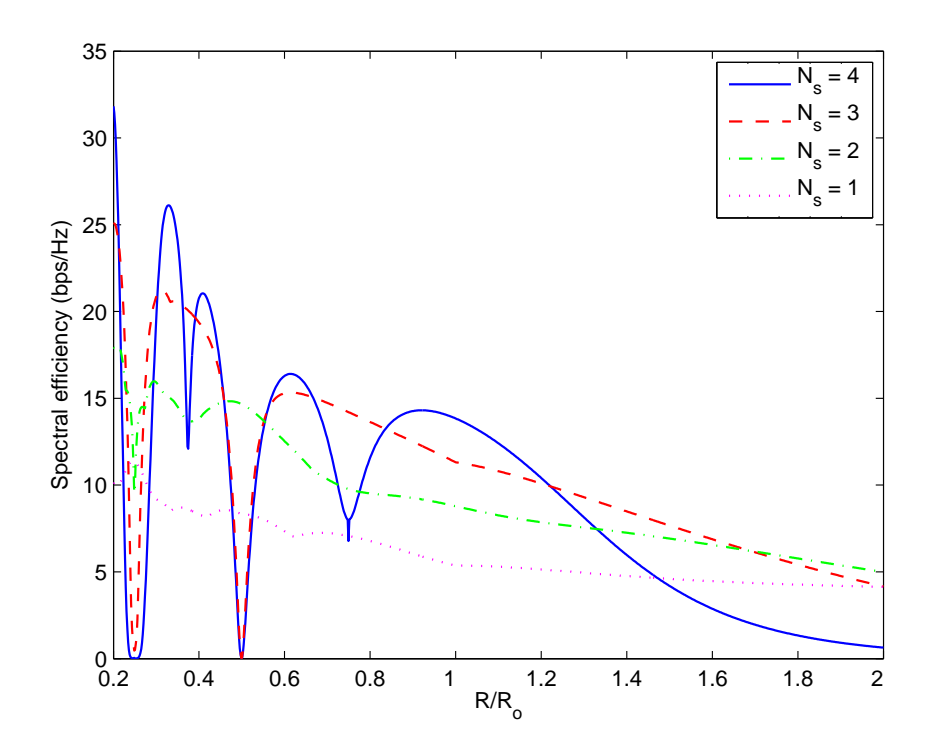


Figure 2.11:  $\mathcal{I}$  as a function of  $N_s$ , the number of independent transmitted signals.

 $\mathcal{I}$  was evaluated through simulation for a LOS MIMO link using 4-element Rayleigh-spaced arrays. Path loss is accounted for by setting the power P at range R equal to

$$P(R) = \left(\frac{R}{R_o}\right)^2 \frac{10}{4},$$

which is normalized such that the equalized signals have a signal-to-noise ratio (SNR) of 10 dB at  $R = R_o$ . Fig. 2.11 plots  $\mathcal{I}$  as a function of normalized link range for fixed values of  $N_s$ . We observe many link ranges where transmitting fewer than four independent data streams is optimal. This is true, as expected,

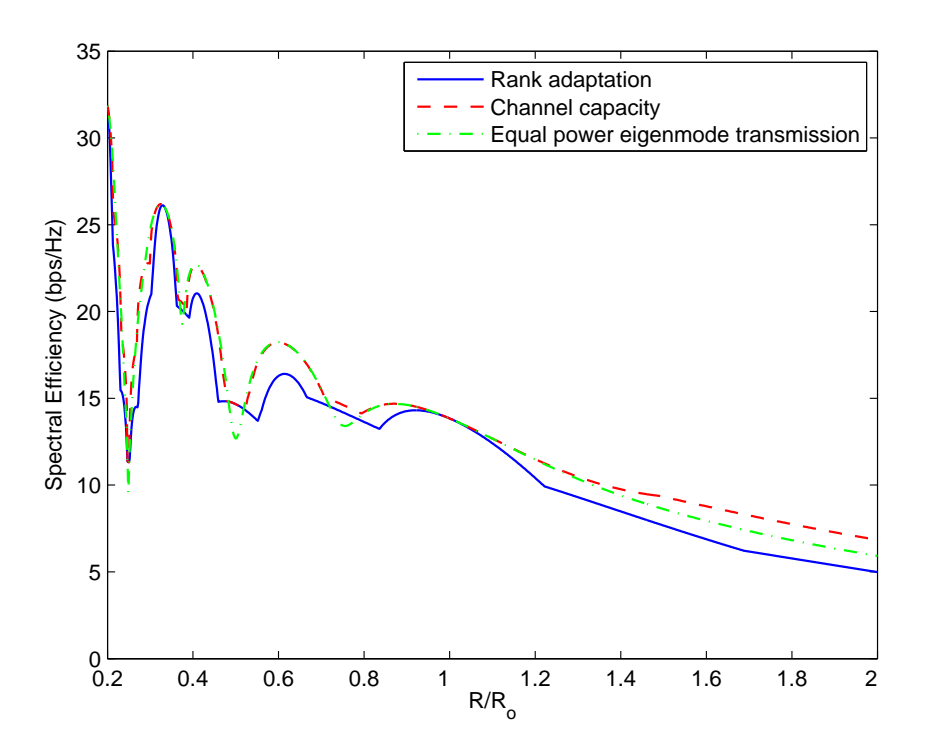


Figure 2.12: Rank adaptation strategy compared to channel capacity.

at the ranges where the correlation rises sharply due to grating lobe interference. It is also holds when the link range is roughly 20% larger than  $R_o$ .

Fig. 2.12 compares  $\mathcal{I}$  to the channel capacity. We also compute (2.20) under equal power allocation, which we refer to as equal power eigenmode transmission. Averaged over  $0.2 \leq R/R_o \leq 2$ , the spectral efficiency of the rate adaptation scheme is 1.37 bps/Hz lower than channel capacity, and 1.03 bps/Hz lower than equal power eigenmode transmission.

## 2.5 Discussion

In this chapter, we presented a case for the use of nonuniform arrays in LOS MIMO systems. In practice, the precise distance between nodes may be unknown during the array design process. Therefore, we examined how system performance is affected when array size and link range are are not matched according to the Rayleigh spacing criterion. Under a zero-forcing equalization scheme, significant degradation of SNR at the output of the equalizer may occur. Seeking to minimize these effects, alternate array geometries were considered. It was demonstrated that non-uniform antenna spacing can provide acceptable performance over a larger set of link ranges than uniform Rayleigh spacing.

We also considered the rank adaptation strategy, in which the number of independent data streams transmitted simultaneously is varied according to the degree of spatial correlation in the channel. Rate adaptation was shown to be an effective strategy when the channel matrix is rank deficient or ill-conditioned.

## Chapter 3

# Hierarchical MIMO Signal Processing: Architecture and Prototype

In the previous chapter, we focused on how the LOS MIMO channel is impacted by antenna array geometry. We now broaden our scope to consider designing a practical mm-wave link that leverages these results. In particular, we consider some of the challenges that arise when a MIMO system scales to larger bandwidths and multi-Gbps symbol rates. High-precision sampling, a critical component of today's DSP-centric designs, becomes prohibitive in cost and power consumption at multiGHz rates. To obviate the need high-speed, high-precision analog-to-digital converters (ADCs), we propose a two-level architecture that decouples the signal processing tasks of spatial equalization and demodulation. More specifically, spatial equalization is applied to the baseband signals in the analog domain, and equalizer training occurs at a slower time-scale, permitting the use of low-rate,

full-precision ADCs. The equalized channels can then each be sampled at a high rate using low-precision ADCs, which are sufficient for demodulation of the small constellation signals currently used for mm-wave communications.

The two-level architecture has been implemented as a four-channel mm-wave MIMO hardware prototype with an aggregate data rate of 2.5 Gbps. To the best of our knowledge, the prototype provided the first demonstration of LOS spatial multiplexing at mm-wave frequencies. It consists of off-shelf mm-wave and RF components and a printed circuit board (PCB) based spatial equalization network. The link was tested at 5 m in an indoor office environment and at 41 m in an outdoor environment.

The mm-wave hardware for the prototype was built by Dr. Colin Sheldon and the adaptive spatial interference suppression scheme was implemented by Dr. Munkyo Seo. The author built the FPGA-based transmitter, and was responsible for Matlab post-processing of complex baseband samples. The prototype was co-supervised by Profs. Mark Rodwell and Upamanyu Madhow.

A detailed description of the prototype hardware can be found in [15] [29] [14] and in Dr. Colin Sheldon's PhD dissertation [30]. The focus here is on describing the system-level architecture and algorithms, including new block-based algorithms for spatial interference suppression that were not implemented on the prototype.

The main contributions of this chapter are as follows:

- We propose a two-level architecture for mm-wave MIMO links that decouples the tasks of equalization and signal demodulation into two separate time scales, thereby avoiding a need for costly high-precision, high-speed ADCs.
- Three spatial equalization methods are introduced. We evaluation their performance through simulation and discuss various tradeoffs associated with their use.
- A four-channel mm-wave MIMO prototype was designed and tested. It provides proof-of-concept for mm-wave LOS spatial multiplexing and the two-level signal processing architecture. We provide a description of the prototype and a summary of experimental results at the end of this chapter.

The chapter is organized as follows. Section 3.1 introduces the two-level mm-wave MIMO architecture and provides the channel model. Spatial equalization and channel estimation is considered in the context of the proposed architecture in Section 3.2. The prototype system is described in Section 3.3 and experimental results are discussed. The chapter concludes with a summary of results in Section 3.4.

## 3.1 Two-level mm-Wave MIMO Architecture

We begin by reviewing traditional training-based channel estimation methods and considering their viability when scaled to multi-Gbps speeds. This motivates the introduction of the proposed architecture in Section 3.1.2.

#### 3.1.1 Pilot-Symbol-Aided Channel Estimation

## Background

A spatial equalizer attempts to eliminate spatial interference by reversing the effects of a MIMO channel. To accomplish this, an equalizer may require an explicit estimate of the channel. Under conventional methods of training-based channel estimation, known pilot symbols are multiplexed with data symbols to facilitate channel estimation at the receiver. This technique is commonly used in existing wireless standards, including GSM, WCDMA, CDMA-2000, and the various 802.11 standards, as well as wireline systems such as cable and DSL [31].

For multiantenna channel estimation, we assume a discrete-time block-fading MIMO channel modeled by

$$Y = HX + W, (3.1)$$

where  $\mathbf{X} \in \mathbb{C}^{N_T \times B}$  represents a a block of symbols transmitted over  $N_T$  transmit antennas and B time slots,  $\mathbf{Y} \in \mathbb{C}^{N_R \times B}$  is the signal received over  $N_R$  receive

antennas,  $\mathbf{W} \in \mathbb{C}^{N_R \times B}$  is additive noise, and  $\mathbf{H} \in \mathbb{C}^{N_R \times N_T}$  is the channel. The transmitted signal, including pilot symbols, is given by

$$x_{k,n} = \sqrt{\alpha_{k,n}} d_{k,n} + \sqrt{\beta_{k,n}} p_{k,n}, \qquad k = 1, \dots, N_T, \qquad n = 1, \dots, B,$$
 (3.2)

where  $x_{k,n}$  is the signal transmitted from the kth antenna at time slot n,  $d_{k,n}$  is an unknown data symbol with zero mean and unit variance, and  $p_{k,n}$  is a training symbol with  $|p_{k,n}| = 1$ . The power allocated to data and training symbols are given by  $\alpha_{k,n}$  and  $\beta_{k,n}$ , respectively. The form of 3.2 permits training signals to be interspersed, clustered together, or embedded with data signals.

Equation (3.1) is a linear channel model and permits straightforward application of the linear least squares (LSE) or linear minimum mean squared error (MMSE) estimators to acquire a channel estimate [32]. The channel estimate, in turn, can be used to recover the transmitted signals from interference using, for example, the ZF filter.

Modern digital communication receivers commonly sample signals with 6-12 bits of precision, which is sufficient for the pilot-symbol-aided channel estimation techniques just described to approach full-precision performance. MultiGbps links operating in the 60 GHz band, however, require sampling rates on the order of several GHz. As bandwidth and data rates scale up, the cost, power consumption, and availability of high-speed, high-precision ADCs becomes prohibitive [5]. As

a result, the ADC becomes a limiting factor in designing affordable multiGbps mm-wave MIMO architectures.

This bottleneck could potentially be avoided by using significantly lower precision ADCs (i.e. 1-3 bits) than are currently employed. Application of the linear LSE or MMSE estimator to this highly-quantized data would produce a poor channel estimate. However, information theoretic studies of SISO links have demonstrated that the capacity loss resulting from the use of low-precision ADCs is relatively small, assuming a non-dispersive channel with perfect synchronization [33]. Methods of performing various receiver tasks using highly quantized data have been considered in the literature, including amplitude estimation [34], frequency estimation [35], direction of arrival estimation using coarse quantization was recently addressed in [38], although the proposed estimator requires operation in the low-SNR regime and provides relatively coarse estimates when using 1- or 2-bit quantizers. We propose an alternate approach to channel estimation in the following section.

## 3.1.2 System Architecture

In this section, we consider the alternate approach of a two-level architecture that performs spatial equalizer adaptation and channel demodulation on separate

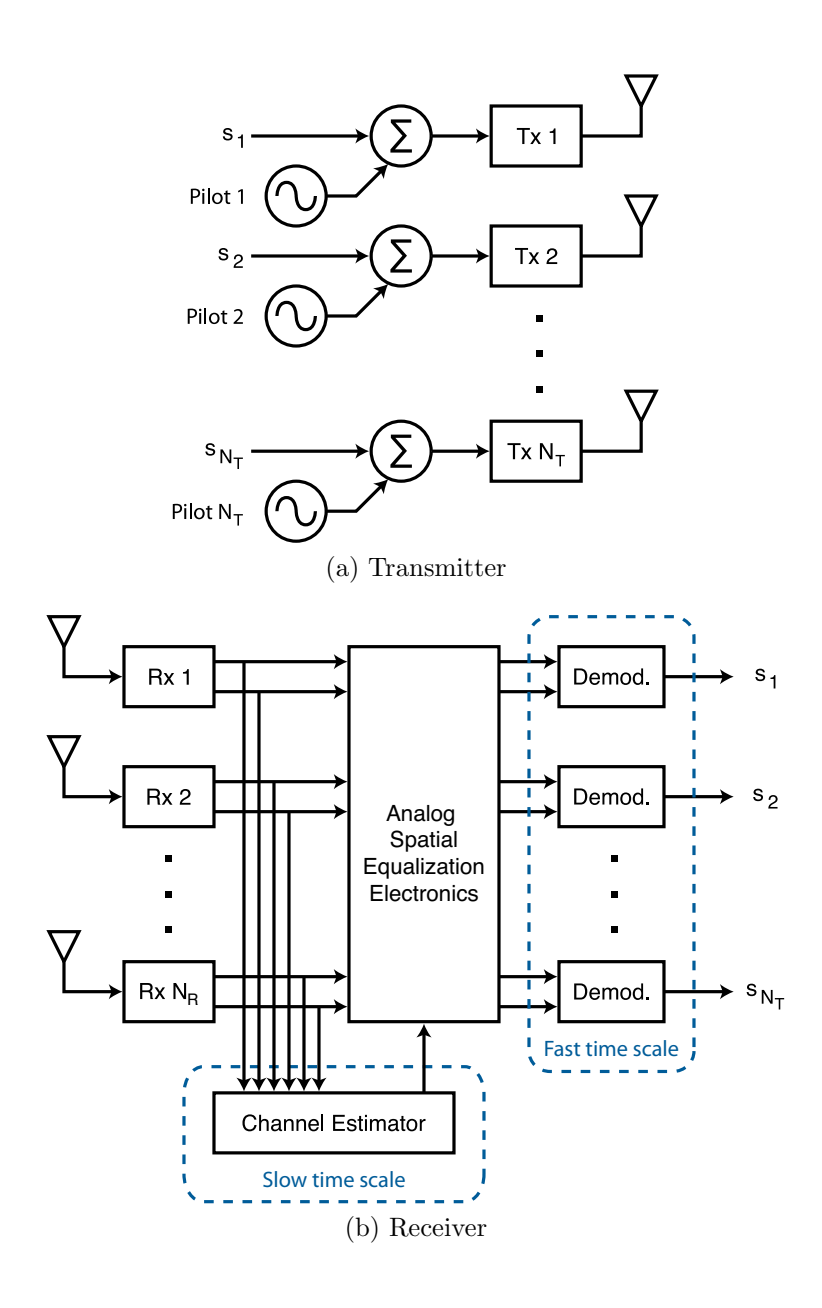


Figure 3.1: Two-level system architecture.

time scales. The architecture derives from the realization that, for the reasons described above, channel estimation benefits from full-precision sampling, while low-precision sampling suffices for other tasks, such as the demodulation of small-constellation signals. Fig. 3.1 is a block diagram of the proposed system. The transmitter combines each of  $N_T$  baseband data streams with a unique narrowband pilot signal, which we take to be a low-frequency (i.e. 10-100 kHz range) sinusoid. The signals are upconverted to 60 GHz and transmitted over an array of  $N_T$  elements. The signals are received over an  $N_R$  element array and downconverted to complex baseband. The baseband signals are spatially equalized in the analog domain before the recovered signals are sampled with high-rate, low-precision ADCs and demodulated.

The spatial equalizer coefficients are determined through an explicit or implicit channel estimate which is derived through processing of the embedded pilot signals. The pilot signals have significantly lower bandwidth than the data, which may span several GHz. The received signals can therefore be filtered and sampled at a high precision using inexpensive low rate ADCs. Fig. 3.1 depicts an open-loop architecture, where an explicit estimate of the channel is formed from observations of the pilot tones. This estimate is in turn used to compute the equalizer coefficients. A feedback-based architecture is also considered, where the equalizer controller observes the pilot tones to estimate the symbol-to-interference

ratio (SIR) at the equalizer output. The controller adjusts the equalizer weights adaptively to maximize the measured SIR. In this case, an explicit channel estimate is not formed. Both designs are considered in more detail in 3.2.

#### 3.1.3 Channel Model

The continuous-time complex baseband signal received at the mth receive antenna is given by

$$r_m(t) = e^{i(2\pi f_0 t + \phi_0)} \sum_{n=1}^{N_T} h_{m,n} \left( p_n(t) + d_n(t) \right) + w_m(t), \tag{3.3}$$

where  $h_{m,n}$  is the complex channel gain between the mth receive antenna and nth transmit antenna,  $p_n(t)$  and  $d_n(t)$  are the nth pilot signal and data signal, respectively,  $w_m(t)$  is complex white Gaussian noise with power spectral density  $N_0$ , and  $f_0$  and  $\phi_0$  are a carrier frequency offset and phase offset, respectively, which allow for mismatch between the carrier signals at the transmitter and receiver. We assume  $|f_0| < f_M$ , where  $f_M$  denotes the maximum possible carrier frequency offset.

The nth data signal is given by

$$d_n(t) = \sqrt{\frac{1}{N_T}} \sum_{l=-\infty}^{\infty} s_{n,l} g(t - lT_d - \tau), \qquad n = 1, \dots, N_T,$$
 (3.4)

where  $T_d$  is the symbol rate, g(t) is a pulse shape satisfying  $||g(t)||^2 = T_d$ ,  $\tau$  is an unknown time delay, and the complex data symbols  $\{s_{n,l}\}$  satisfy  $E[s_{n,l}s_{m,k}^*] =$ 

 $E_s\delta_{nm}\delta_{lk}$ . This signal is summed at the transmitter with the *n*th pilot signal, given by

$$p_n(t) = \sqrt{\frac{\alpha}{N_T}} \exp\left(i \left(2\pi f_n t + \phi_n\right)\right), \qquad (3.5)$$

where  $\alpha$  is a scaling factor,  $f_n$  is a given frequency, and  $\phi_n$  is an unknown phase offset. We assume  $|h_{m,n}|^2 = 1$ , and hence  $\alpha$  is the received power of each pilot tone.

The spatial interference cancellation algorithms described herein operate on the received signal after it has been low-pass filtered and sampled. We take the filter to be ideal low-pass with one-sided bandwidth B/2, where  $B \ll 1/T_d$ . The sampling rate, denoted by  $F_s > 2(f_M + \max_n f_n)$ , is chosen independently of the data, which is treated as noise by the interference cancellation algorithm. The filtering and sampling operations produce the discrete-time signal

$$r_m[k] = LPF\{r_m(kT_s)\}$$
(3.6)

$$= e^{i(2\pi f_0 k T_s + \phi_0)} \sum_{n=1}^{N_T} h_{m,n} \left( \sqrt{\frac{\alpha}{N_T}} p_n(k T_s) + \sqrt{\frac{1}{N_T}} \tilde{d}_n(k T_s) \right) + w_m[k], \quad (3.7)$$

where  $T_s = 1/F_s$ ,  $\tilde{d}_n(t)$  is a low-pass filtered version of  $d_n(t)$ , and  $w_m[k]$  is zero mean, complex Gaussian noise with variance  $2\sigma_N^2 = N_0 B$ . In the frequency range -B/2 < f < B/2, we assume the PSD of the data signal is roughly flat and equal to  $T_d$ , which is satisfied, for instance, by the pulse  $g(t) = \text{sinc}(t/T_d)$ . The nth

filtered data stream is represented in discrete time as

$$\tilde{d}_n[k] = BT_d \sum_{l=-\infty}^{\infty} s_{n,l} \operatorname{sinc} \left( B \left( kT_s - lT_d - \tau \right) \right). \tag{3.8}$$

Noting that  $BT_d \ll 1$ , we observe that  $\tilde{d}_n[k]$  is the sum of a large number of independent random variables, and can be approximated as a zero mean Gaussian random variable with variance  $2\sigma_d^2 = E[|\tilde{d}_n[k]|^2] = BT_dE_s$ . We assume that the sampling rate  $F_s$  equals an integer multiple of B and the data and noise terms of the sampled received signal are uncorrelated, and hence independent, in time.

The low-pass filtered, discrete-time received signal can be expressed in vector notation as

$$\mathbf{r}[k] = e^{i(2\pi f_0 k T_s + \phi_0)} \mathbf{H} \left( \sqrt{\frac{\alpha}{N_T}} \mathbf{p}[k] + \sqrt{\frac{1}{N_T}} \tilde{\mathbf{d}}[k] \right) + \mathbf{w}[k]$$
 (3.9)

where  $\mathbf{H} \in \mathbb{C}^{N_R \times N_T}$  is the channel matrix whose (m, n)th entry is  $h_{m,n}$ ,  $\mathbf{p}[k] \in \mathbb{C}^{N_T \times 1}$  is the sampled pilot tone vector whose nth entry is  $p_n(kT_s)$ ,  $\tilde{\mathbf{d}}[k] \sim \mathcal{CN}(\mathbf{0}, 2\sigma_d^2 \mathbf{I}_{N_T})$  represents filtered data, and  $\mathbf{w}[k] \sim \mathcal{CN}(\mathbf{0}, 2\sigma_N^2 \mathbf{I}_{N_R})$  is complex white Gaussian noise.

## 3.2 Spatial Interference Suppression

The spatial equalizer is implemented as a linear filter in the analog domain using array of variable-gain amplifiers (VGAs) as shown in Fig. 3.2.  $N_R$  complex-valued

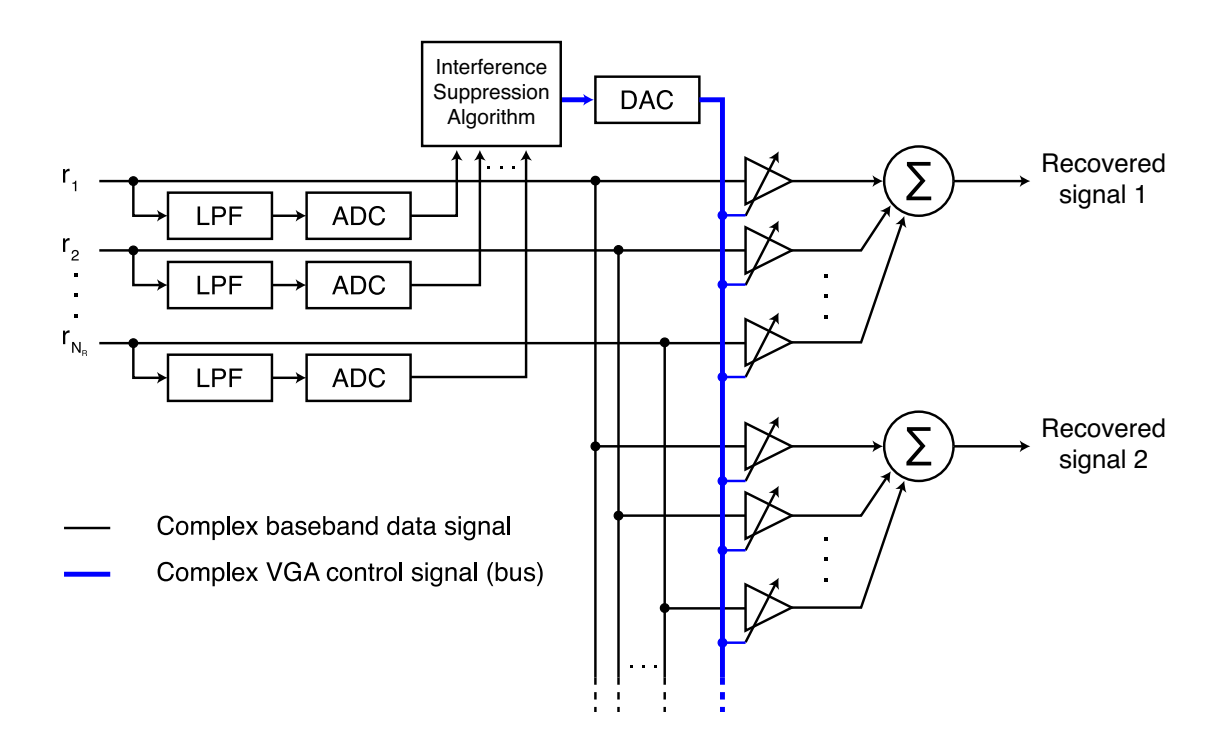


Figure 3.2: Open-loop spatial equalizer structure.

gains are required to recover each of the  $N_T$  transmitted signals, requiring  $N_R N_T$  complex gains in total. They are implemented using  $2N_R N_T$  VGAs. The equalizer weights, represented by the matrix  $\mathbf{C} \in \mathbb{C}^{N_T \times N_R}$  are chosen such that  $\mathbf{C}\mathbf{H} = \mathbf{I}_{N_T}$ . This approach is commonly referred to as the decorrelating receiver or zero-forcing (ZF) spatial equalizer, and is achieved by setting  $\mathbf{C}$  equal to the pseudoinverse of  $\mathbf{H}$ , given by  $\hat{\mathbf{H}} = (\mathbf{H}^H \mathbf{H})^{-1} \mathbf{H}^H$ .

Given the channel model in (3.9), there are  $N_T + 2$  unknown parameters in addition to the entries of **H**. Namely, these are the carrier frequency offset and phase offset, and the  $N_T$  pilot signal phases. The carrier frequency offset must be

estimated, either implicitly or explicitly, to obtain an estimate of **H**. However, we now show that the unknown carrier and pilot phases can be ignored during the estimation process if we allow the recovered signals at the output of the spatial equalizer to have arbitrary phase. Specifically, we allow  $\mathbf{C}\mathbf{H} = \boldsymbol{\phi}^H \mathbf{I}_{N_T}$ , where  $|\phi(n)|^2 = 1$  for  $n = 1, 2, ..., N_T$ .

We define the *n*th entry of  $\mathbf{p}_0[k]$  as  $p_n[k] = \exp(i2\pi f_n)$ , i.e. the *n*th sampled pilot tone assuming  $\phi_n = 0$ . We also define

$$\Phi_D = \text{diag}([e^{i(phi_1+phi_0)}, e^{i(phi_2+phi_0)}, \dots e^{i(phi_{N_T}+phi_0)}]).$$

We then have the equality

$$e^{i(2\pi f_0 k T_s + \phi_0)} \mathbf{H} \mathbf{p}[k] = e^{i(2\pi f_0 k T_s)} \mathbf{H}_0 \mathbf{p}_0[k],$$

where  $\mathbf{H}_0 = \mathbf{H}\mathbf{\Phi}_D^H$ . If we assume  $\phi_n = 0$  for  $n = 0, 1, ..., N_T$  during estimation, our channel estimator will produce an estimate  $\hat{\mathbf{H}}$  of  $\mathbf{H}_0$  rather than of  $\mathbf{H}$ . When  $\hat{\mathbf{H}} = \mathbf{H}_0$ , the estimate satisfies

$$\hat{\mathbf{H}}^{\dagger}\mathbf{H} = (\mathbf{\Phi}_D \mathbf{H}^H \mathbf{H} \mathbf{\Phi}_D^H)^{-1} (\mathbf{H} \mathbf{\Phi}_D)^H \mathbf{H}$$
 (3.10)

$$= \mathbf{\Phi}_D^{-1} (\mathbf{H}^H \mathbf{H})^{-1} \mathbf{\Phi}_D^{-H} \mathbf{\Phi}_D^H \mathbf{H}^H \mathbf{H}$$
 (3.11)

$$= \mathbf{\Phi}_D^{-1}, \tag{3.12}$$

and is thus valid for the purpose of ZF equalization. We can henceforth assume the carrier and pilot phases to be zero. We consider three spatial equalization schemes. The first two schemes compute estimates of the channel matrix in different ways, and use these estimates to perform ZF equalization. The third is a closed-loop iterative approach that adapts the equalizer weights based on observations of the equalized signal.

#### 3.2.1 DFT-Based Channel Estimation:

The samples of the kth received signal stream in (3.6) can be rewritten

$$r_m[k] = \sqrt{\frac{\alpha}{N_T}} \sum_{n=1}^{N_T} h_{m,n} \exp(-i2\pi (f_n - f_0)kT_s) + z[k],$$
 (3.13)

where z[k] is a composite noise combining the data and additive noise terms. The channel estimation problem is equivalent to finding the frequencies and complex amplitudes of  $N_T$  tones from a set of noisy discrete-time samples. This problem of estimating the amplitude and frequency of a single tone from discrete-time observations was addressed in [39]. There, the authors showed that the ML estimates of these parameters were related to the discrete-time Fourier transform (DTFT) of the sampled signal, given by

$$A(f) = \frac{1}{L} \sum_{n=0}^{L-1} s[k] \exp(-i2\pi f l T_s),$$

where L is the number of observations and  $s[l] = a \exp(i2\pi f_e l T_s)$  are the noisy samples of a complex sinusoid. Specifically, the ML estimate of  $f_e$  is given by

$$\hat{f}_e = \underset{f,a}{\arg\max} |A(f)|,$$

and the ML estimate of a is

$$\hat{a} = A(\hat{f}_e).$$

Thus the problem requires finding the value of the DTFT where its magnitude reaches is maximum value. The ML solution can be approximated by performing these operations over the DFT rather than the DTFT. Alternatively, if an explicit estimate of the noise variance is found, the channel estimate could be used to implement MMSE equalization. For the relatively high SNR and well-conditioned channel matrices in our application, the MMSE and ZF solutions give similar performance.

The generalization to estimating the amplitudes of  $N_T$  tones is straightforward if we assume the pilot tones are separated in frequency by at least  $2f_M$ , where  $|f_0| < f_M$ . The process is as follows:

- 1. Given L discrete-time observations of the mth received signal, compute  $R_m[l]$ , the N-point DFT.
- 2. For n in 1 to  $N_T$ , search for the maximum of  $|A_m[l]|$  over the frequency bins corresponding to the window  $f_n f_M \le f \le f_n + f_M$ . Denote the bin where this occurs by  $n_{m,n}^*$ . Then  $\hat{h}_{m,n} = A_m[n_{m,n}^*]$ .

The individual estimates  $\hat{h}_{m,n}$  form the entries of  $\hat{\mathbf{H}}$ . The channel estimate can be used to perform ZF equalization, with the equalizer weights given by  $\mathbf{C} = \mathbf{H}^{\dagger}$ .

## 3.2.2 Least Squares Channel Estimation:

We next consider choosing the equalizer weights based on the least-squares estimate (LSE) of **H**. We begin by reviewing the LS estimate of a MIMO channel matrix given a linear channel model. The linear MIMO channel is given by

$$\mathbf{Y} = \mathbf{H}\mathbf{X} + \mathbf{V},\tag{3.14}$$

where  $\mathbf{Y} \in \mathbb{C}^{N_R \times L}$  represents the received signal vector collected over L time instants,  $\mathbf{X} \in N_T \times L$  is a block of known training data that has been transmitted, and  $\mathbf{V} \in N_R \times L$  is the measurement error, in our case taken to be additive Gaussian noise. We assume  $L > N_T$  so that we have more measurements than the  $N_T N_R$  unknown variables in  $\mathbf{H}$ . The LS estimate of  $\mathbf{H}$  given this channel model is given by

$$\hat{\mathbf{H}} = \mathbf{Y}\mathbf{X}^{\dagger},\tag{3.15}$$

where  $\mathbf{X}^{\dagger} = \mathbf{X}^{H}(\mathbf{X}\mathbf{X}^{H})^{-1}$  is the Moore Penrose pseudo-inverse.

We now consider the least squares in the context of the proposed architecture. The equalizer operates on a block of the past L consecutive samples of the low-pass filtered discrete-time received signal vector  $\tilde{\mathbf{r}}$ , as given by  $\mathbf{R}[k] = [\tilde{\mathbf{r}}[k-L+1], \mathbf{r}[k-L+2], \dots, \mathbf{r}[k]]$ .  $\mathbf{R}[k]$  can expressed in terms of its constituent signals as

$$\mathbf{R}[k] = (\mathbf{1}_{N_R \times 1} \mathbf{f}[k]) \circ \left( \mathbf{H} \left( \sqrt{\frac{\alpha}{N_T}} \mathbf{P}[k] + \sqrt{\frac{1}{N_T}} \tilde{\mathbf{D}}[k] \right) \right) + \mathbf{W}[k]$$
 (3.16)

where  $\mathbf{1}_{N_R \times 1}$  is the  $N_R \times 1$  all-ones vector, and the *n*th entry of  $\mathbf{f}[k] \in \mathbb{C}^{1 \times L}$  is  $e^{i2\pi f_0(k-L+n)T_s}$ , and  $\mathbf{W}[k] \in \mathbb{C}^{N_R \times L}$  is additive white Gaussian noise with independent identically distributed (i.i.d.) entries in  $\mathcal{CN}(0, 2\sigma_N^2)$ . Eq. (3.16) can be alternatively be expressed as

$$\mathbf{R}[k] = \mathbf{HP}'[k] + \mathbf{Z}[k], \tag{3.17}$$

where the filtered data and noise terms have been combined into a single noise term  $\mathbf{Z}[k]$ , and

$$\mathbf{P}'[k] = \sqrt{\frac{\alpha}{N_T}} \mathbf{P}[k] \circ (\mathbf{1}_{N_T \times 1} \mathbf{f}[k]). \tag{3.18}$$

The columns of  $\mathbf{Z}[k]$  are zero mean with covariance  $\frac{2\sigma_d^2}{N_T}\mathbf{H}^H\mathbf{H} + 2\sigma_N^2\mathbf{I}_{N_R}$ .

Our channel model (3.17) differs from the linear model (3.14) in that the training data vector  $\mathbf{P}'[k]$  is subject to an unknown carrier frequency offset. Since the frequency is a non-linear parameter in the channel model, it must be estimated prior to taking the linear LS estimate of  $\mathbf{H}$ . We note that the carrier frequency offset has the effect of shifting the pilot tones in frequency by  $f_0$ . Since the pilot tone frequencies  $f_n$  are known, estimating  $f_0$  amounts to estimating the frequencies of the shifted pilot tones. The (approximate) frequencies of the pilot tones are easily observed by locating the impulses in the discrete Fourier transform (DFT) of the received signal. As described in Section 3.2.1, the DFT peak detection method approximates the ML estimate. An N-point FFT gives a frequency resolution of

 $F_s/(2N)$ , which may be the limiting factor in our estimate of  $f_0$ . If sufficient FFT resolution is unavailable, numerical methods may be used instead to maximize the DTFT of the received signal [39].

Using  $\hat{f}_0$ , our estimate of  $f_0$ , we can form an estimate  $\hat{\mathbf{P}}'[k]$  of the frequency-shifted pilot tones as specified in (3.18). It follows that the LS estimate of  $\mathbf{H}$  is given by

$$\hat{\mathbf{H}} = \mathbf{R}[k]\hat{\mathbf{P}}'[k]^{\dagger}. \tag{3.19}$$

The channel estimate can then be used to find ZF or MMSE equalizer weights.

As described, the channel estimate is formed from simultaneous processing of  $N_R \times L$  measurements. An alternative to block-based least squares estimation is to employ the recursive least squares (RLS) [40].

## 3.2.3 Closed-Loop Equalization:

The last method we consider uses the closed-loop equalizer structure shown in Fig. 3.3 to recover a desired signal. In this approach, the interference cancellation algorithm observes the equalizer output in the frequency domain using the fast Fourier transform (FFT). The pilot tones embedded in the received signal appear as impulses in the frequency domain, as shown in Fig. 3.4a. The *n*th impulse lies within the frequency window  $f_n - f_M \leq f \leq f_n + f_M$ , where  $f_M$  accounts for possible frequency translation due to carrier frequency offset. By comparing

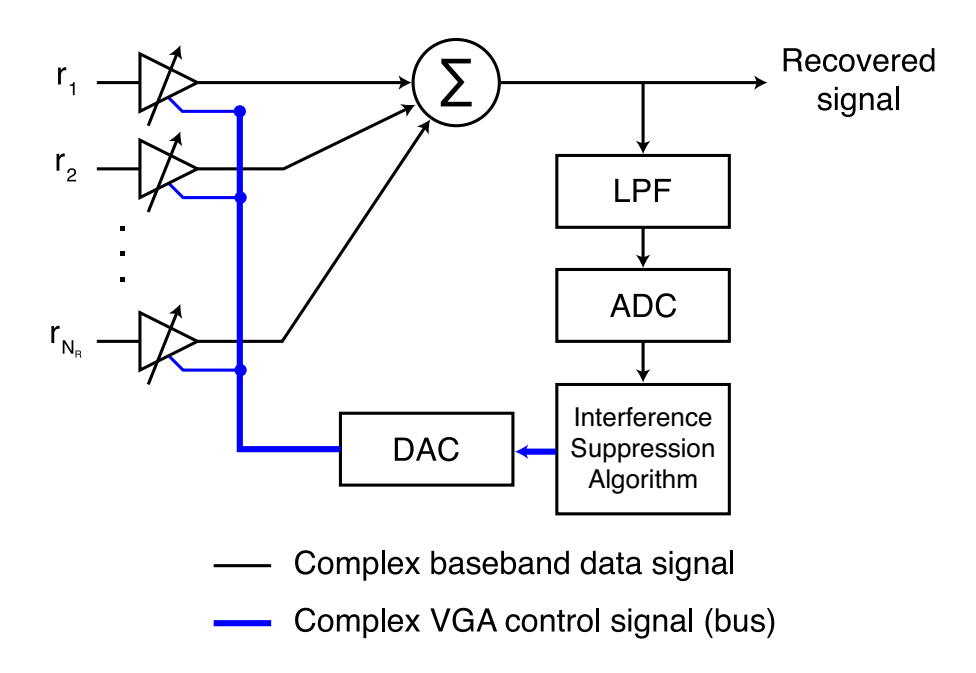


Figure 3.3: Closed-loop frequency domain spatial equalizer structure.

the relative magnitudes of these impulses, the signal-to-interference ratio (SIR) can be estimated. The interference cancellation algorithm iteratively adjusts the equalizer weights, reevaluating the SIR after each adjustment. In this manner, the weights converge to a solution with high SIR as shown in Fig. 3.4a, where the interference caused by the 2nd, 3rd, and 4th transmitted signals has been eliminated. Note that the equalizer in Fig. 3.3 recovers one of the  $N_T$  transmitted signals, and thus a receiver must include  $N_T$  such structures to recover all transmitted signals.

As an example, we consider the iterative weight adjustment scheme that was used in the hardware prototype discussed in Section 3.3. Consider the task of

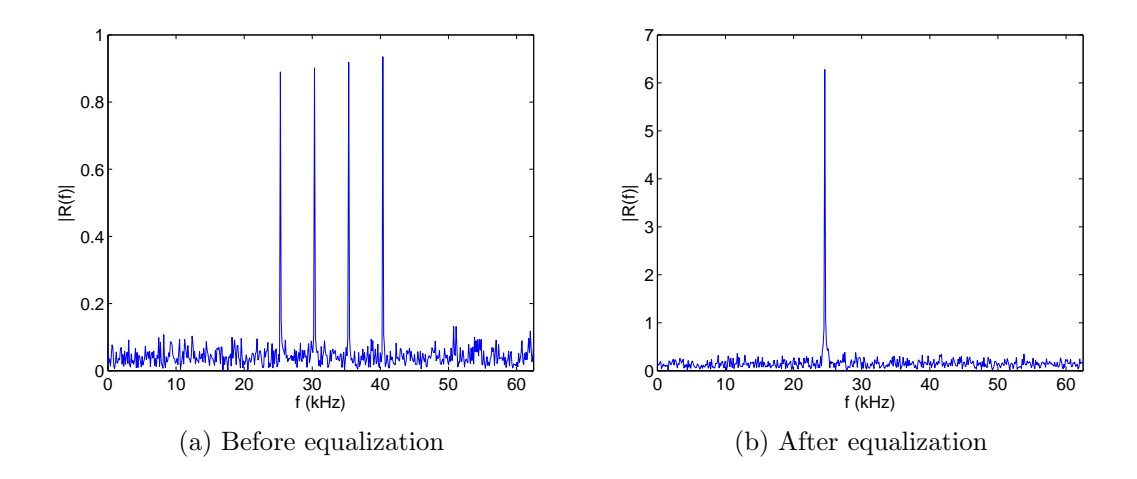


Figure 3.4: Discrete Fourier transform of received signal.

recovering the kth transmitted signal, with the corresponding equalizer weights specified by the kth row of  $\mathbf{C}$ , denoted by  $\mathbf{c}_k$ . We begin by describing the process used to estimate the SIR of the desired pilot signal. When required to estimate the SIR at some discrete time n, the interference cancellation algorithm forms  $\mathbf{y}$  from the following N consecutive samples of the equalized low-pass signal, given by

$$\mathbf{y} = \mathbf{c}_k \mathbf{R} \tag{3.20}$$

where  $\mathbf{R} = [\mathbf{r} [n] \mathbf{r} [n+1] \dots \mathbf{r} [n+N-1]]$ , and we assume  $\mathbf{c}_k$  remains constant over the observation window. The FFT is then performed on  $\mathbf{y}$  to estimate the SIR by observing the relative powers of the pilot signals in the frequency domain. This is achieved by recording the peak value, denoted by  $P_j$ , of the squared magnitude of the FFT in the frequency range  $f_j - f_M \leq f \leq f_j + f_M$  for  $j = 1, 2, \dots, N_T$ . The normalized peak power, defined as

$$NPP = \frac{P_k}{\sum_{j=1}^{N_T} P_j},$$
(3.21)

is then computed. We note  $NPP \in [0,1]$ , with values closer to one indicating a higher SIR.

#### Algorithm 1 Adaptive Control Loop

```
for n = 1 to 2N_R do {Initialize variables}
   a(n) \leftarrow 0
   \delta(n) \leftarrow \epsilon_1
   F(n) \leftarrow 0
end for
NPP_{stored} \leftarrow 0
loop
   for n = 1 to 2N_R do
     a(n) \leftarrow a(n) + \delta(n)
      calculate NPP
     if NPP < NPP_{stored} then {Revert to previous VGA gain}
         a(n) \leftarrow a(n) - \delta(n)
        if F(n) = 0 then {Reverse search direction}
           \delta(n) \leftarrow -\delta(n)
            F(n) \leftarrow 1
        else {Reduce perturbation}
           \delta(n) \leftarrow \delta(n)(1-\epsilon_2)
            F(n) \leftarrow 0
         end if
      else
         NPP_{stored} \leftarrow NPP
      end if
   end for
end loop
```

Whenever the equalizer weights are adjusted, the interference cancellation algorithm computes a new value of NPP to determine whether the change had a

positive or negative impact on the SIR. The equalizer weights are implemented as VGA gains applied to the in-phase and quadrature components of the complex baseband received signal. Letting  $\mathbf{a} \in \mathbb{R}^{2N_R \times 1}$  represent the VGA gains, we set the mapping between the complex weight vector and and the real VGA gains as  $a(2n-1) = \Re(c_k(n))$  and  $a(2n) = \Im(c_k(n))$  for  $n=1,2,\ldots,N_R$ . The iterative process of adjusting the VGA gains is described in Algorithm 1, where the input parameters  $\epsilon_1$  and  $\epsilon_2$  are chosen as small values less than one. With each iteration, the algorithm adjusts the VGA gains consecutively in the directions that increase the NPP. If gain adjustments in both the positive and negative directions reduce the NPP, a smaller adjustment is applied to that VGA in the following iteration.

Note that, while not explicitly stated in Algorithm 1, the weights may be normalized periodically to ensure they remain within the bounds imposed by the VGA hardware.

Note that this approach makes no explicit computation of the optimal equalizer weights, and relies instead on evaluating the effect of small perturbations to the VGA weights. As such, the algorithm does not need accurate knowledge of the mapping between the control signal applied to the VGA and the corresponding gain applied to the received signal. Also note that the interfering pilot tones will be reduced in power until they reach the noise level. At this point, the peak detect algorithm used to calculate NPP will be unable to distinguish the pilot

tones from the noise. This prevents the pilot tones interference from being nulled further at the price of noise enhancement. Hence, this method may converge to the linear MMSE solution which minimizes the signal-to-interference-and-noise ratio (SINR), rather than the ZF solution which minimizes the SIR. Under low SNR conditions, the linear MMSE equalizer outperforms the ZF equalizer. However, in the scenario under consideration, where the pilot tones are likely high above the noise floor, the two solutions will essentially coincide.

The example weight adjustment scheme was described in detail because it was used in the mm-wave MIMO hardware prototype. It should be possible to obtain improved adaptive algorithms, however, that provably converge to the linear MMSE equalizer, (e.g., using coarse frequency estimation followed by differential MMSE), while maintaining the advantage of not requiring precise calibration of the VGA weights.

#### 3.2.4 Simulation Results

The performance of the proposed spatial equalizer adaptation schemes is evaluated through simulation. We consider a point-to-point MIMO link with four antennas at each node. We assume the LOS channel model described in 2.1.1. It is also assumed that the antenna arrays are Rayleigh spaced, and hence  $\mathbf{H}\mathbf{H}^H = N_T \mathbf{I}_{N_R}$ . As such, the entries of  $\mathbf{Z}$  in (3.17) are i.i.d. zero-mean complex Gaussian random

variables with variance  $2\sigma_Z^2=2(\sigma_d^2+\sigma_N^2)$ . We define the pilot-to-noise ratio as  $\text{PNR}=\alpha/\sigma_Z^2$ .

The pilot tones have frequencies 25 kHz, 30 kHz, 35 kHz, and 40 kHz. The carrier frequency offset is a uniformly distributed random variable taking values in the range -1 kHz  $< f_0 < 1$  kHz, while the carrier and pilot phases are uniformly distributed in  $[0, 2\pi]$ . The sample rate is  $F_s = 125$  kHz.

The performance of each equalizer is evaluated in terms of the signal-tointerference ratio (SIR) at its output. With  $\mathbf{c}_k$  representing the kth row of  $\mathbf{C}$ , we define  $\mathbf{s} = \mathbf{c}_k \mathbf{H}$ . The SIR of the kth recovered signal is then given by

$$SIR_k = \frac{s[k]^2}{\sum_{n \neq k} s[n]^2}, \qquad k = 1, \dots, N_T.$$
 (3.22)

We first consider the performance of the DFT-based spatial equalizer. The SIR is plotted in Fig. 3.5 as a function of the DFT length, taken by factors of two for efficient FFT implementation. We observe that the SIR increases linearly with the DFT length.

Next, we assess the performance of the LSE-based spatial equalizer. We assume the carrier frequency offset has initially been estimated to within 1 Hz. Fig. 3.6 plots the SIR as a function of the (unweighted) LS observation window. A larger observation improves the channel estimate essentially through filtering the measurement noise. However, this improvement is offset by the effect of error in the carrier frequency offset estimate. This effect increases observation window

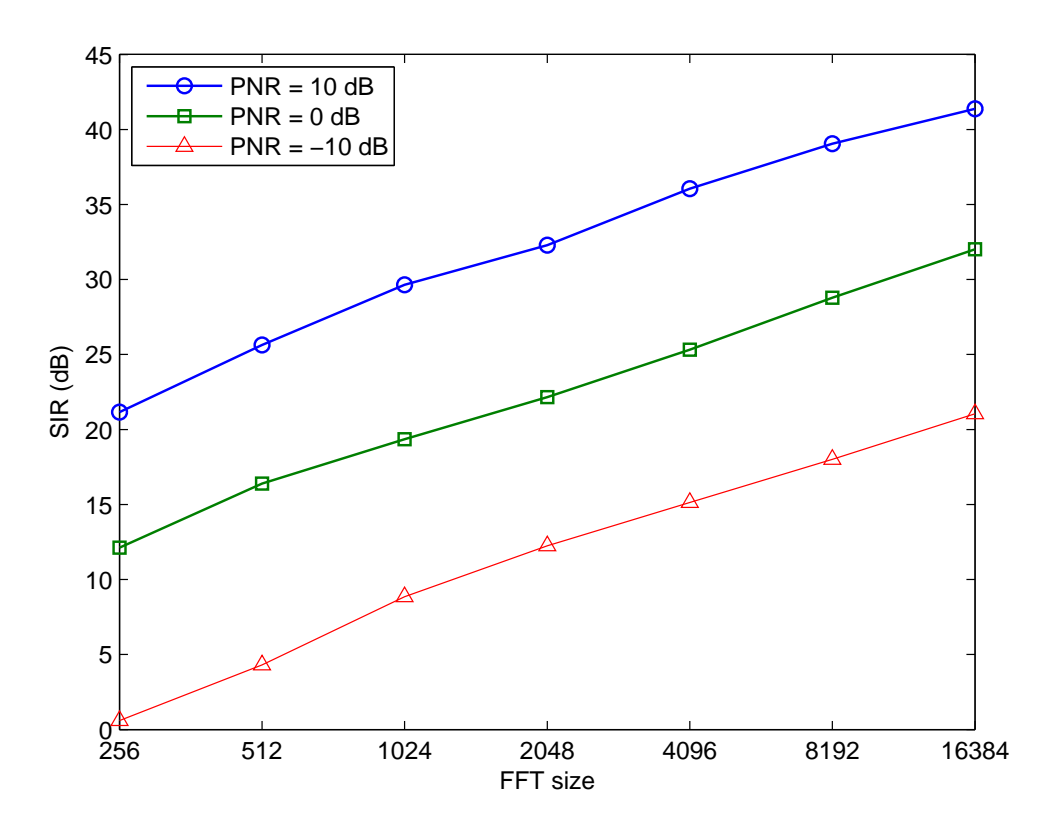


Figure 3.5: SIR using DFT-based spatial equalizer.

grows. This does not seriously degrade the SIR over the duration our simulation (due to assumption of small frequency offset estimation error). However, for larger expected frequency estimation error, the observation window length or observation weighting should be selected with this in mind. The LS estimator can be implemented as a recursive algorithm, allowing for a large observation window and limited computational complexity. Assuming the carrier offset is estimated

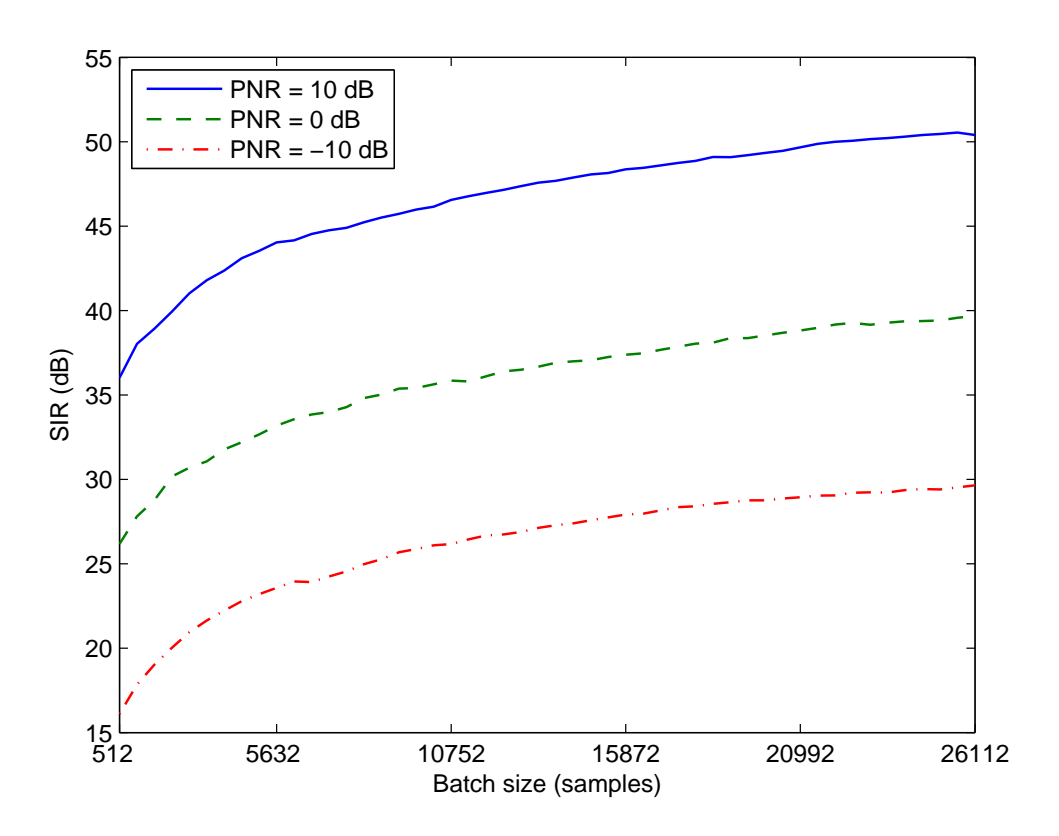


Figure 3.6: SIR using LSE-based spatial equalizer.

accurately, this allows the LS estimator to achieve a higher SIR than the other methods we consider.

Finally, we consider the closed-loop FFT-based spatial equalizer. A 512-point FFT is performed after each perturbation of the equalizer weights. The average SIR is plotted as a function of control loop iterations in Fig. 3.6 for several values of PNR. We observe that over the course of the first roughly twenty iterations, the SIR increases by nearly 20 dB. This can be attributed to the equalizer rapidly

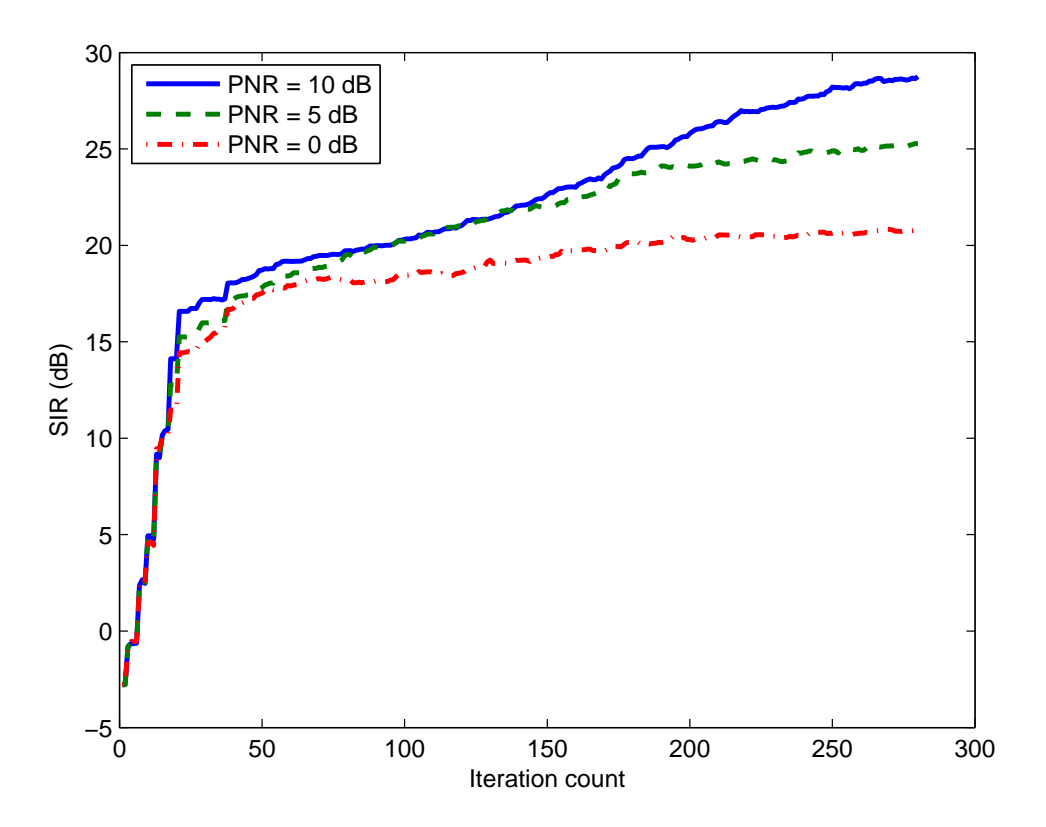


Figure 3.7: SIR using closed-loop spatial equalizer.

converging to a coarse approximation of the optimal equalizer weights. Further refinement of the equalizer weights is then possible as the perturbations are gradually reduced in magnitude. Compared to the other equalization schemes, this method adapts relatively slowly over time. At a minimum, it takes roughly 80 ms to obtain an SIR of 15 dB, and 800 ms to obtain an SIR of 25 dB at a PNR of 10 dB. In practice, however, this process can take significantly longer depending on the hardware implementation, as described in the next section.

# 3.3 Hardware Prototype

The two-level mm-wave MIMO architecture was implemented as a 60 GHz hardware prototype using commercially available mm-wave and RF components and a printed circuit board spatial equalization network. The prototype was initially designed as a two-channel 60 GHz MIMO link with a manually tuned spatial equalization network that operated at IF frequencies. This system successfully demonstrated point-to-point 60 GHz in both short-range (5 m) indoor [41] and longer range (41 m) outdoor environments [14]. The most recent version of the prototype, described in this section and [15], features four-channel communication with a aggregate data rate of 2.4 Gbps and adaptive spatial equalization applied at baseband. The spatial equalizer is adapted using the iterative FFT-based procedure described in Section 3.2.

The prototype was demonstrated in an indoor office environment at a link range of 5 m. Experimental results provided at the end of this section include bit error rate (BER) and SIR measurements.

#### 3.3.1 Transmitter and Receiver Electronics

The transmitter is shown in Fig. 3.8. Four data bitstreams are generated by an FPGA at a rate of 600 Mbps. The FPGA implements four linear feedback

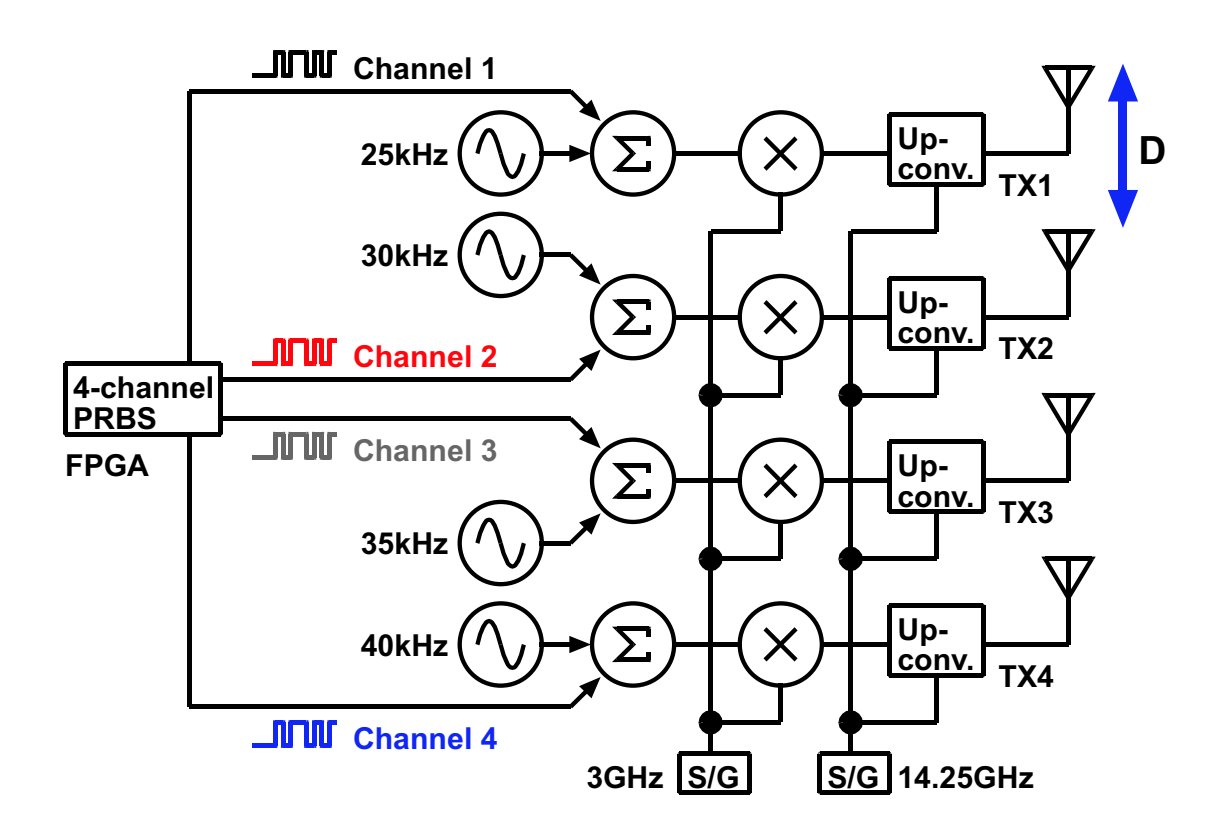


Figure 3.8: Transmitter prototype block diagram.

shift registers (LFSRs) which produce maximum-length pseudorandom binary sequences (PRBSs) of lengths  $2^{20} - 1$ ,  $2^{22} - 1$ ,  $2^{23} - 1$ , and  $2^{25} - 1$  bits. The digital bit sequences are converted to antipodal analog signals and each is combined with pilot tone of 30 kHz, 35 kHz, 40 kHz, or 45 kHz. The combined signals are upconverted to 3 GHz IF and then to 60 GHz RF before being transmitted over a ULA of four 24 dBi standard gain horn antennas. The inter-antenna spacing is chosen as 7.9 cm, which satisfies the Rayleigh criterion given the 5 m link range.

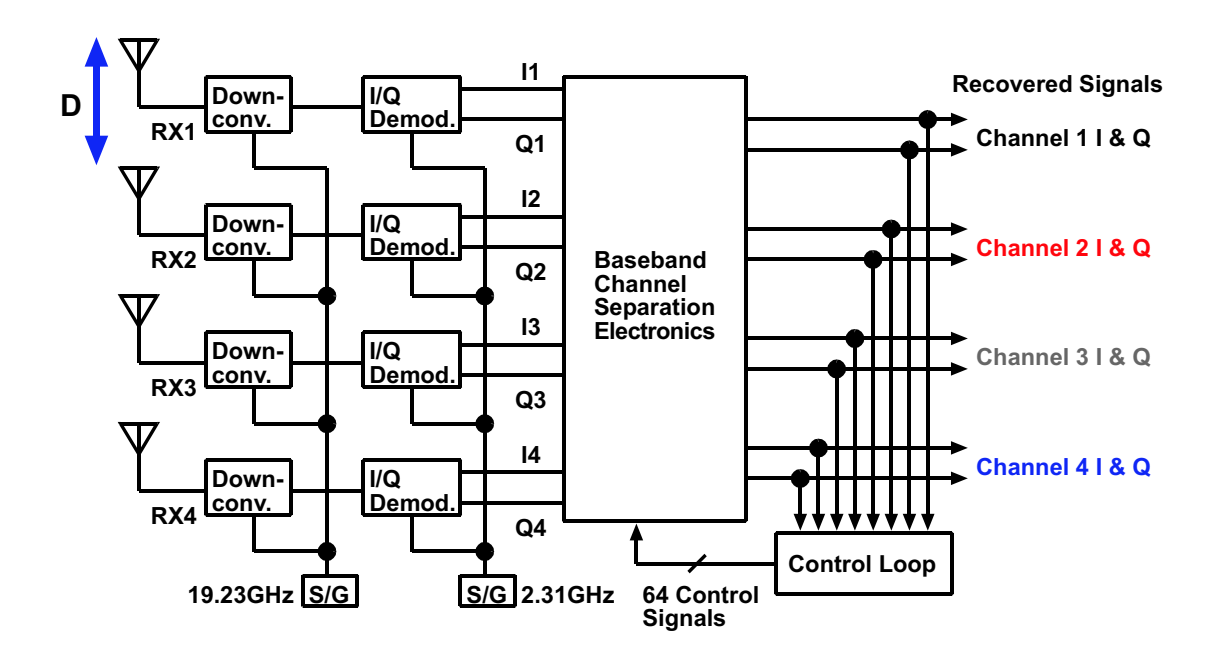


Figure 3.9: Receiver prototype block diagram.

The receiver, shown in Fig. 3.9, receives the signals over a four-element Rayleigh-spaced array consisting of 24 dBi horn antennas. The received signals are downconverted to a 2.31 GHz IF frequency, and I/Q demodulators convert the IF signal to baseband. The I and Q signals are split and distributed to eight spatial equalization boards, which individually recover the I or Q components of a single channel. The boards include an array of VGAs, implemented as full four-quadrant analog multipliers. This allows an arbitrary complex gain to be applied to each received signal. The scaled signals are summed using an 8:1 resistor power combiner matched to 50  $\Omega$ . The recovered signals were digitized using

two-channel oscilloscope and stored on a computer for offline Differential PSK (DPSK) demodulation and bit error rate analysis.

The VGAs are adaptively tuned using the closed-loop FFT-based equalization method previously described. The received signals are low-pass filtered and sampled at a rate of 125 kHz, which can achieved using low-cost multi-channel ADCs. An FFT of the digitized signals is performed and analyzed using a laptop computer, which outputs control signals that run through a 64-channel D/A converter board to the VGAs. An update of all 64 VGA voltages takes on the order of one second and is sufficient to track slowly-varying changes in the channel. The update time could be reduced by using a faster D/A interface, which is the limiting factor to the loop speed.

## 3.3.2 Experimental Results

To evaluate the prototype's performance, the transmitter and receiver were tested in an office environment at a 5 m link range as shown in Fig. 3.10. Table 3.1 provides a link budget of the experimental setup.

Spatial equalizer performance was evaluated in a two stage process. First, the adaptive equalizer control loop was allowed to run until the SIR stabilized. Next, the interfering signals were switched off, and the received power spectrum of the desired signal was measured at the output of the spatial equalizer. Then,

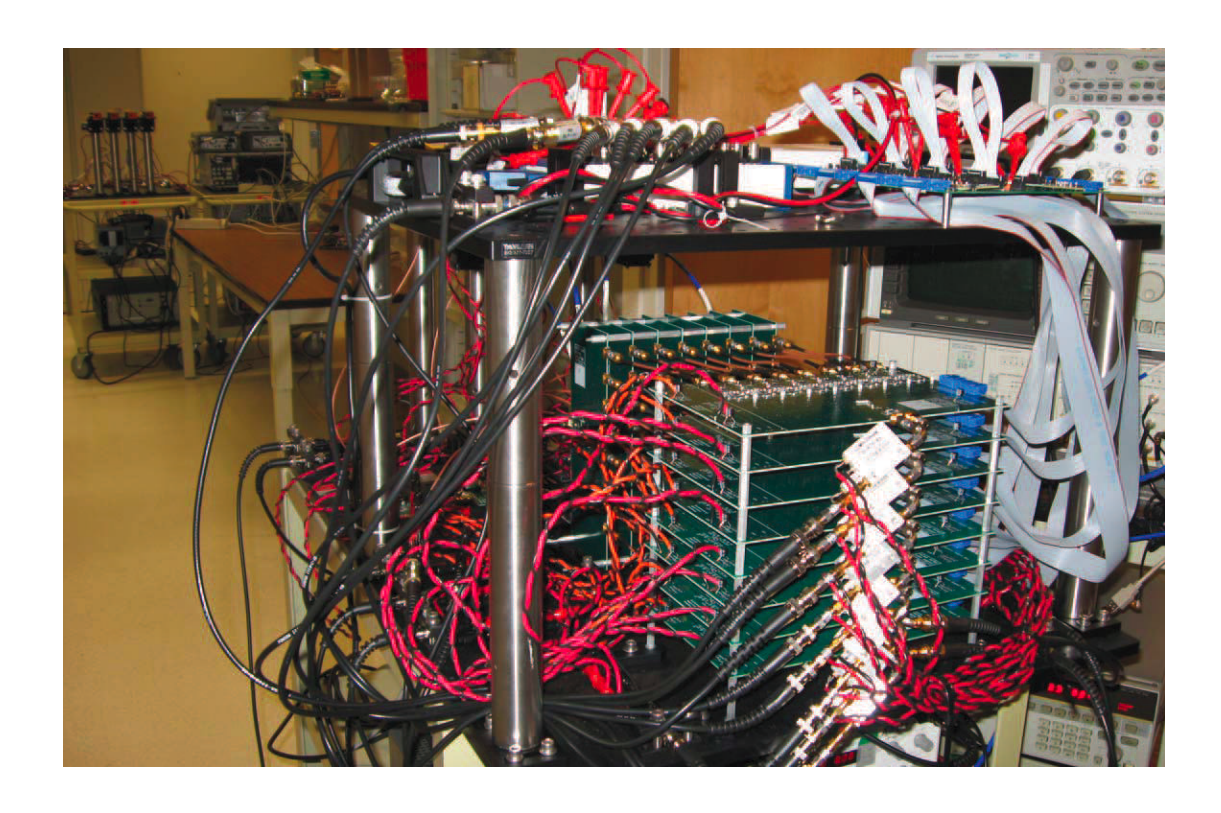


Figure 3.10: Photograph of prototype receiver.

the desired channel was switched off, the interfering signals were re-activated, and their power was measured. In this manner, the powers of the desired signal and interference was measured for each of the four channels. The received power spectrums are shown in Fig. 3.11, and the SIR for each channel is provided in Table 3.2. Channels 1, 2, and 4 had similar interference suppression performance. The relatively poor performance of channel 3 is due to the third signal being received with less power. Additional measurements are required to determine the underlying cause.

Table 3.1: Link budget

TX antenna gain	24	dBi
RX antenna gain	24	dBi
Link range	5	m
Free-space path loss	82	dB
Rx noise figure	14	dB
BER	$10^{-6}$	
Link margin	17	dB
Tx Power	-10	dBm
Rx Power	-44	dBm

Table 3.2: SIR and BER Measurements

Recovered Channel	BER	SIR (dB)
1	$< 10^{-6}$	15
2	$< 10^{-6}$	12
3	$1.2 \times 10^{-5}$	10
4	$< 10^{-6}$	14

To perform BER measurements, the I and Q channels at the output of the spatial equalizer were sampled using an oscilloscope and stored offline on a computer. To assess the impact of spatial interference, the BER measurements were performed in two stages. First, signals were transmitted individually to measure BER in the absence of interference. Second, all transmitters were activated simultaneously and the BER was measured again. In both cases, the symbols were demodulated using differential binary phase shift keying (DBPSK) and the symbol sequence was compared to the appropriate PRBS sequence. For single active channels, the BER was estimated to be below 10<sup>-6</sup> for each channel. With all

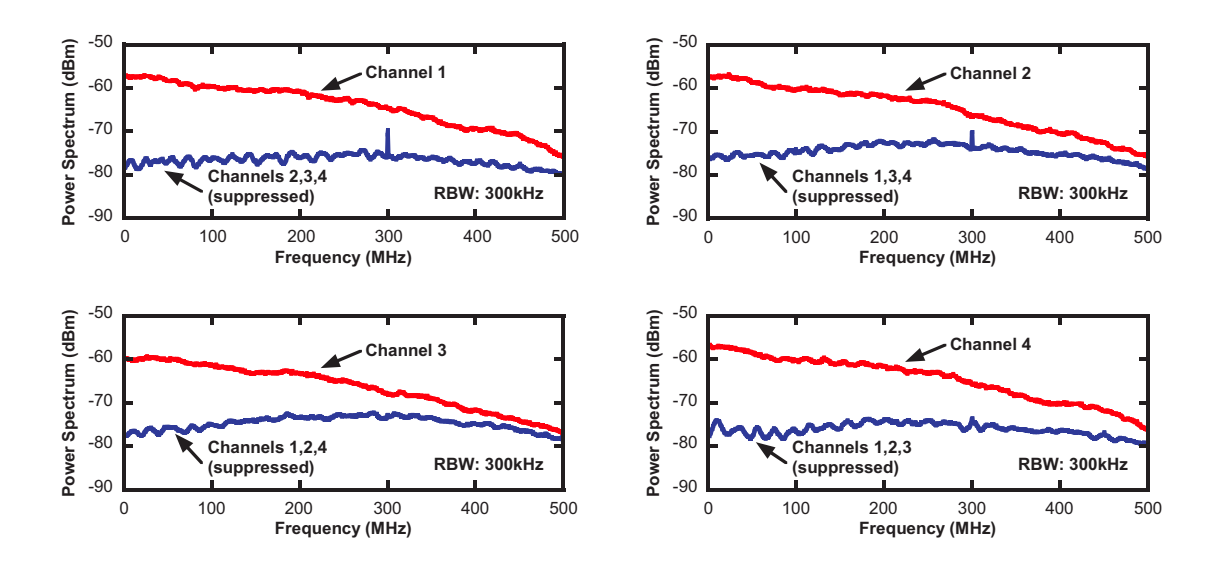


Figure 3.11: Measured power spectrums of signals and interference.

transmitters active, the BER performance was similar for the first, second, and fourth channels. The third channel, which exhibited a lower SIR, had a measured BER of  $1.2 \times 10^{-5}$ . The BER performance is summarized in 3.2. The eye patterns of the received signals after DPSK demodulation are shown in Fig. 3.12. The variations in eye closure are consistent with the SIRs as measured using the power spectrums.

## 3.4 Discussion

In this chapter, we considered how conventional channel estimation methodology, based on the assumption of full precision sampling, creates an ADC bottleneck as signals scale to multi-GHz bandwidths. We proposed a two-level architecture that decouples the processing tasks of spatial equalization and data demodulation. By performing these tasks at separate time scales, the need for costly high-precision, high-speed ADCs is avoided. We considered several methods of computing the spatial equalizer weights, based either on channel estimation or closed-loop adaptation, and we evaluated their performance through simulation. Low signal-to-interference ratios can be achieved using any of the proposed methods, and each offers various tradeoffs in terms of their implementation complexity. There remain open questions regarding the adaptive scheme, as it is not yet clear what perturbation weights are optimal, or whether they could be adapted in a more efficient manner.

A four-channel hardware prototype operating at 60 GHz offers proof-of-concept for LOS mm-wave MIMO multiplexing and the two-level architecture. Experimental results suggest that two-level architecture is a viable approach for practical mm-wave MIMO systems.

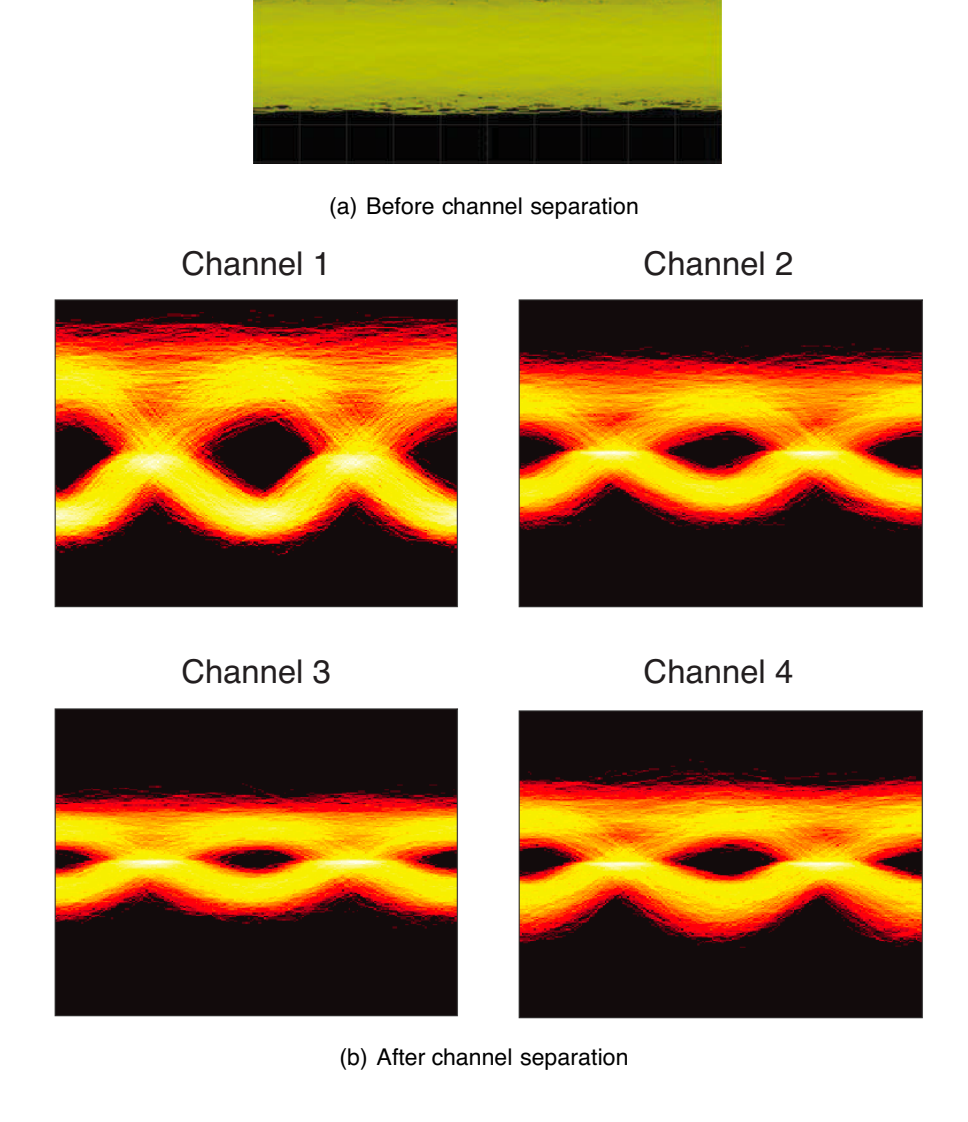


Figure 3.12: Eye patterns before and after equalization.

# Chapter 4

# Feasibility and Performance Study of Indoor mm-Wave MIMO Links

In this chapter, we evaluate the feasibility of mm-wave MIMO links designed for short-range indoor applications. This scenario requires that we consider the effects of array form factor constraints, potential LOS blockage, and multipath reflections. We begin by establishing fundamental limits on the number of spatial degrees of freedom available over a LOS channel given array length constraints. We find that the Rayleigh spaced arrays described in Chapter 2 are essentially optimal in terms of maximizing the spatial degrees of freedom. Increasing the antenna count further primarily provides beamforming gain. This motivates a proposed array-of-subarrays architecture, whose performance we evaluate in a simulated indoor environment. A practical transmit beamsteering/receive MMSE scheme is compared against a waterfilling benchmark in both LOS and NLOS

settings, and variations in channel capacity due to node placement are examined. We find that significant spatial multiplexing gains are available throughout the indoor environment. While LOS blockage can substantially reduce throughput at low power levels, this effect is lessened when the spectral efficiency is limited by the use of small signal constellations, which are commonly used in practice due to the limited power levels generated by mm wave electronics.

The chapter is organized as follows. In Section 4.1, we review the array geometry criterion that guarantees an orthogonal channel matrix for LOS MIMO. We then show that this is near-optimal by deriving a limit on the number of spatial degrees of freedom with array length (i.e. form factor) constraints. An system architecture that provides array gain and spatial multiplexing gain is introduced in Section 4.2. An indoor environment modeled using ray-tracing techniques is described in Section 4.3. In Section 4.4, the performance of the proposed architecture is evaluated in terms of channel capacity under LOS and non-LOS (NLOS) conditions. Conclusions are discussed in Section 4.5.

### 4.1 Fundamental Limits of LOS MIMO

In this section, we derive limits on the number of spatial degrees of freedom of a LOS MIMO channel given array length constraints. We find that the form factors of typical consumer electronics devices are sufficient to allow multiple degrees of freedom.

#### 4.1.1 LOS MIMO Channel Model

We briefly restate the channel model introduced in Chapter 2. Consider a link consisting of two N-element arrays. Assuming a flat-fading MIMO channel, the received signal vector  $\mathbf{y} \in \mathbb{C}^{N \times 1}$  is given by

$$y = Hx + w, (4.1)$$

where  $\mathbf{x} \in \mathbb{C}^{N \times 1}$  is the transmitted signal vector,  $\mathbf{H} \in \mathbb{C}^{N \times N}$  is the channel matrix,  $\mathbf{w} \in \mathbb{C}^{N \times 1}$  is additive complex white Gaussian noise with with covariance  $N_0 \mathbf{I}_{N_t}$ , and  $\mathbf{I}_N$  is the  $N \times N$  identity matrix. In a purely LOS channel, the complex channel gain  $h_{m,n}$ , representing the (m,n)th element of  $\mathbf{H}$ , can be modeled as

$$h_{m,n} = \frac{\lambda}{4\pi p_{m,n}} \exp\left(-j\frac{2\pi}{\lambda}p_{m,n}\right),\tag{4.2}$$

where  $\lambda$  is the carrier wavelength and  $p_{m,n}$  is the path length from the *n*th transmit antenna to the *m*th receive antenna.

Assuming the arrays are uniformly-spaced and aligned broadside, the path length is given by  $p_{m,n} = \sqrt{R^2 - (md_T - nd_R)^2}$ , where R is the link range, and  $d_R$  and  $d_T$  denote the distance between neighboring receive antennas and transmit antennas, respectively. When R is much larger than the length of either array, we

can approximate the path length by  $p_{m,n} \approx R + (md_t - nd_r)^2/(2R)$ . The channel gain is then

$$h_{m,n} \approx \frac{\lambda}{4\pi R} \exp\left(-j\frac{2\pi}{\lambda} \left(R + \frac{(md_T - nd_R)^2}{2R}\right)\right).$$
 (4.3)

In contrast to a NLOS MIMO channel, which is highly dependent on the surrounding multipath scattering environment, we note that the LOS MIMO channel is specified by the carrier frequency and the relative positions of the array elements. We first consider the setting where the number of antenna elements (rather than the array lengths) is fixed. We demonstrated in Chapter 2 that the optimal uniform spacing is given by

$$d_T d_R = \frac{R\lambda}{N}. (4.4)$$

When this condition holds, **H** is a scaled unitary matrix with equal singular values, which we denote by  $\sigma_n$  for n = 1, ..., N. Each non-zero singular value corresponds to an eigenmode (or eigenchannel) over which data can be transmitted. We refer to a pair of arrays satisfying (4.4) as Rayleigh spaced or optimally spaced ULAs.

Now, if the lengths of the transmit and receive arrays are constrained and N is arbitrary, we can determine from (4.4) the maximum number of antennas that can be supported while preserving the orthogonality condition. Noting that the length of a ULA is given by L = d(N-1), where d is the inter-element spacing,

and solving (4.4) for N, the maximum number of antennas is given by

$$N_U = \left[1 + \frac{L_T L_R}{2\lambda R} + \frac{1}{2} \sqrt{\left(2 + \frac{L_T L_R}{\lambda R}\right)^2 - 4}\right],\tag{4.5}$$

where  $L_T$  is the maximum transmit array length,  $L_R$  is the maximum receive array length, and |a| is the largest integer less than or equal to a.

Equation (4.5) specifies the maximum number of spatial degrees of freedom available to a LOS MIMO link while satisfying both the orthogonality condition and a set of array length constraints. Such a design may be termed an *optimally spaced sparse array*, where the sparsity is required for orthogonality. In the next section, we investigate what can be gained by forgoing orthogonality and increasing the antenna count of our fixed-length arrays beyond  $N_U$ .

## 4.1.2 Spatial Degrees of Freedom

Equation (4.5) specifies the maximum number of spatial degrees of freedom available to a LOS MIMO link while satisfying both the orthogonality condition and a set of array length constraints. We may ask what can be gained by forgoing orthogonality and increasing the antenna count of our fixed-length arrays beyond  $N_U$ . We first consider two LOS MIMO links as an example. The first link uses optimally spaced arrays, with N=8,  $\lambda=5$  mm, R=5 m, and  $L_T=L_R=39.1$  cm. The squared singular values the associated channel matrix, plotted in Fig. 4.1, are

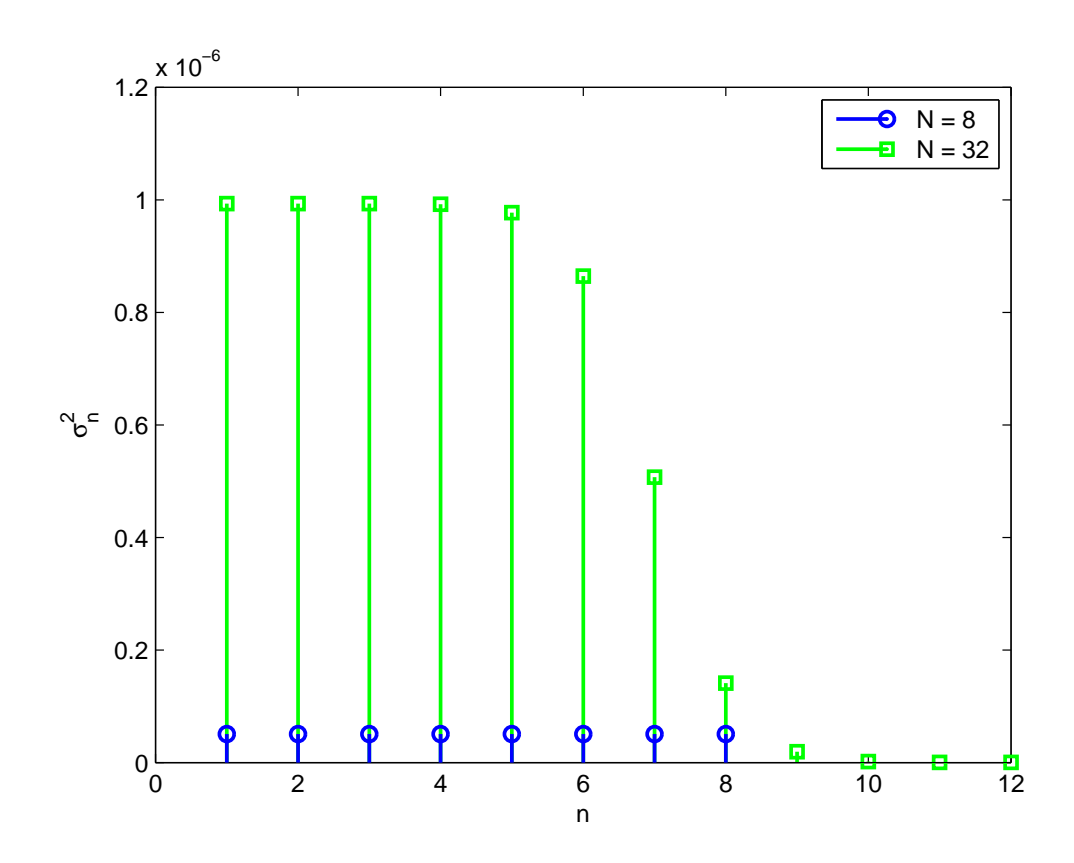


Figure 4.1: Squared singular values of discrete ULA channel matrix.

of equal value, as expected. The arrays of the second link also have lengths of 39.1 cm, but the number of uniformly spaced elements is increased fourfold to N=32. Fig. 4.1 plots the largest twelve squared singular values. We observe that the additional antennas provide mostly power gains to the first eight eigenchannels rather than degree of freedom gains. The additional eigenvalues are significantly weaker and drop off rapidly to zero.

To see whether this result continues to hold for larger N, we take the limit as N approaches infinity. Based on our observation of Fig. 4.1, namely that

additional antennas seem to yield primarily array processing gains to the first  $N_U$  eigenmodes, we may expect the squared singular values to increase in proportion to  $N^2$ . This follows from the fact that, under a transmit power constraint, transmit beamforming and receive beamforming each provide a factor of N power gain. We therefore introduce a normalized form of the channel matrix given by

$$\tilde{\mathbf{H}} = \frac{4\pi R}{\lambda N} \mathbf{H},\tag{4.6}$$

where the 1/N scaling factor normalizes the squared singular values by  $1/N^2$ . With this choice of normalization,  $\sum_{n=1}^{N} \tilde{\sigma}_n^2 = 1$ , where  $\tilde{\sigma}_n$  are the singular values of  $\tilde{\mathbf{H}}$ . Substituting  $\tilde{\mathbf{H}}$  for  $\mathbf{H}$  in (4.1) and disregarding additive noise, the signal at the kth receive antenna is given by

$$y_k = \frac{1}{N} \sum_{m=0}^{N} \exp\left(-j\frac{2\pi}{\lambda} \left(R + \frac{(md_T - nd_R)^2}{2R}\right)\right) x_m. \tag{4.7}$$

In the limit as N goes to infinity and the interelement spacing becomes infinitesimal, we can express the received signal at point  $p \in [-L_R/2, L_R/2]$  on the receive array as

$$y(p) = \frac{1}{L_T} e^{-j\frac{2\pi}{\lambda}R} \int_{-L_T/2}^{L_T/2} e^{-j\frac{2\pi}{\lambda}\frac{(q-p)^2}{2R}} x(q) dq, \tag{4.8}$$

where x(q) is the transmitted signal at point  $q \in [-L_T/2, L_T/2]$  on the transmit array.

The integral kernel

$$G(p,q) = \frac{e^{-j\frac{2\pi}{\lambda}R}}{L_T} e^{-j\frac{2\pi}{\lambda}\frac{(q-p)^2}{2R}}.$$
 (4.9)

was previously studied in the context of the diffraction limited optics by Thaning et al. in [42], and the analysis here follows their approach. Equation (4.9) can be expanded via the spectral theorem as

$$G(p,q) = \sum_{n=1}^{\infty} g_n a_n^*(q) b_n(p), \tag{4.10}$$

where  $g_n$  and  $a_n(q)$  are the eigenvalues and eigenfunctions of the integral equation

$$|g_n|^2 a_n(q) = \int_{-L_T/2}^{L_T/2} K(q', q) a_n(q') dq', \qquad (4.11)$$

and where

$$K(q',q) = \int_{-L_R/2}^{L_R/2} G^*(p,q)G(p,q')dp.$$
 (4.12)

The functions  $b_n(p)$  are defined by

$$g_n b_n(p) = \int_{-L_T/2}^{L_T/2} G(p, q) a_n(q) dq.$$

The functions  $a_n(q)$ , which are ordered such that  $|g_1| \geq |g_2| \geq \ldots \geq |g_n|$ , form an orthonormal set over the interval  $[-L_T/2, L_T/2]$ , and hence the received signal can be expressed as

$$y(p) = \sum_{n=1}^{\infty} g_n A_n b_n(p), \qquad (4.13)$$

where

$$A_n = \int_{-L_T/2}^{L_T/2} a_n^*(p_T) x(p_T) dp_T.$$

We note that, although y(p) is represented in (4.13) by an infinite summation, y(p) can be represented to a given level of accuracy using only a finite number of terms.

Expressing the eigenfunctions in the form

$$a_n(q) = \exp\left(j\frac{\pi}{\lambda R}q^2\right)\alpha_n(q),\tag{4.14}$$

we can substitute (4.14) and (4.12) into (4.11) to obtain the following equation

$$\frac{L_T^2}{\lambda R} |g_n|^2 \alpha_n(q) = \int_{-L_T/2}^{L_T/2} \frac{\sin 2\pi W (q - q')}{\pi (q - q')} \alpha_n(q') dq', \tag{4.15}$$

where  $W = L_R/(2\lambda R)$ . The integral equation (4.15) defines a set of prolate spheroidal wavefunctions (PSWFs), a family of functions investigated extensively by Slepian et al. in the context of bandlimited and approximately time-limited signals. The eigenvalues  $|g_n|^2$  are related to  $v_n$ , the eigenvalues of the PSWFs, by  $|g_n|^2 = v_n \lambda R/L_T^2$ . A well-known property of the PSWFs is that their eigenvalues remain approximately equal to one until n nears a critical value, given here by

$$S = 2WL_T = \frac{L_T L_R}{\lambda R},\tag{4.16}$$

after which they drop off rapidly to zero. Correspondingly,  $A_n$  drops off to zero for n > S, and the received signal y(p) is specified to a high degree of accuracy by the first S + 1 values of  $A_n$ . We conclude that the number of degrees of freedom of the continuous array link is limited to approximately

$$N_C = \frac{L_T L_R}{\lambda R} + 1. (4.17)$$

 $N_C \approx N_U$ , although as a result of factoring out the beamforming gain,  $N_C$  is generally a more conservative estimate of the degrees of freedom.

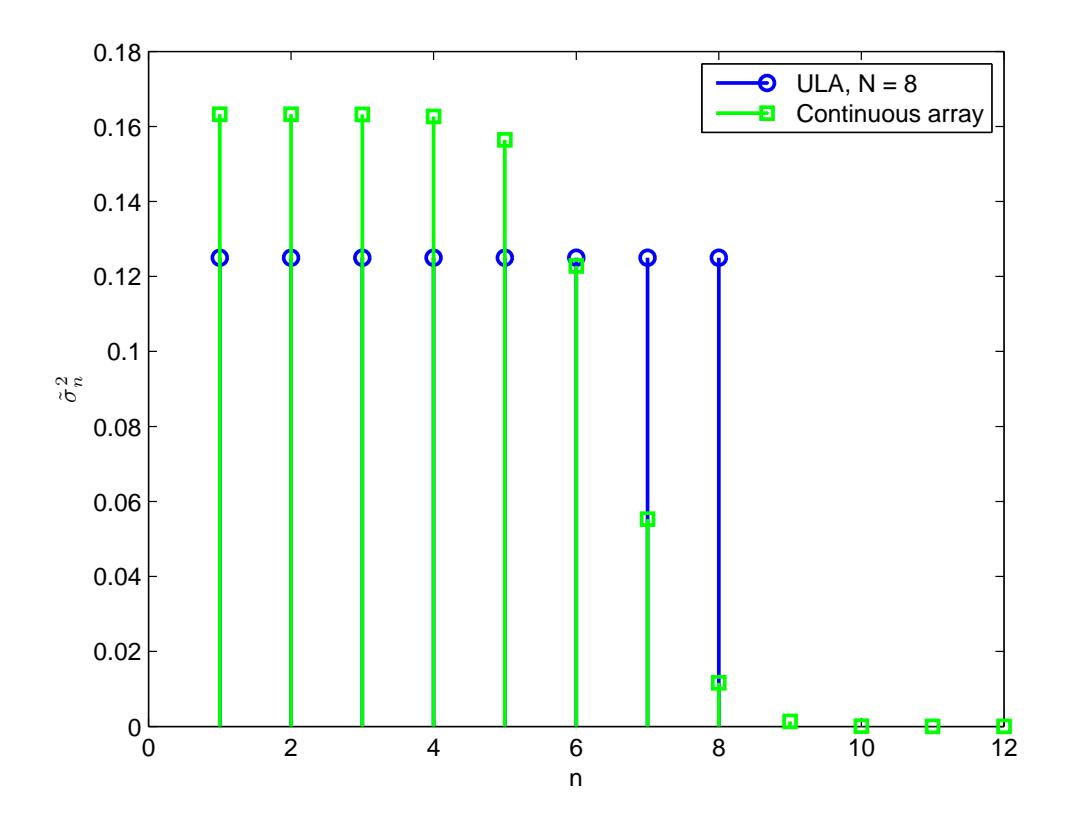


Figure 4.2: Eigenvalues of continuous array channel.

Fig. 4.2 plots the first twelve eigenvalues of the continuous array channel,  $|g_n|^2$  for  $n=1,\ldots,12$ , when R=5 m, and  $L_T=L_R=39.1$  cm. Their transition to zero is centered around S=6.125, in agreement with (4.16). Relating these results to discrete ULAs, we observe that for large values of N, the squared singular value  $\sigma_n^2$  increases by an amount proportional to  $|g_n|^2$  when an additional element is added to the array. Thus  $|g_n|^2$  describe how the power gain provided by an

additional antenna is distributed among the eigenchannels of a ULA link when  $N \gg N_U$ . Comparing Fig. 4.2 and Fig. 4.1, we find that squared singular values of the N=32 ULA link are approximately proportional to the continuous array eigenvalues.

The preceding asymptotic analysis yields fairly specific guidelines for transceiver design. First, increasing antenna count beyond the optimally spaced sparse design is an impractical means of increasing the number of degrees of freedom: while the power gain may be sufficient that more than  $N_U$  eigenchannels are utilized under a given power allocation scheme, these modes will remain significantly weaker than the dominant modes. Indeed, for the form factors and ranges of interest for indoor mm-wave MIMO, the number of dominant modes is already quite large. However, while optimally spaced sparse arrays are, in fact, near-optimal in the number of spatial degrees of freedom they provide, our analysis also indicates that the SNR per degree of freedom can be significantly improved by increasing the number of elements. This observation motivates the array of subarrays architecture presented in the following section.

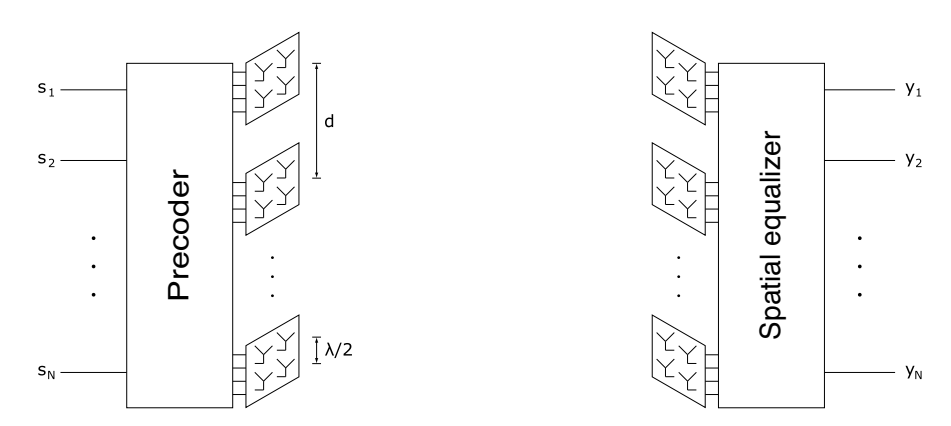


Figure 4.3: Array of subarrays architecture.

#### 4.2 LOS mm-Wave MIMO Architecture

Our proposed MIMO transceiver architecture in Fig. 4.3 is based on the preceding optimal spacing criterion given by (4.4). N independent data streams are precoded and transmitted over an N-element optimal ULA, where the spacing d is chosen to satisfy (4.4) given an expected link range  $R_o$ . Each element of the ULA is a square  $\lambda/2$ -spaced subarray, which can be implemented as a monolithic millimeter wave integrated circuit. Because the spacing between subarray elements is small, the subarrays provide array gain rather than spatial multiplexing gain. The additional directivity helps to offset propagation loss at mm-wave frequencies and attenuate multipath. Each subarray is an  $M \times M$  square array, so the total number of antennas per node is given by  $N_T = NM^2$ . The receiver consists of an identical array-of-subarrays structure, with received signals feeding

into a equalizer designed to null spatial interference. We now describe two spatial equalization and modulation schemes based on the above architecture.

#### 4.2.1 Waterfilling Benchmark

Our performance benchmark is standard waterfilling based eigenmode transmission. This employs a transmit precoder and a receive spatial equalizer based on the singular value decomposition (SVD) of the channel matrix  $\mathbf{H}$ , such that the channel is decomposed into N non-interfering parallel subchannels, or eigenmodes. The SVD of the channel matrix  $\mathbf{H}$  is given by

$$H = U\Sigma V^H$$
,

where  $\mathbf{U}, \mathbf{V} \in \mathbb{C}^{N_T \times N_T}$  are unitary and  $\mathbf{\Sigma} \in \mathbb{R}^{N_T \times N_T}$  is a diagonal matrix whose nonzero entries are the ordered singular values of  $\mathbf{H}$ , given by  $\sigma_1 \geq \sigma_2 \geq \ldots \geq \sigma_{N_T}$ . Let  $\mathbf{V}_N$  and  $\mathbf{U}_N$  denote the matrices composed of the first N columns of  $\mathbf{V}$  and  $\mathbf{U}$ , respectively. The data vector  $\mathbf{s}$  is premultiplied by  $\mathbf{V}_N$  at the transmit precoder stage and the received data  $\mathbf{r}$  is filtered by  $\mathbf{U}_N^H$ , resulting in

$$\mathbf{y} = \mathbf{U}_N^H \mathbf{r} = \mathbf{U}_N^H (\mathbf{H} \mathbf{V_N} \mathbf{s} + \mathbf{w}) = \mathbf{\Sigma}_N \mathbf{s} + \tilde{\mathbf{w}},$$

where  $\Sigma_N$  is the  $N \times N$  submatrix consisting of the first N columns and N rows of  $\Sigma$ . Note that the distribution of the noise component remains unchanged because the columns of  $U_N$  are orthonormal. Effectively, the channel is decomposed into

N parallel subchannels of the form

$$y_i = \sigma_i s_i + \tilde{w}_i$$
  $i = 1, 2, \dots, N$ .

The channel capacity, given by

$$C = \sum_{i}^{N} \left( \log \frac{\mu \sigma_i^2}{N_0} \right)^+, \tag{4.18}$$

is achieved when the input symbols  $s_i$  are Gaussian distributed and the power allocated to the *i*th channel, denoted by  $P_i = E[|s_i|^2]$ , obeys the waterfilling power allocation policy.  $P_i$  is given by

$$P_i = \left(\mu - \frac{N_0}{\sigma_i^2}\right)^+,\tag{4.19}$$

where  $a^+$  indicates  $\max\{0, a\}$ , the value of  $\mu$  is chosen such that  $\sum_i P_i = P_T$ , and  $P_T$  is a total power constraint. If  $(\mu - N_0/\lambda_i^2) < 0$ , no power or data is allocated to the *i*th eigenchannel.

#### 4.2.2 Transmit Beamsteering/Receive MMSE

While the previous scheme provides an upper bound on link performance, it is important to identify more conservative performance estimates that represent typical hardware and signal processing constraints. To this end, we consider a scheme in which the transmitter sends a single data stream from each subarray, with each subarray limited to beamsteering in a given direction. We assume the transmitter

knows the directions of the LOS and first-order reflection paths to the receiver (these can be learned by scanning at start-up), and beamsteering is constrained along these paths. The transmitter beamsteers in the direction(s) that maximize the sum-rate spectral efficiency. The constellation per data stream is fixed (we use 16QAM in our numerical results). The spatially multiplexed data streams can now interfere with each other, and we employ linear MMSE spatial interference suppression to separate them out at the receiver.

Note that, as demonstrated in recent hardware prototypes [15], spatial processing (e.g., linear interference suppression) for a quasi-static channel can be performed in our architecture on a slow time scale using (digitally controlled) analog processing, thus avoiding the need for high-speed analog-to-digital converters (ADCs) with large dynamic range. Digitization can be performed with ADCs with lower dynamic range after separation of the multiplexed data streams.

The beamsteering weight applied to the antenna in the kth column and lth row of the jth subarray is given by

$$a_{jkl} = \exp(-i\pi((k-1)\cos\theta_j\sin\phi_j + (l-1)\cos\phi_j)) \quad k, l \in \{1, 2, \dots, M\},$$

$$(4.20)$$

where  $\theta_j$  and  $\phi_j$  are the azimuthal and polar steering angles, respectively. Let  $a_{jkl}$  be the (k,l)th entry of the  $M \times M$  matrix  $\mathbf{A}(\theta_j,\phi_j)$  and let  $\mathbf{a}(\theta_j,\phi_j) = \text{vec}(\mathbf{A}(\theta_j,\phi_j))$  be the vector formed from concatenating the columns of  $\mathbf{A}(\theta_j,\phi_j)$ .

The precoding matrix G is given by

$$\mathbf{G} = \frac{1}{M} \begin{pmatrix} \mathbf{a}(\theta_1, \phi_1) & \mathbf{0} & \cdots & \mathbf{0} \\ \mathbf{0} & \mathbf{a}(\theta_2, \phi_2) & \cdots & \vdots \\ \vdots & \vdots & \ddots & \mathbf{0} \\ \mathbf{0} & \cdots & \mathbf{0} & \mathbf{a}(\theta_N, \phi_N) \end{pmatrix}$$
(4.21)

where **0** is an  $M^2 \times 1$  vector of zeros.

At the receiver, full channel state information is assumed. The input to the spatial equalizer is given by

$$\mathbf{r} = \mathbf{HGs} + \mathbf{w} = \mathbf{\hat{H}s} + \mathbf{w} \tag{4.22}$$

where  $\mathbf{s}$  is the  $N \times 1$  data vector,  $\mathbf{G}$  is the  $NM^2 \times N$  steering matrix, and  $\hat{\mathbf{H}} = \mathbf{H}\mathbf{G}$  is an  $NM^2 \times N$  equivalent channel matrix combining the propagation environment and the steering matrix. We now assume equal power allocation across data streams, such that  $E[|s_i|^2] = P_T/N$ . The equalizer output is given by

$$\mathbf{y} = \mathbf{C}^H \mathbf{r} = \mathbf{C}^H \left( \hat{\mathbf{H}} \mathbf{s} + \mathbf{w} \right) \tag{4.23}$$

where equalizer coefficients are specified by **C**. The coefficients of the MMSE equalizer are given by

$$\mathbf{C}_{\text{MMSE}} = \left(\frac{P_T}{N}\hat{\mathbf{H}}\hat{\mathbf{H}}^H + P_N \mathbf{I}_{NM^2}\right)^{-1} \frac{P_T}{N}\hat{\mathbf{H}},\tag{4.24}$$

where  $P_N = N_0 B$  is the noise power and B is the bandwidth.

The signal to interference and noise ratio (SINR) at the kth output of the equalizer is given by

$$\gamma_k = \frac{\frac{P_T}{N} |\mathbf{c}_k^H \hat{\mathbf{H}}_k|^2}{\frac{P_T}{N} \sum_{j \neq k} |\mathbf{c}_j^H \hat{\mathbf{H}}_k|^2 + P_N \mathbf{c}_k^H \mathbf{c}_k},$$
(4.25)

where  $\mathbf{c}_k$  is the kth column of  $\mathbf{C}_{\text{MMSE}}$ . The spectral efficiency is computed with the interference treated as Gaussian noise, and with the symbol constellation restricted to 16-QAM.

# 4.3 Indoor Propagation Model

The optimal antenna spacing criterion given by (4.4) assumes the transmit and receive arrays are aligned parallel, the channel is purely LOS, and the link range is known *a priori*. For practical indoor applications, none of these assumptions hold, and we wish to evaluate the performance of the proposed architecture when operating under more realistic scenarios. To this end, we present a indoor environment propagation model that allows us to assess the impact of multipath propagation, link range variations, and LOS blockage.

The propagation environment, shown in Fig. 4.4, is a room of dimensions 5 m  $\times$  5 m  $\times$  3 m. The receive array lies horizontally along the plane of the front wall, centered at coordinates (2.5 m, 0, 1.5 m). The transmitter's position is variable, and given by coordinates (x, y, 1.5 m), where  $0 \le x \le 5 \text{ m}$  and  $0 \le y \le 5 \text{ m}$ .

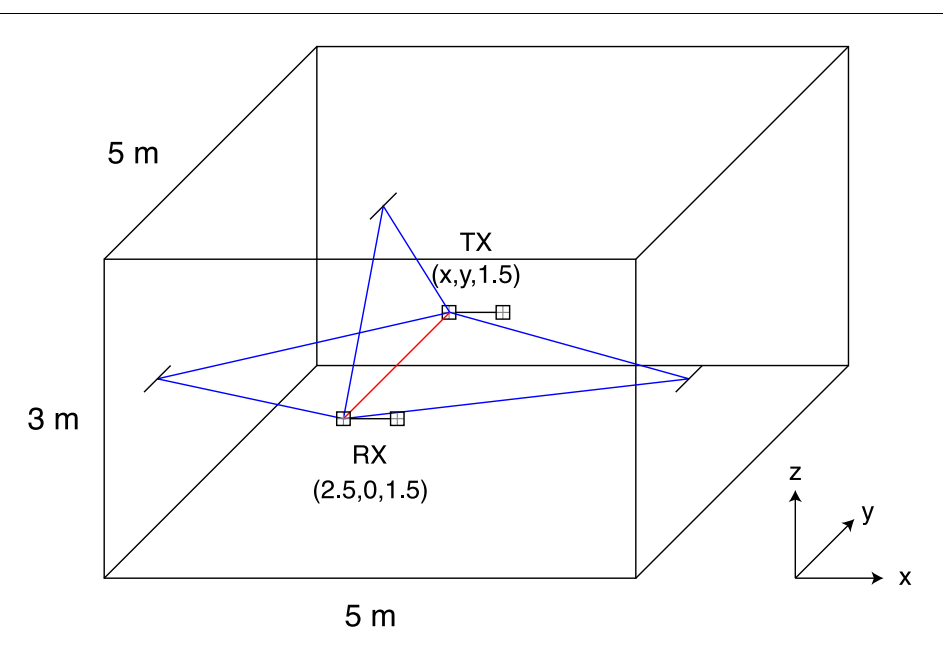


Figure 4.4: Indoor environment model.

Unless otherwise noted, the transmit array is also aligned parallel with the front and back walls.

Given the specular nature of mm-wave reflections, we model the environment using the method of geometrical optics [4]. The LOS paths from transmitter to receiver, as well as single-bounce reflected paths off the side walls and ceiling, contribute to the channel matrix  $\mathbf{H}$ . Higher order reflections are disregarded in the simulations due to the additional path losses and reflection losses they incur, as well as the directivity provided by the subarrays. The channel matrix  $\mathbf{H} \in \mathbb{C}^{N_T \times N_T}$  can be written

$$\mathbf{H} = \mathbf{H}_{LOS} + \mathbf{H}_{L} + \mathbf{H}_{R} + \mathbf{H}_{C} \tag{4.26}$$

where  $\mathbf{H}_{\mathrm{LOS}}$  is the LOS component,  $\mathbf{H}_{\mathrm{L}}$  and  $\mathbf{H}_{\mathrm{R}}$  are the components resulting from the left and right wall reflections, respectively, and  $\mathbf{H}_{\mathrm{C}}$  is the contribution of the ceiling reflections. The (m,n)th entry of  $\mathbf{H}_{\mathrm{LOS}}$  is given by

$$h_{\text{LOS}}(m,n) = \frac{\lambda}{4\pi p_{\text{LOS}}(m,n)} e^{-i\frac{2\pi}{\lambda}p_{\text{LOS}}(m,n)}.$$
 (4.27)

The (m, n)th entry of  $\mathbf{H}_{L}$  is given by

$$h_{\mathcal{L}}(m,n) = \Gamma_{\perp}(\theta_{\mathcal{L}}) \frac{\lambda}{4\pi p_{\mathcal{L}}(m,n)} e^{-i\frac{2\pi}{\lambda}p_{\mathcal{L}}(m,n)}$$
(4.28)

where  $p_{\rm L}(m,n)$  is the length of the path from the *n*th transmit antenna to the point of reflection on the left wall to the *m*th receive antenna, and  $\theta_{\rm L}$  is the reflected ray's angle of incidence.  $\Gamma_{\perp}(\theta_{\rm L})$  is the perpendicular Fresnel reflection coefficient [43]. The entries of  $\mathbf{H}_{\rm R}$  are similarly defined, with  $p_{\rm R}(m,n)$  and  $\theta_{\rm R}$  replacing  $p_{\rm L}(m,n)$  and  $\theta_{\rm L}$ . The (m,n)th entry of  $\mathbf{H}_{\rm C}$  is given by

$$h_{\mathcal{C}}(m,n) = \Gamma_{\parallel}(\theta_{\mathcal{C}}) \frac{\lambda}{4\pi p_{\mathcal{C}}(m,n)} e^{-i\frac{2\pi}{\lambda}p_{\mathcal{C}}(m,n)}$$
(4.29)

where  $\Gamma_{\parallel}(\theta_{\rm C})$  is the parallel reflection coefficient. We assume the floor is carpeted, and we hence ignore floor reflections due to the high reflection loss of carpeted surfaces [44].

There are two scenarios where modification of (4.26) is required. The first is in the case of LOS blockage, referred to herein as the non-LOS (NLOS) scenario, which we model by removing the  $\mathbf{H}_{LOS}$  term from (4.26). The second scenario

may occur when we alter the alignment of transmit array. Namely, if we rotate the array around the vertical axis that passes through its midpoint, a point of reflection on the left or wall may fall behind the array. Since we assume the energy radiated behind the array is highly attenuated by the transmitting device itself, this reflection component is omitted.

#### 4.4 Results

In this section, we evaluate the spectral efficiency achieved by the mm-wave MIMO architectures proposed in Section 4.2 using the indoor propagation model.

The system and environment parameters are as follows. The room dimensions are 5 m  $\times$  5 m  $\times$  3 m. The spacing between subarrays, given by  $d = \sqrt{\frac{2.5\lambda}{N}}$ , is chosen such that the LOS component of the channel is spatially uncorrelated when the transmit node is located at the center the room. The arrays are formed from  $4 \times 4 \lambda/2$ -spaced subarrays. The overall array length is thus  $L = (N-1)d + 1.5\lambda$ . The link operates at a carrier frequency of 60 GHz, with a corresponding wavelength of  $\lambda = 5$  mm. The noise power at the receiver is given by  $P_N = kTBF$ , where k is the Boltzmann constant, B = 2.16 GHz is the bandwidth, T = 300 K is the operating temperature, and F = 10 dB is the noise figure. The relative

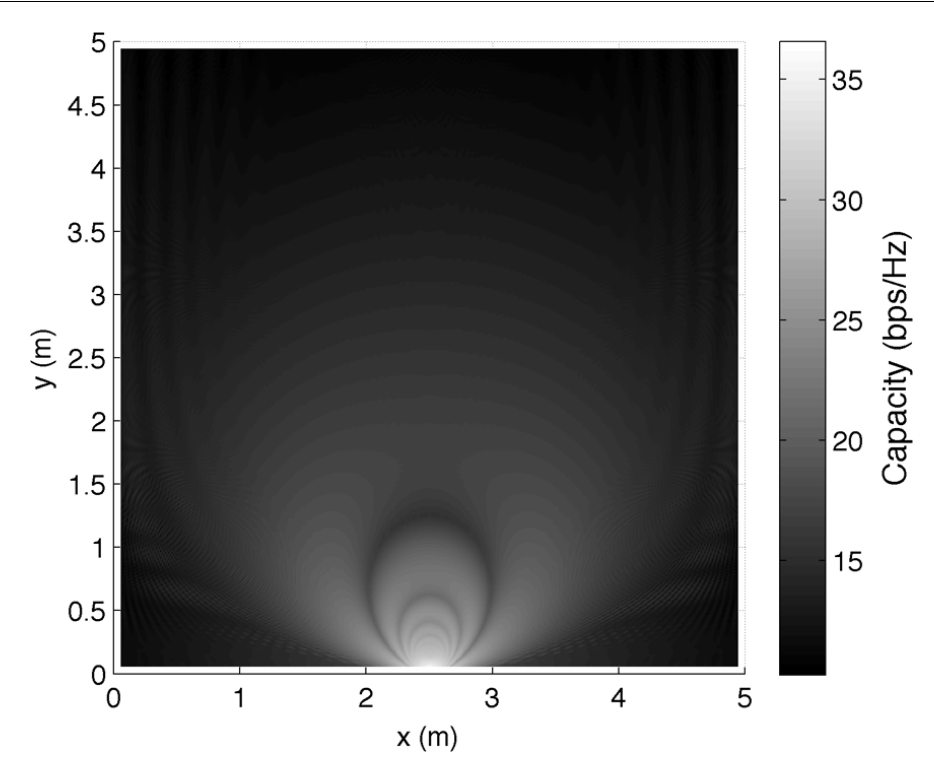


Figure 4.5: Channel capacity with waterfilling benchmark scheme as a function of transmitter coordinates.

dielectric constant  $\epsilon_r = 2.8$  and conductivity  $\sigma = 0.221$  of the wall and ceiling surfaces are chosen to represent plasterboard [44].

## 4.4.1 Performance of Waterfilling Benchmark

Fig. 4.5 depicts how the channel capacity varies as a function of the transmitter's position within the room. Here we have set N=2 and fixed the transmit power per antenna at  $P_A=-10$  dBm. The shade of gray at a particular value of (x,y) indicates the channel capacity when the transmitter is located at coordinates

(x,y). The plot can be interpreted as a top-down view of the room with the receiver located at (2.5,0). The capacity is primarily affected by two factors: path loss and spatial correlation. Path loss causes the received signal power, and hence the capacity, to decrease as the transmitter moves farther from the receiver. Spatial correlation fluctuates in a more complex manner based on the link geometry. Given the proposed architecture, the channel is represented by a  $32 \times 32$  matrix. We expect two of the thirty-two eigenmodes to be dominant when the spatial correlation between subarrays is low. This happens, for instance, when the transmitter is placed at the center of the room and the optimal ULA criterion is satisfied. The spatial correlation may increase at other transmitter positions, in which case the second eigenchannel becomes much weaker than the first. As the transmitter moves from the center of the room towards the receiver, for instance, a series of rings alternating between low and high correlation is observed. These particular fluctuations arise from the correlation in the LOS component of the channel matrix and are independent of the multipath environment.

Fig. 4.6 plots the capacity as a function of the transmitter's position assuming LOS blockage. As expected, the absence of the dominant LOS signal component results in lower SNR and capacity throughout the room. In contrast to the LOS scenario, however, the NLOS channel does not exhibit large fluctuations in capacity due to path loss. Instead, we observe small-scale fluctuations in capac-

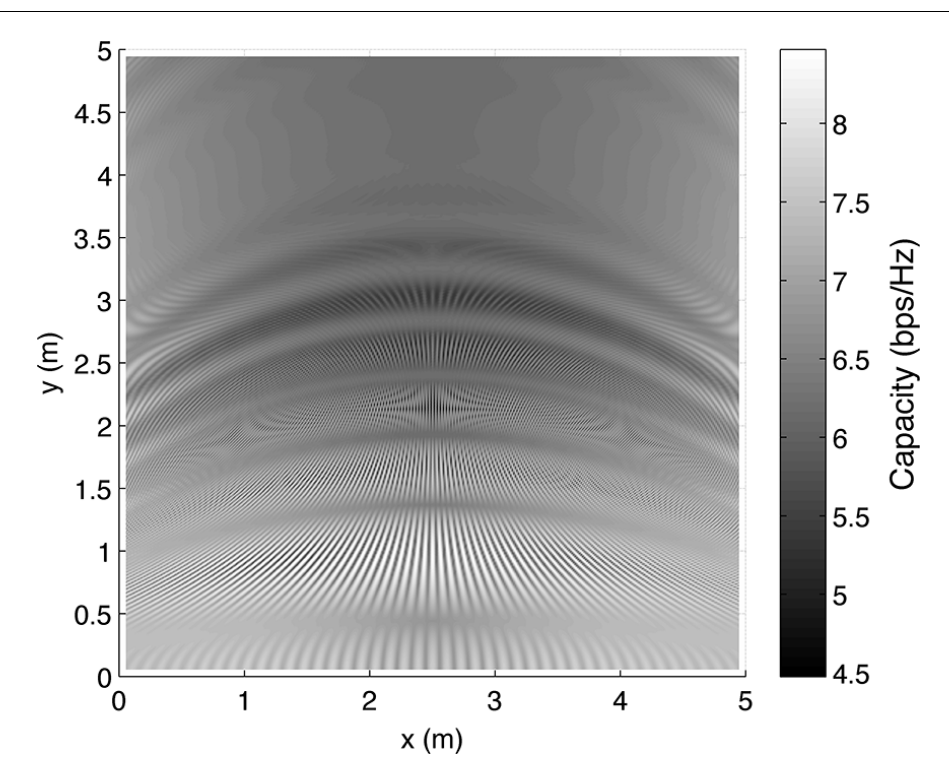


Figure 4.6: NLOS channel capacity with waterfilling benchmark scheme.

ity due to variations in spatial correlation. The fluctuations are on the order of several bits/s/Hz, which occur over distances on the order of millimeters. This suggests that, especially in NLOS settings, the link must be able to quickly adapt to changes in the transmitter or receiver locations if one or both nodes are mobile.

As described in Section 4.2.1, the left- and right-singular vectors corresponding to the N largest singular values specify the weights of the spatial filters at the receiver and transmitter, respectively. The filters beamsteer in the directions of the N strongest eigenmodes of the channel. In the LOS scenario considered above, both beams are generally directed along the LOS path, which offers the lowest

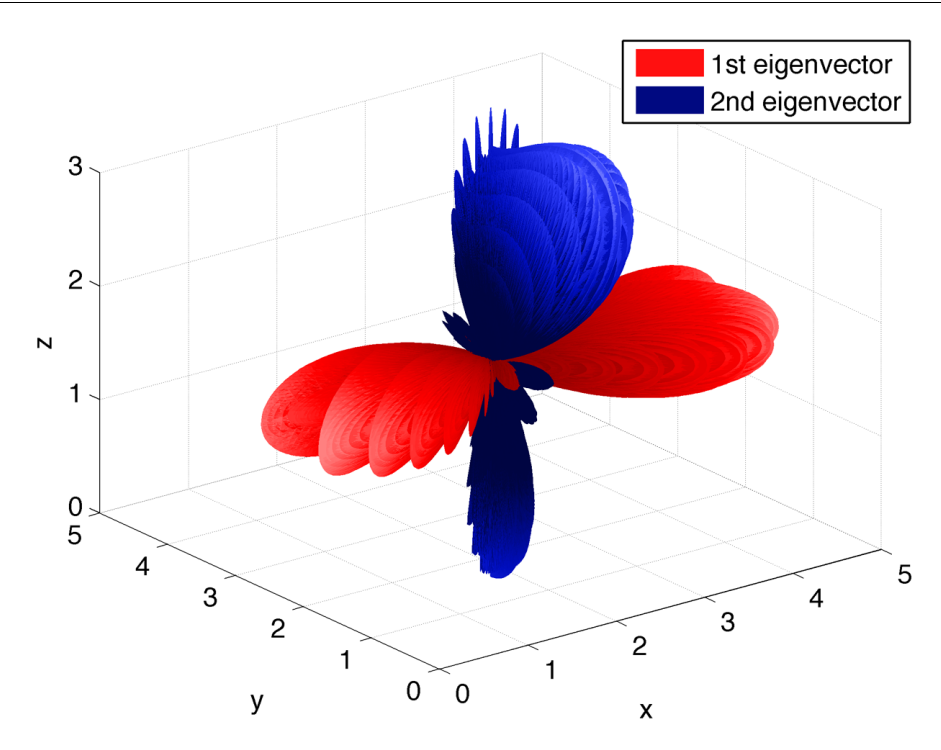


Figure 4.7: Transmit eigenvector field patterns in LOS blockage scenario.

path loss and reflection loss. When the LOS path is blocked, the link must utilize wall and/or ceiling reflections to close the link. In Fig. 4.7, the radiation patterns produced by the first and second right-singular (transmit) vectors are shown when the transmitter is located in the center of the room. The first eigenvector beamsteers in the directions of the wall reflections, while the second eigenvector utilizes the ceiling reflection. Grating lobes are caused by the subarrays being separated by several wavelengths.

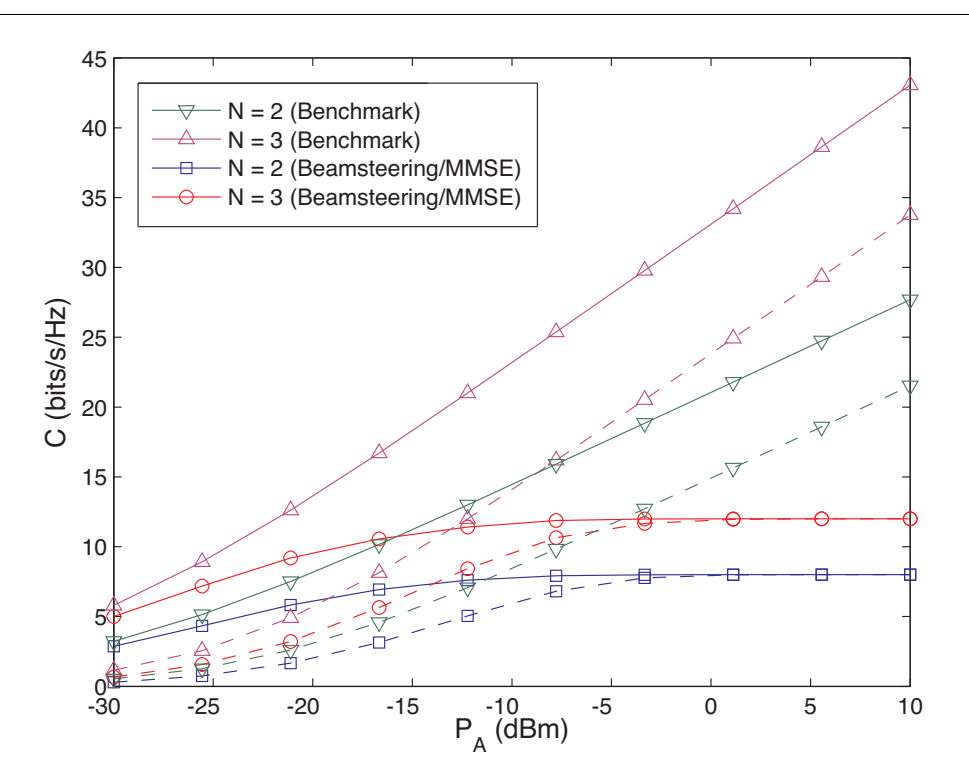


Figure 4.8: Channel capacity as a function average transmit power per antenna. Dashed lines represent the NLOS scenario.

# 4.4.2 Performance of Transmit Beamsteering/Receive MMSE

Fig. 4.8 plots the spectral efficiency, averaged over random transmitter coordinates, as a function of the per-antenna transmit power  $P_A$ . The transmitter's x and y coordinates are taken as independent random variables uniformly distributed over [0 + L/2, 5 - L/2]. The performances of both the waterfilling benchmark scheme and the beamsteering/MMSE scheme are included for comparison. In the former case,  $P_A$  represents the average transmit power per antenna. In prac-

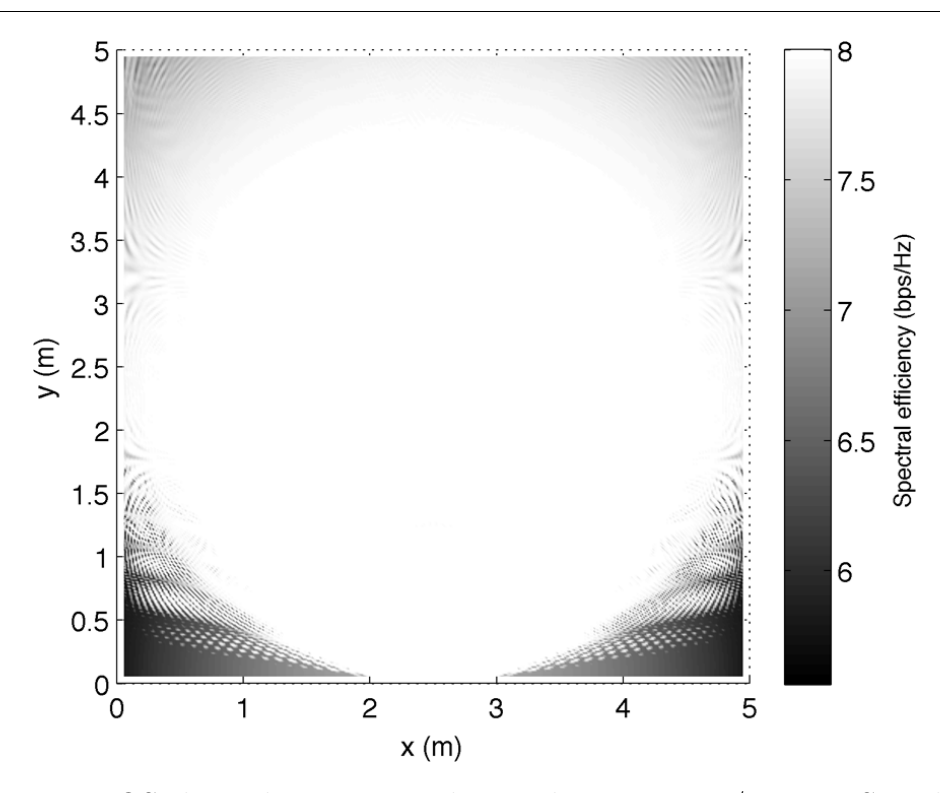


Figure 4.9: LOS channel capacity under TX beamsteering/RX MMSE scheme.

tice, each antenna element would be peak power limited, which is a constraint imposed on the more practical beamsteering/MMSE scheme. We observe that when the constellation is restricted to 16-QAM, the spectral efficiency reaches a 4N bps/HZ limit as  $P_A$  increases. This reduces the impact of LOS blockage on spectral efficiency under the beamsteering/MMSE scheme when the transmit power is sufficiently high.

The spectral efficiency is plotted as a function of transmitter position in Fig. 4.9 with N=2 and P=-10 dBm. The sum-rate capacity approaches the constellation-constrained limit of 8 bps/Hz when the transmitter is placed near

the center of the room. Uncoded data can be transmitted at a symbol error rate of  $P_e \leq 10^{-5}$  through 85.5% of the room, and at a symbol error rate of  $P_e \leq 10^{-10}$  through 73.5% of the room. When the channel is ill-conditioned, such as when the transmitter is placed in one of the front corners, an adaptive link can maintain a low error rate by increasing the transmit power, reducing the constellation size (e.g. QPSK or BPSK), or coding the data symbols. Through 86% of the room, the transmitter beamsteers both signals in the direction of the LOS path. If the LOS channel component is ill-conditioned, which occurs when the transmitter is placed in one of the front corners of the room, the spectral efficiency is increased by beamsteering one or both subarrays along a reflected path.

When the LOS path is blocked, the spectral efficiency throughout the room varies from 3.2 to 6.5 bps/Hz as shown in Fig. 4.10. Reliable uncoded transmission at the full 8 bps/Hz rate requires an additional 15 - 20 dBm of power. Alternatively, the transmitter can adapt the coding or modulation scheme to improve link reliability. Fig. 4.11 plots beamsteering directions that maximize the sum-rate capacity in the NLOS scenario. When the transmitter is located in the back half of the room, for example, the optimal strategy is to steer each subarray towards a different wall reflection. In the front half of the room, it is typically optimal to steer one beam towards the ceiling reflection, and the other towards the

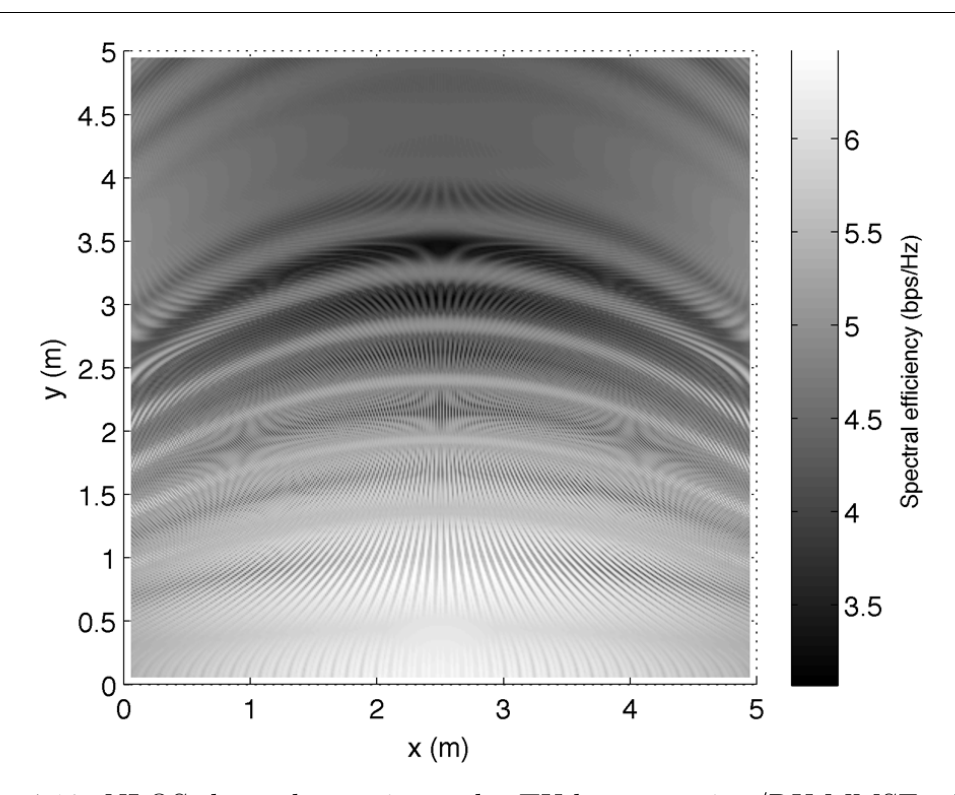


Figure 4.10: NLOS channel capacity under TX beamsteering/RX MMSE scheme. nearest wall reflection. The remaining schemes of steering both beams towards the ceiling or a single wall are optimal less frequently.

### 4.4.3 Transmitter Alignment

In the previous simulation results, the transmitter remained aligned facing the front wall. Fig. 4.12 compares this approach with an alternate alignment scheme as well as randomized alignment. We assume N=2, the transmitter coordinates (x,y) are chosen at random, and the waterfilling benchmark scheme is used. We observe from Fig. 4.12 that aligning the transmitter parallel with the front

wall offers the best performance in the NLOS scenario. This occurs because at any given location, the transmitter can beamsteer off either the left or side wall. The second alignment scheme we consider is pointing the transmitter at the receiver. This offers the best performance when the LOS path is unobstructed. When the LOS path is blocked, however, the nearest side wall may lie behind the array, and as a result, the transmitter must rely on the far wall to provide a reflected path. Finally, we consider the case where the transmit direction is a uniform random variable chosen in the range [-90°, 90°] with the two extreme values corresponding to the transmitter pointing toward the left and right walls, respectively. Comparing all schemes, we find that the spectral efficiency remains fairly robust to transmitter misalignment.

### 4.5 Discussion

We have established that spatial multiplexing gains can be layered on top of beamforming gains for indoor 60 GHz links, for nodes whose form factors conform to typical consumer electronics and computing devices. Relating the LOS MIMO channel to prolate spheroidal waveforms, whose eigenvalues drop off sharply around a value related to the array lengths, shows that an array of subarrays architecture is near-optimal: the subarray spacing can be adjusted to provide the maximum

number of degrees of freedom for a given form factor, while using multiple antenna elements within a subarray provides beamforming gain and reduces the transmit power per element.

Our simulations indicate that the architecture provides spatial multiplexing gains throughout an indoor environment, and that these gains are robust to node placement and LOS blockage as long as we can electronically steer the beam for each subarray. For a fixed constellation (which caps the maximum link speed), variations in spectral efficiency due to node placement are reduced. The impact of alignment between the transmitter and receiver arrays, and the geometry of the spatial eigenmodes as a function of node placement and LOS blockage, are discussed. Our promising results motivate future work on extensive performance evaluation for packetized communication with specific coded modulation schemes and signal processing algorithms, and on hardware implementation of the proposed architecture with careful partitioning of analog and digital signal processing.

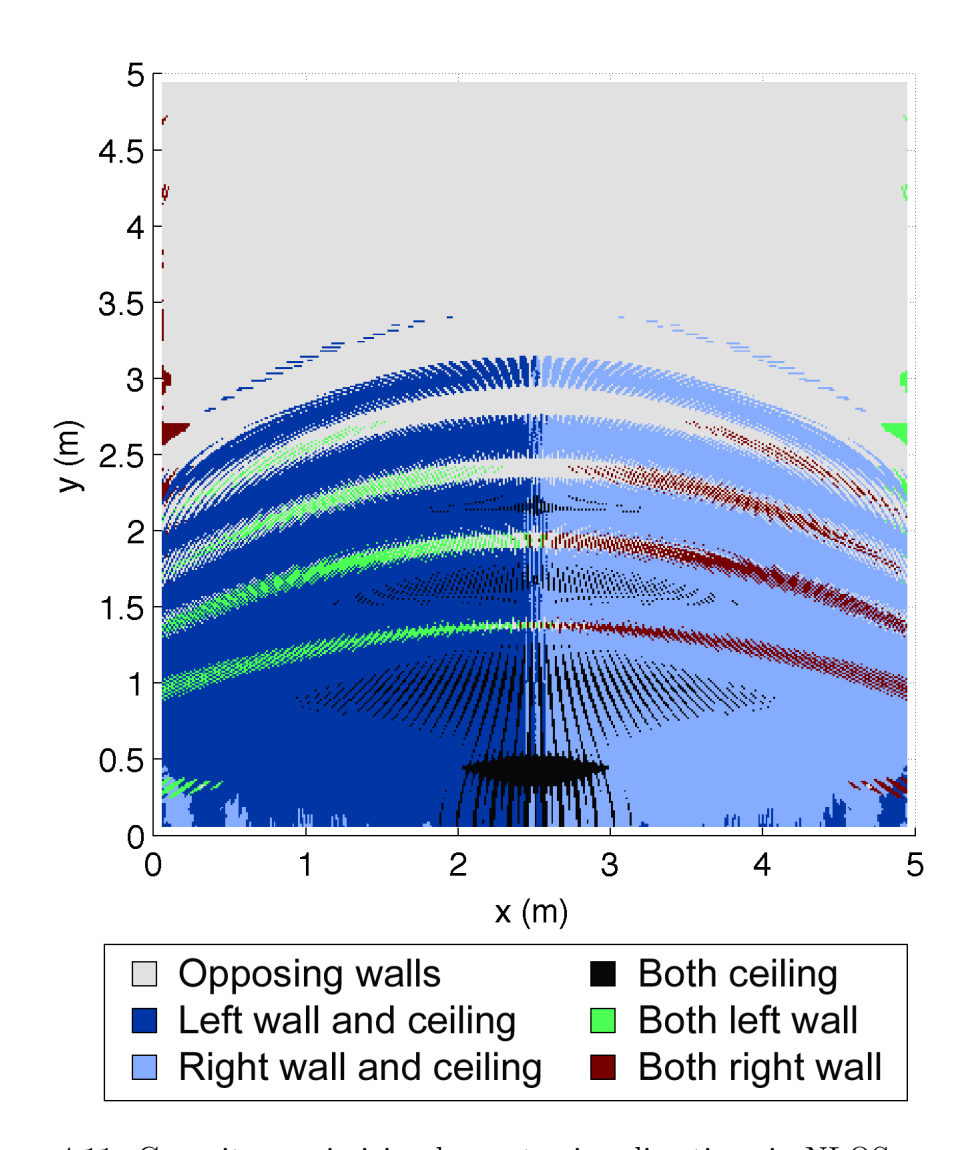


Figure 4.11: Capacity-maximizing beamsteering directions in NLOS scenario.

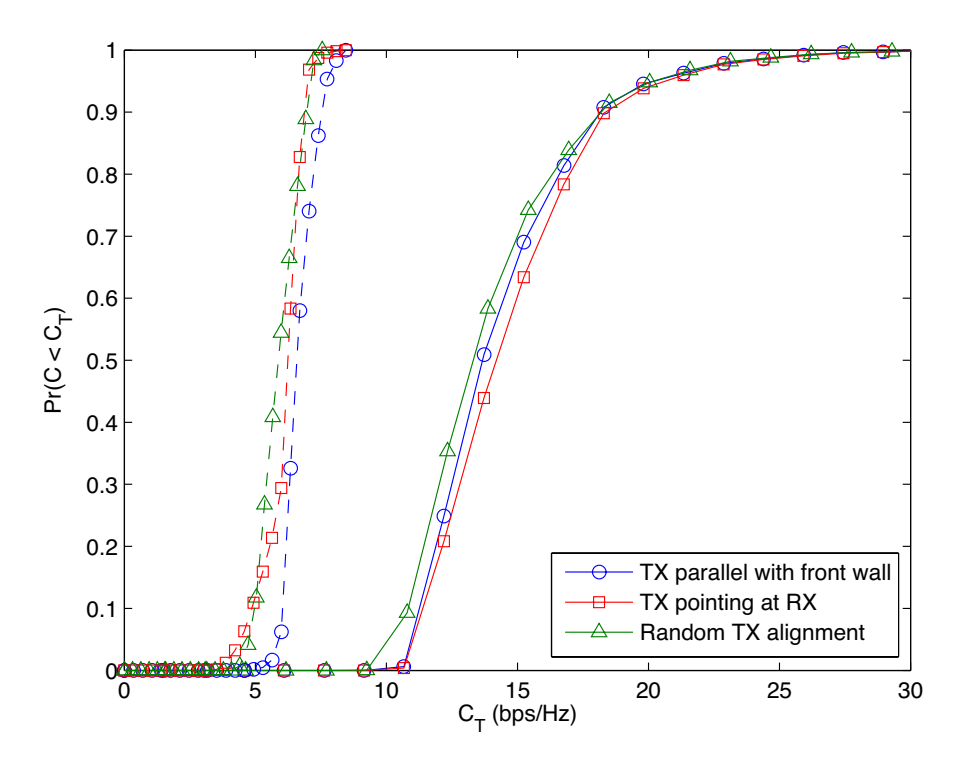


Figure 4.12: Cumulative distribution function of the spectral efficiency using various transmitter alignments. Dashed lines represent the NLOS scenario.

## Chapter 5

### Conclusions and Future Work

We considered the whether practical communication systems could achieve spatial multiplexing gains while operating at mm-wave frequencies. We began by identifying the key properties of the mm-wave band that result in new challenges and opportunities for MIMO systems. This motivated our examination of three main subjects, summarized as follows.

Based on the observation that the mm-wave channel is predominantly line-of-sight, we investigated the relation between antenna array geometry and spatial multiplexing. We found that, while Rayleigh-spaced uniform linear arrays maximize the channel capacity when the link range is known, they can perform poorly when the range deviates from nominal. When multiple transmitters fall within the grating lobes of the receiver's array response, the channel becomes rank deficient and the corresponding signals cannot be separated. In response, we proposed using non-uniform linear arrays, which were found to increase robustness under range

uncertainty. In addition, we proposed a practical rank adaptation scheme that reduces the number of transmitted streams when the channel is highly correlated.

Next we considered how, as bandwidths scale to multiple GHz, the cost of high-precision ADCs becomes prohibitive. In order to avoid this bottleneck, we propose decoupling the signal processing tasks of spatial equalization and signal demodulation. The spatial equalizer weights are determined from observations of low-frequency pilot tones embedded in the transmitted signals. Since the pilot tones fall within a narrow frequency band, they can be observed with a slow sampling rate. Equalization is carried out in the analog domain, using a network of variable gain amplifiers. The equalized signals can then be sampled at the full rate using 1-3 bit ADCs, which provide adequate precision for data demodulation. Several estimation/adaptation schemes for spatial equalization are evaluated and discussed. We reviewed experimental results from a four-channel hardware prototype demonstrating the viability the proposed architecture.

Finally, we evaluated the feasibility of mm-wave MIMO for indoor links, which are characterized by limited array form factors, multipath reflections, and potential LOS blockage. We identified fundamental limits on the spatial degrees of freedom available over a LOS channel when using arrays of fixed sized. We found that Rayleigh-spaced arrays are essentially optimal in terms of spatial degrees of freedom, and additional antennas provide only beamforming gain. This result

motivated our array of subarrays architecture, which utilizes subarrays of half-wavelength spaced elements for steering capability and array gain. We evaluated the performance of this architecture using ray-tracing modeling of an indoor environment. A sub-optimal transmission and reception scheme, chosen to represent today's mm-wave hardware and signal processing constraints, was evaluated relative to an optimal system. We found that indoor mm-wave MIMO links can attain spatial multiplexing gains even when the LOS is blocked.

### 5.1 Directions for Future Work

We proposed decoupling spatial equalization and demodulation as a means to avoid high-precision sampling at multiGbps rates. An alternative solution involves developing new signal processing algorithms that operate on highly quantized (1-3 bit) measurements. This has already shown to be a viable approach for many signal processing tasks [33], [34], [35], [36], [37]. Results in [38] suggest that this approach could be used for MIMO channel estimation, however the mean squared estimation error is fairly high for 1-bit quantization. However, research is active in this area, and it remains to be seen whether further improvements are possible.

As discussed in [30], the hardware prototype could be improved using custom ICs rather than off-the-shelf components, allowing higher bandwidths and a re-

duction in hardware cost. Dual polarization or larger 2-dimensional arrays could also be used to increase data rates. The heuristic adaptation algorithm implemented in the hardware prototype, while sufficient for proof-of-concept, lacks a firm foundation within the frameworks of estimation or adaptive filtering. Performance may improve using adaptive algorithms, such as differential MMSE, that provably converge to the linear MMSE solution.

In the context of indoor mm-wave MIMO links, many implementation issues remain open. For instance, spatial equalization in the proposed decoupled architecture occurs at a relatively slow time scale, making it most suitable for slowly-varying channels. Indoor environments may be subject to rapid variations due to the movement of people within the environment, possibly leading to LOS blockage. It remains unclear whether spatial multiplexing gains can be maintained in the face of rapid and severe channel fluctuations.

# Bibliography

- [1] I. E. Telatar, "Capacity of multi-antenna Gaussian channels," AT&T Bell Lab Internal Tech. Memo., Oct. 1995.
- [2] G. J. Foschini and M. Gans, "On the limits of wireless communications in a fading environment when using multiple antennas," *Wireless Personal Communications*, vol. 6, no. 3, p. 311, Mar. 1998.
- [3] H. Xu, V. Kukshya, and T. Rappaport, "Spatial and temporal characteristics of 60-GHz indoor channels," *IEEE J. Sel. Areas Commun.*, vol. 20, no. 3, pp. 620–630, Apr. 2002.
- [4] P. F. M. Smulders, "Deterministic modelling of indoor radio propagation at 40-60 Ghz," *Wireless Personal Communications*, vol. 4, no. 2, pp. 127–135, Jun. 1994.
- [5] R. Walden, "Performance trends for analog to digital converters," Communications Magazine, IEEE, vol. 37, no. 2, pp. 96–101, Feb. 1999.
- [6] S. Singh, R. Mudumbai, and U. Madhow, "Distributed coordination with deaf neighbors: Efficient medium access for 60 ghz mesh networks," in *INFOCOM*, 2010 Proceedings IEEE, Mar. 2010, pp. 1 –9.
- [7] IEEE Std 802.15.3c-2009 (Amendment to IEEE Std 802.15.3-2003), Oct. 2009.
- [8] High Rate 60 GHz PHY, MAC and HDMI PAL, 1st ed., ECMA-387, Dec. 2008.
- [9] Wireless Gigabit Alliance. [Online]. Available: http://wirelessgigabitalliance. org/
- [10] WirelessHD. [Online]. Available: http://www.wirelesshd.org/

- [11] D. Gesbert, H. Bolcskei, D. Gore, and A. Paulraj, "Outdoor MIMO wireless channels: models and performance prediction," *IEEE Trans. Commun.*, vol. 50, no. 12, pp. 1926–1934, Dec. 2002.
- [12] F. Bohagen, P. Orten, and G. Oien, "Design of optimal high-rank line-of-sight MIMO channels," *Wireless Communications, IEEE Transactions on*, vol. 6, no. 4, pp. 1420–1425, April 2007.
- [13] P. Larsson, "Lattice array receiver and sender for spatially orthonormal MIMO communication," *Vehicular Tech. Conf.*, *IEEE 61st*, vol. 1, pp. 192–196 Vol. 1, May 2005.
- [14] C. Sheldon, E. Torkildson, M. Seo, C. P. Yue, M. Rodwell, and U. Madhow, "Spatial multiplexing over a line-of-sight millimeter-wave MIMO link: A two-channel hardware demonstration at 1.2Gbps over 41m range," in 38th European Microwave Conference, Oct. 2008.
- [15] C. Sheldon, M. Seo, E. Torkildson, M. Rodwell, and U. Madhow, "A 2.4 Gb/s millmeter-wave link using adaptive spatial multiplexing," *IEEE Int. AP-S Symp.*, Jul. 2010.
- [16] C. H. Doan, S. Emami, A. M. Niknejad, and R. W. Brodersen, "Millimeter-wave cmos design," *IEEE Journal of Solid-State Circuits*, vol. 40, pp. 144–155, 2005.
- [17] B. Heydari, M. Bohsali, E. Adabi, and A. Niknejad, "Millimeter-wave devices and circuit blocks up to 104 ghz in 90 nm cmos," *Solid-State Circuits, IEEE Journal of*, vol. 42, no. 12, pp. 2893 –2903, Dec. 2007.
- [18] M. Khanpour, K. Tang, P. Garcia, and S. Voinigescu, "A wideband w-band receiver front-end in 65-nm cmos," *Solid-State Circuits, IEEE Journal of*, vol. 43, no. 8, pp. 1717 –1730, Aug. 2008.
- [19] B. Razavi, "A 60-ghz cmos receiver front-end," Solid-State Circuits, IEEE Journal of, vol. 41, no. 1, pp. 17 22, Jan. 2006.
- [20] X. Guan, H. Hashemi, and A. Hajimiri, "A fully integrated 24-ghz eight-element phased-array receiver in silicon," *Solid-State Circuits, IEEE Journal of*, vol. 39, no. 12, pp. 2311 2320, Dec. 2004.
- [21] A. Natarajan, A. Komijani, X. Guan, A. Babakhani, and A. Hajimiri, "A 77-ghz phased-array transceiver with on-chip antennas in silicon: Transmitter and local lo-path phase shifting," *Solid-State Circuits, IEEE Journal of*, vol. 41, no. 12, pp. 2807 –2819, Dec. 2006.

- [22] V. Dyadyuk, J. Bunton, J. Pathikulangara, R. Kendall, O. Sevimli, L. Stokes, and D. Abbott, "A multigigabit millimeter-wave communication system with improved spectral efficiency," *Microwave Theory and Techniques, IEEE Transactions on*, vol. 55, no. 12, pp. 2813–2821, Dec. 2007.
- [23] A. Poon, R. Brodersen, and D. Tse, "Degrees of freedom in multiple-antenna channels: a signal space approach," *Information Theory, IEEE Transactions on*, vol. 51, no. 2, pp. 523–536, Feb. 2005.
- [24] I. Sarris and A. Nix, "Design and performance assessment of maximum capacity MIMO architectures in line-of-sight," *Communications, IEE Proc.*, vol. 153, no. 4, pp. 482–488, Aug. 2006.
- [25] F. Bohagen, P. Orten, and G. Oien, "Optimal design of uniform rectangular antenna arrays for strong line-of-sight MIMO channels," *EURASIP J. Wirel. Commun. Netw.*, vol. 2007, no. 2, pp. 12–12, 2007.
- [26] R. Olsen, D. Rogers, and D. Hodge, "The  $aR^b$  relation in the calculation of rain attenuation," *IEEE Trans. Antennas Propag.*, vol. 26, no. 2, pp. 318–329, Mar. 1978.
- [27] Y. Karasawa and Y. Maekawa, "Ka-band Earth-space propagation research in Japan," *Proc. IEEE*, vol. 85, no. 6, pp. 821–842, Jun. 1997.
- [28] E. Torkildson, B. Ananthasubramaniam, U. Madhow, and M. Rodwell, "Millimeter-wave MIMO: Wireless links at optical speeds," in *Proc. of 44th Allerton Conference on Communication, Control and Computing*, Sep. 2006.
- [29] C. Sheldon, M. Seo, E. Torkildson, M. Rodwell, and U. Madhow, "Four-channel spatial multiplexing over a millimeter-wave line-of-sight link," *IEEE MTTS International Microwave Symposium*, Jun. 2009.
- [30] C. Sheldon, "Adaptive spatial multiplexing for millimeter-wave communication links," Ph.D. dissertation, University of California, Santa Barbara, 2009.
- [31] L. Tong, B. Sadler, and M. Dong, "Pilot-assisted wireless transmissions: general model, design criteria, and signal processing," *Signal Processing Magazine*, *IEEE*, vol. 21, no. 6, pp. 12 25, Nov. 2004.
- [32] M. Dong and L. Tong, "Optimal design and placement of pilot symbols for channel estimation," *Signal Processing, IEEE Transactions on*, vol. 50, no. 12, pp. 3055 3069, Dec. 2002.

- [33] J. Singh, O. Dabeer, and U. Madhow, "Communication limits with low precision analog-to-digital conversion at the receiver," in *Communications*, 2007. ICC '07. IEEE International Conference on, Jun. 2007, pp. 6269–6274.
- [34] D. Rousseau, G. V. Anand, and F. Chapeau-Blondeau, "Nonlinear estimation from quantized signals: Quantizer optimization and stochastic resonance," in *Proc. 3rd Int. Symp. Physics in Signal and Image Processing*, Jan. 2003, pp. 89–92.
- [35] T. Andersson, M. Skoglund, and P. Handel, "Frequency estimation by 1-bit quantization and table look-up processing," in *Proc. Europ. Signal Processing Conf.*, Sep. 2000, pp. 1807–1810.
- [36] O. Bar-Shalom and A. Weiss, "Doa estimation using one-bit quantized measurements," *Aerospace and Electronic Systems, IEEE Transactions on*, vol. 38, no. 3, pp. 868 884, Jul. 2002.
- [37] O. Dabeer and U. Madhow, "Channel estimation with low-precision analog-to-digital conversion," in *Communications (ICC)*, 2010 IEEE International Conference on, May 2010, pp. 1–6.
- [38] A. Mezghani, F. Antreich, and J. Nossek, "Multiple parameter estimation with quantized channel output," in *Smart Antennas (WSA)*, 2010 International ITG Workshop on, Feb. 2010, pp. 143–150.
- [39] D. Rife and R. Boorstyn, "Single tone parameter estimation from discrete-time observations," *Information Theory, IEEE Transactions on*, vol. 20, no. 5, pp. 591 598, Sep. 1974.
- [40] J. M. Mendel, Lessons in Estimation Theory for Signal Processing, Communications, and Control. Prentice Hall, 1995.
- [41] C. Sheldon, E. Torkildson, M. Seo, C. P. Yue, M. Rodwell, and U. Madhow, "A 60ghz line-of-sight 2×2 MIMO link operating at 1.2Gbps," in *IEEE Antennas and Propagation Society International Symposium Digest*, Jul. 2008.
- [42] A. Thaning, P. Martinsson, M. Karelin, and A. T. Friberg, "Limits of diffractive optics by communication modes," *Journal of Optics A: Pure and Applied Optics*, vol. 5, no. 3, p. 153, 2003.
- [43] T. S. Rappaport, Wireless Communications: Principles and Practice. New Jersey: Prentice Hall, 2002.

[44] K. Sato, H. Kozima, H. Masuzawa, T. Manabe, T. Ihara, Y. Kasashima, and K. Yamaki, "Measurements of reflection characteristics and refractive indices of interior construction materials in millimeter-wave bands," in *Vehicular Tech. Conf.*, *IEEE 45th*, vol. 1, Jul. 1995, pp. 449–453.